

**SYNTHESIS AND SPECTROSCOPIC,
ELECTROCHEMICAL, AND COMPUTATIONAL
STUDIES OF ORGANOMETALLIC COMPLEXES FOR
HYDROGEN PRODUCTION**



Orrasa In-noi

A Thesis Submitted in Partial Fulfillment of the Requirements for the

Degree of Doctor of Philosophy in Chemistry

Suranaree University of Technology

Academic Year 2012

การสังเคราะห์และการศึกษาทางสเปกโทรสโกปี ไฟฟ้าเคมีและการศึกษาเชิง
คำนวณของสารโลหะอินทรีย์เพื่อการผลิตไฮโดรเจน

นางสาวอรสา อินทร์น้อย



วิทยานิพนธ์นี้เป็นส่วนหนึ่งของการศึกษาตามหลักสูตรปริญญาวิทยาศาสตรดุษฎีบัณฑิต
สาขาวิชาเคมี

มหาวิทยาลัยเทคโนโลยีสุรนารี

ปีการศึกษา 2555

**SYNTHESIS AND SPECTROSCOPIC, ELECTROCHEMICAL,
AND COMPUTATIONAL STUDIES OF ORGANOMETALLIC
COMPLEXES FOR HYDROGEN PRODUCTION**

Suranaree University of Technology has approved this thesis submitted in partial fulfillment of the requirements for the Degree of Doctor of Philosophy.

Thesis Examining Committee

(Assoc. Prof. Dr. Jatuporn Wittayakun)

Chairperson

(Assoc. Prof. Dr. Kenneth J. Haller)

Member (Thesis Advisor)

(Prof. Dr. Dennis L. Lichtenberger)

Member

(Assoc. Prof. Dr. Albert Schulte)

Member

(Assoc. Prof. Dr. David J. Harding)

Member

(Prof. Dr. Sukit Limpijumnong)

Vice Rector for Academic Affairs

(Assoc. Prof. Dr. Prapun Manyum)

Dean of Institute of Science

อรรสา อินทร์น้อย : การสังเคราะห์และการศึกษาทางสเปกโทรสโกปี ไฟฟ้าเคมีและ
การศึกษาเชิงคำนวณของสารประกอบโลหะอินทรีย์เพื่อการผลิตไฮโดรเจน (SYNTHESIS
AND SPECTROSCOPIC, ELECTROCHEMICAL, AND COMPUTATIONAL
STUDIES OF ORGANOMETALLIC COMPLEXES FOR HYDROGEN
PRODUCTION)

อาจารย์ที่ปรึกษา : รองศาสตราจารย์ ดร.เค็นเนท เจ. แชลเลอร์, 145 หน้า.

ไฮโดรเจนคือพลังงานทางเลือกที่น่าสนใจสำหรับพลังงานสะอาดที่สามารถผลิตได้ใน
ธรรมชาติอย่างมีประสิทธิภาพโดยเอนไซม์ไฮโดรจิเนส สารประกอบที่ประกอบด้วยแกนหลัก
[2Fe2S] ที่มีโครงสร้างคล้ายกับบริเวณเร่งของเอนไซม์ไฮโดรจิเนสมีความสามารถในการเร่ง
ปฏิกิริยาไฟฟ้าเคมีการผลิตไฮโดรเจนจากโปรตอนและอิเล็กตรอน สารประกอบ [2Fe2S] ที่มีหมู่
แทนที่ไซโอเลดที่แตกต่างกัน *anti*-[(μ -methylthiolato)(μ -phenylthiolato)Fe₂(CO)₆] (1) และ *anti*-
[(μ -methylthiolato)(μ -2-thienylthiolato)Fe₂(CO)₆] (2) ถูกสังเคราะห์จากกรีนยาร์ดคลิเวจของ[(μ -
S₂)Fe₂(CO)₆] ตามด้วยปฏิกิริยาการเติมหมู่เมทิล สารประกอบที่มีหมู่เมทิลในตำแหน่งระนาบ และฟี
นิลหรือไซโอไนลในตำแหน่งตั้งฉากถูกแยกเป็นสารผลิตภัณฑ์หลัก ทำการวิเคราะห์ทางโครงสร้าง
สเปกโทรสโกปี ไฟฟ้าเคมีและการศึกษาเชิงคำนวณโดย DFT

สารประกอบ 1 และ 2 แสดงลักษณะสเปกตรัมการดูดกลืนรังสีอินฟราเรดในช่วงการยืด
ของหมู่คาร์บอนิลที่คล้ายกันแต่สเปกตรัมการดูดกลืนของสาร 1 มีการขยับเคลื่อนไปทางย่านความ
ยาวคลื่นแสงสีแฉงเล็กน้อยเทียบกับสเปกตรัมการดูดกลืนของสาร 2 เนื่องจากความหนาแน่นของ
อิเล็กตรอนที่อะตอมเหล็กทั้งสองของสาร 1 มีมากกว่า ซึ่งทำให้ 1 มีความยาวพันธะ Fe-Fe สั้นกว่า
และศักย์รีดักชันเริ่มต้นเป็นลบมากกว่า การศึกษาการเร่งปฏิกิริยาทางไฟฟ้าเคมีของปฏิกิริยารีดักชัน
โปรตอนของสาร 1 และ 2 โดยเทคนิคไซคลิกโวลแทมเมตรี การรีดักชันเริ่มต้นเกิดขึ้นที่ศักย์
ประมาณ -1.4 V ถึง -1.5 V vs. Fe⁺/Fe ทำให้เกิดสารที่มีสมบัติในการเร่งปฏิกิริยาการรีดักชันของ
โปรตอนจากสารละลายกรดอะซิติก โดยเกิดขึ้นที่ศักย์ประมาณ -1.8 V ซึ่งถือว่าเกิดขึ้นที่
ศักย์ไฟฟ้าต่ำเมื่อเทียบกับศักย์รีดักชันของโปรตอนเมื่อเร่งโดยสารประกอบ [μ -(1,2-
benzenedithiolato)Fe₂(CO)₆] และ [μ -(1,3-propanedithiolato)Fe₂(CO)₆] พิธีของการเร่งปฏิกิริยานี้
หายไปถ้าสารละลายอิมิตัวด้วยคาร์บอนมอนอกไซด์ซึ่งอาจอธิบายได้ว่าคาร์บอนมอนอกไซด์อาจจะ
บดบังบริเวณที่โปรตอนเข้าไปจับกับบริเวณเร่ง หรือ ไปยับยั้งการเกิดสารที่มีสมบัติเป็นตัวเร่ง
ปฏิกิริยา การเติมกรดลงในสารละลายทำให้ศักย์รีดักชันเริ่มต้นเคลื่อนไปทางบวก อาจเนื่องจากผล
ของพันธะไฮโดรเจนหรือโปรตอนไปจับกับโมเลกุลตัวเร่งที่มีผลให้ความหนาแน่นของอิเล็กตรอน
ที่อะตอมเหล็กลดลง นอกจากนี้ลักษณะการเร่งปฏิกิริยาของ 2 ยังถูกจำกัดและศักย์มีการขยับไปทาง
ลบมากขึ้นเมื่อความเข้มข้นของกรดที่ 50 mM ซึ่งอาจเกิดกระบวนการเร่งด้วยกระบวนการอื่น

ในสารละลายอิมิตัวด้วยในโทรเจนที่มีและไม่มีกรดอะซิติก ศักย์ไฟฟ้าของการเร่งปฏิกิริยาที่ -2.2 V แสดงการเคลื่อนไปทางบวกอย่างต่อเนื่องเมื่อมีการสแกนซ้ำที่ไม่มีการขัดขวางไฟฟ้าระหว่างสแกน ข้ออธิบายหนึ่งที่เป็นไปได้ของการเกิดการเคลื่อนไปทางบวกนี้คือการเคลื่อนไปข้างหน้าของอิเล็กตรอนโดยโมเลกุลที่เกิดขึ้นจากการรีดิวซ์

ได้ทำการคำนวณโดยทฤษฎี DFT ของโมเดลแบบรีดักทีฟบางอัน ได้แก่แบบที่มีการหมุนและไม่มีการหมุนของไดแอนไอออนที่มีการแตกตัวเป็นแอนไอออนเดี่ยวเพื่อเสนอกลไกของการเกิดรีดักชัน ค่าศักย์รีดักชันเริ่มต้นที่คำนวณได้ใกล้เคียงกับค่าที่ได้จากการทดลอง อย่างไรก็ตามค่าศักย์ออกซิเดชันที่คำนวณได้ของโมเดลแบบรีดักทีฟแตกต่างอย่างมากจากค่าที่ได้จากการทดลอง



สาขาวิชาเคมี

ปีการศึกษา 2555

ลายมือชื่อนักศึกษา _____

ลายมือชื่ออาจารย์ที่ปรึกษา _____

ORRASA IN-NOI : SYNTHESIS AND SPECTROSCOPIC,
ELECTROCHEMICAL, AND COMPUTATIONAL STUDIES OF
ORGANOMETALLIC COMPLEXES FOR HYDROGEN PRODUCTION
THESIS ADVISOR : ASSOC. PROF. KENNETH J. HALLER, Ph.D. 145 PP.

[FeFe]-HYDROGENASE/PROTON REDUCTION/ELECTROCHEMISTRY/
HYDROGEN PRODUCTION/IRON-SULFUR COMPLEX/DFT

Hydrogen is an attractive alternative fuel for clean energy that is efficiently produced in nature by hydrogenase enzymes. Complexes containing the [2Fe2S] core, inspired by the [FeFe]-hydrogenase active site, have potential for electrocatalytic hydrogen production from protons and electrons. The [2Fe2S] complexes with unsymmetrically substituted thiolate ligands, *anti*-[(μ -methylthiolato)(μ -phenylthiolato)Fe₂(CO)₆] (**1**) and *anti*-[(μ -methylthiolato)(μ -2-thienylthiolato)Fe₂(CO)₆] (**2**) were synthesized by Grignard cleavage of [(μ -S₂)Fe₂(CO)₆] followed by methylation. The complexes with methyl groups in equatorial positions and phenyl or thienyl groups in axial positions were isolated as the major products. Structural analysis, spectroscopy, electrochemistry, and density functional theory (DFT) calculations were performed.

Complexes **1** and **2** show similar infrared absorption spectra in carbonyl stretching region with **1** slightly red shifted compared to **2**, presumably because of more electron richness on its diiron center of **1** which is also provides a shorter Fe–Fe bond and slightly more negative in initial reduction potential for **1**. Electrocatalyzed proton reductions of **1** and **2** were examined by cyclic voltammetry. The initial reduction occurs at –1.4 to –1.5 V vs. Fc⁺/Fc and generates the reactive catalysts which then catalyze proton reduction from acetic acid solutions at about –1.8 V; at a relatively low potential compared to

$[\mu\text{-(1,2-benzenedithiolato)Fe}_2(\text{CO})_6]$ and $[\mu\text{-(1,3-propanedithiolato)Fe}_2(\text{CO})_6]$ as catalysts. The catalytic peaks completely disappear in saturated CO solutions, suggesting that CO may block the protonation site on the reactive species or inhibit generation of the catalytically active species. Adding acid to the solution shifts the initial reduction in a positive direction suggesting a hydrogen bond effect or protonation of catalyst molecules which can reduce electron density on the iron center. In addition, the catalytic behavior of **2** is limited when adding more acetic acid up to 50 mM suggesting other processes may proceed. Under N₂ saturated solution with and without acetic acid, catalytic potential at around -2.2 V clearly shows a progressively positive shift with repeat scan without polished electrode between each scan. One possible explanation of this positive shift is electrode coating by reduced species.

DFT calculations of some reductive models including rotated form of dianions and unrotated form of dianions with dissociation to monomer anions, have been attempted to proposed reduction mechanism. The calculated initial reduction potential close to the experimental value is obtained. However, the calculated oxidation potential of these reductive models is quite far from the experimental value.

School of Chemistry

Academic Year 2012

Student's Signature _____

Advisor's Signature _____

ACKNOWLEDGEMENTS

It is impossible to thank all people who have helped me on my study but, I will give it a try.

I would like to express my sincerest gratitude to my supervisor, Assoc. Prof. Dr. Kenneth J. Haller, for his guidance, enthusiasm, and patience throughout the years of my studies. Indeed, I become a stronger person because of his philosophy and psychology.

I would like to express my sincere thanks to Prof. Dr. Dennis L. Lichtenberger, The University of Arizona, for his challenging ideas and works, serving as a committee member in my Ph.D. defense and providing paperwork for my second visit to his laboratories. I am very appreciated for all of his help.

I wish to express my special thanks to Assoc. Prof. Dr. Jatuporn Wittayakhun for serving as a chairperson for my Ph.D. defense committee, Assoc. Prof. Dr. David J. Harding, Walailak University, and Assoc. Prof. Dr. Albert Schulte for serving as committee members in my Ph.D. defense. I am grateful for their comments and suggestions.

I would like to thank Prof. Dr. John H. Enemark, The University of Arizona, for his help in paperwork to apply for my first visit, chemicals, equipment, his support, and his inspiring advice.

Overwhelming thanks go to all of the Collaborative Research in Chemistry (CRC) group members, The University of Arizona, Prof. Dr. Richard S. Glass, Prof. Dr. Dennis H. Evans, The University of Purdue, and Team DLL, Gabe, Laura, Susan, Elliot, Steve, Matt, and Takahei, for their help and suggestions with the laboratory work and friendship,

good sound advice and good teaching. I have learned a lot from them and they made my time with them very memorable.

Dr. Eric Klein and all JHE group members for helping me in the laboratory and good advice. Dr. Gary S. Nichol and Dr. Sue A. Roberts, for their kind help on X-ray crystallography and Dr. Neil Jacobson, for his advice and help with the NMR spectroscopy. Special thanks to Dr. Takahiro Sakamoto for his kindness, goodwill, and strong advice during my study time at The University of Arizona, and to the technical and support staffs at Suranaree University of Technology and Department of Chemistry and Biochemistry, The University of Arizona, for their assistance in the paper work, acquisition of chemicals and equipment, and generous help.

I would like to thank the Office of the Commission of Higher Education, Thailand for financial support for my Ph.D. study. Thanks are also due to former and current members of the Applied Surface Science and Crystallography Group, Suranaree University of Technology, for their friendship, generous help, encouragement, and entertainment to minimize my stress, and for companionship during my study time. We had a lot of good times together.

Special thanks to Khongvit Prasitnok for his support and inspiration. He has provided constant encouragement, especially at difficult moments. Thank you for always being by my side.

Last, but very meaningful, I am deeply indebted to my parents for their support, unconditional love and encouragement throughout the long period of my study. Without their love and understanding this work would not be possible.

Orrasa In-noi

CONTENTS

	Page
ABSTRACT IN THAI	I
ABSTRACT IN ENGLISH	III
ACKNOWLEDGEMENTS	V
CONTENTS	VII
LIST OF TABLES	X
LIST OF FIGURES	XII
LIST OF SCHEMES	XVIII
LIST OF SYMBOLS AND ABBREVIATIONS	XIX
CHAPTER	
I INTRODUCTION AND LITERATURE REVIEW.....	1
1.1 Hydrogen as Future Fuel.....	1
1.2 [2Fe2S] Complexes from Nature: Hydrogenase Enzymes	3
1.3 [2Fe2S] Complexes for Hydrogen Production	6
1.4 Research Objectives.....	20
II GENERAL BACKGROUND	21
2.1 The Manipulation of Air-Sensitive Compounds.....	22
2.2 NMR Spectroscopy.....	27
2.3 IR Spectroscopy	28
2.4 Gas-Phase Ultraviolet Photoelectron Spectroscopy	30
2.5 Cyclic Voltammetry.....	33

CONTENTS (Continued)

	Page
2.6 X-ray Crystallography	37
2.7 Density Functional Theory	39
III EXPERIMENTAL	41
3.1 Preparation of Materials	41
3.2 Characterizations	44
3.3 Density Functional Theory Calculations	46
IV SPECTROSCOPIC, STRUCTURAL, AND COMPUTATIONAL	
STUDIES OF $[(\mu\text{-SR})(\mu\text{-SR}')\text{Fe}_2(\text{CO})_6]$	48
4.1 NMR Spectroscopy	48
4.2 X-ray Structural Determination	52
4.3 Infrared Spectroscopy	61
4.4 Gas-Phase UV Photoelectron Spectroscopy	63
V ELECTROCHEMICAL AND COMPUTATIONAL STUDIES OF	
$[(\mu\text{-SR})(\mu\text{-SR}')\text{Fe}_2(\text{CO})_6]$	70
5.1 Electrochemical Investigation	70
5.2 Electrocatalyzed Proton Reduction of Weak Acid	75
5.3 IR Spectra of Reduced Species	86
5.4 Density Functional Theory Study	87
VI CONCLUSIONS AND FUTURE DIRECTIONS	93
6.1 Conclusions	93
6.2 Future Directions	95

CONTENTS (Continued)

	Page
REFERENCES	96
APPENDICES	113
APPENDIX A SUPPORTING INFORMATION CHAPTER III.....	114
APPENDIX B SUPPORTING INFORMATION CHAPTER IV	116
APPENDIX C SUPPORTING INFORMATION CHAPTER V	135
APPENDIX D CONFERENCES AND PRESENTATIONS.....	142
CURRICULUM VITAE.....	145



LIST OF TABLES

Table	Page
1.1 Comparison of hydrogen properties with other common fuels.	2
2.1 Common cooling bath mixtures.....	27
2.2 Acid dissociation constants (pK_a) and standard potentials for the HA/A ⁻ , H ₂ half reaction of some acids in acetonitrile.....	36
4.1 Summary of data collection and structure refinement parameters for complexes [(μ -SMe)(μ -SPh)Fe ₂ (CO) ₆] and [(μ -SMe)(μ -STh)Fe ₂ (CO) ₆]	53
5.1 Electrochemical data of 1 , 2 and related diiron complexes in CH ₃ CN.....	78
5.2 Peak shift on initial reduction and catalytic peak currents as function of acid strength.....	80
5.3 Proposed reduction mechanism with calculated reduction potential (V) and Gibbs energy of calculated reaction (kcal/mol)	90
5.4 Calculated pK_a and binding energy (kcal/mol) of MeCN or CO to proposed reduced species.....	91
B.1 Comparison of selected bond lengths and angles of crystallographically independent A and B of [(μ -SMe)(μ -SPh) Fe ₂ (CO) ₆] to DFT structures	120
B.2 Comparison of selected bond lengths and angles of crystallographically independent C and D of [(μ -SMe)(μ -SPh) Fe ₂ (CO) ₆] to DFT structures	121
B.3 Comparison of selected bond lengths and angles of [(μ -SMe)(μ -STh) Fe ₂ (CO) ₆] to DFT structures	122
B.4 Bond lengths (Å) and angles (°) for [(μ -SMe)(μ -SPh)Fe ₂ (CO) ₆].....	123
B.5 Bond lengths (Å) and angles (°) for [(μ -SMe)(μ -STh)Fe ₂ (CO) ₆]	125

LIST OF TABLES (Continued)

Table	Page
B.6 Optimized geometry (cartesian coordinates in Å)	126



LIST OF FIGURES

Figure	Page
1.1 Cartoon drawing of ideal hydrogen production	3
1.2 Structures of the hydrogenase active sites.....	4
1.3 Ribbon representation of <i>Clostridium pasteurianum</i> (CpI) hydrogenase with the [FeFe] active site and [4Fe4S] clusters chain shown as capped stick models.....	6
1.4 Structural diagram of $[\text{Fe}_4\text{S}_4(\text{SCH}_3)_3\{\text{Fe}_2(\text{CH}_3\text{C}(\text{CH}_2\text{S})_3)(\text{CO})_5\}]^{2-}$	7
1.5 Model of general hydrogenase inspired catalysts.....	9
1.6 Structural diagram of $\{[\text{Na}_2(\text{THF})(\text{OEt}_2)_3][\text{BDT}^{2-}]\}_2$	12
1.7 <i>ORTEP</i> diagram of the dimerized structure of PDT dianion with 50% thermal ellipsoids	13
1.8 Structural diagram of $[\text{Fe}_4(\mu\text{-S}(\text{CH}_2)_2\text{S})_2(\mu\text{-CO})_2(\text{CO})_8]^{2-}$ with 50% thermal ellipsoids	14
1.9 Possible isomers of $[(\mu\text{-SR})(\mu\text{-SR}')\text{Fe}_2(\text{CO})_6]$	18
2.1 Double manifold for Schlenk line	22
2.2 Solution transfer using a stainless-steel cannula	25
2.3 Three types of metal–CO interactions.....	28
2.4 Molecular orbital diagram of carbonyl.....	29
2.5 IR spectrum in carbonyl stretching region of $\text{Fe}_2\text{cdt}(\text{CO})_6$, $[\text{Fe}_2(\mu\text{-bdt})(\text{CO})_6]$ and $[\text{Fe}_2(\mu\text{-pdt})(\text{CO})_6]$ in CH_3CN	30
2.6 Schematic illustration of the photoelectric effect.....	31

LIST OF FIGURES (Continued)

Figure	Page
2.7 Components of a gas phase UPS instrument.....	32
2.8 Cyclic voltammogram of ferrocene in acetonitrile representing a reversible process	34
2.9 Linear sweep voltammograms of 10 mM acetic acid in acetonitrile at various electrodes as indicated	37
2.10 Reflection of X-ray beams relative to planes of atoms in a solid.....	38
4.1 Structural diagrams of isolated products of $[(\mu\text{-SMe})(\mu\text{-SPh})\text{Fe}_2(\text{CO})_6]$ and $[(\mu\text{-SMe})(\mu\text{-STh})\text{Fe}_2(\text{CO})_6]$	51
4.2 Variable temperature $^1\text{H-NMR}$ of mixed isomers of $[(\mu\text{-SMe})(\mu\text{-SPh})\text{Fe}_2(\text{CO})_6]$ in dioxane- d_8 solution.....	52
4.3 Crystal morphology of $[(\mu\text{-SMe})(\mu\text{-SPh})\text{Fe}_2(\text{CO})_6]$ and $[(\mu\text{-SMe})(\mu\text{-STh})\text{Fe}_2(\text{CO})_6]$	54
4.4 <i>ORTEP</i> diagram of the asymmetric unit of $[(\mu\text{-SMe})(\mu\text{-SPh})\text{Fe}_2(\text{CO})_6]$ with Fe and S atoms label.....	55
4.5 <i>ORTEP</i> diagrams of four crystallographically independent molecules, A, B, C and D , of $[(\mu\text{-SMe})(\mu\text{-SPh})\text{Fe}_2(\text{CO})_6]$	56
4.6 Least-squares overlays of each pair of isomeric molecules	57
4.7 Overlay crystallographically independent molecule A, B, C , and D of $[(\mu\text{-SMe})(\mu\text{-SPh})\text{Fe}_2(\text{CO})_6]$ with DFT structures.....	58

LIST OF FIGURES (Continued)

Figure	Page
4.8	<i>ORTEP</i> diagram of molecular structure of 2 and its overlay with DFT structure..... 60
4.9	IR spectra in CO stretching region of 1 and 2 62
4.10	Comparison of the experimental IR spectra in the CO stretching region with DFT calculated IR spectra 63
4.11	He I and He II photoelectron spectra of 1 and 2 64
4.12	Plots of LUMO and HOMOs of 1 66
4.13	Plots of LUMO and HOMOs of 2 68
5.1	Structural diagrams of $[(\mu\text{-SMe})(\mu\text{-SPh})\text{Fe}_2(\text{CO})_6]$ (1) and $[(\mu\text{-SMe})(\mu\text{-STh})\text{Fe}_2(\text{CO})_6]$ (2) 70
5.2	Reduction and oxidation scans of 1 and 2 in CH_3CN under N_2 atmosphere..... 71
5.3	Cyclic voltammograms of 1 and 2 72
5.4	Cathodic current recoveries in return scan at varied scan rates of 2 73
5.5	Cathodic current recoveries of 2 at different equilibration times..... 74
5.6	Cyclic voltammograms of 2 at various scan rates 75
5.7	Cyclic voltammograms of 1 and 2 with varied concentrations of HOAc under N_2 77
5.8	Cyclic voltammograms of 2 in the presence of different acids as indicated..... 79
5.9	Cyclic voltammograms of 2 under CO atmosphere without added acid..... 82
5.10	Atmospheric dependence of reduction scans of 2 82

LIST OF FIGURES (Continued)

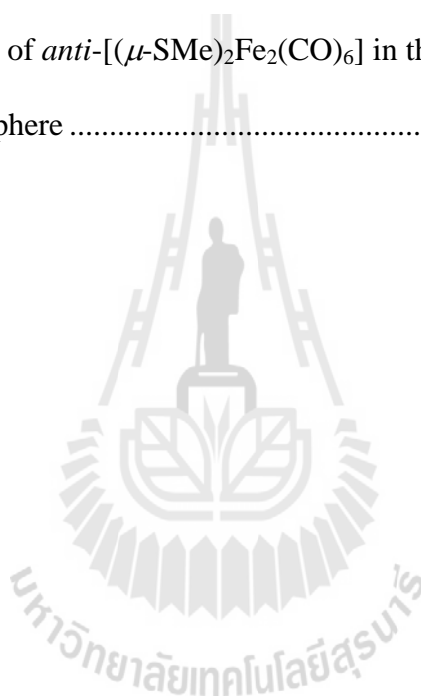
Figure	Page
5.11 Voltammograms of 1 and 2 with varied concentrations of HOAc under CO atmosphere.....	83
5.12 Reduction potential as function of repeating scan of 1 in the absence of acid under N ₂ and CO atmospheres	85
5.13 Catalytic potential as function of repeating scan of 1 in the presence of 50 mM acetic acid under N ₂ and CO atmospheres	85
5.14 IR spectra in the CO stretching region of electrolyte solution recorded prior and after 10 min bulk electrolysis of 1	86
5.15 Voltammogram of 2 in the absence of HOAc under N ₂ atmosphere	88
A.1 IR spectrum in carbonyl stretching region of [(μ -S) ₂ Fe ₂ (CO) ₆] in hexane	114
B.1 ¹ H-NMR spectrum of 1 in CDCl ₃ solution.....	116
B.2 ¹ H-NMR spectrum of [(μ -SMe)(μ -SPh)Fe ₂ (CO) ₆] in CDCl ₃ solution prepared from the mixed <i>anti</i> -isomer crystals.....	116
B.3 ¹³ C-NMR spectrum of [(μ -SMe)(μ -SPh)Fe ₂ (CO) ₆] in CDCl ₃ solution prepared from the mixed <i>anti</i> -isomer crystals.....	117
B.4 ¹ H-NMR spectrum of 2 in CDCl ₃ solution.....	117
B.5 ¹³ C-NMR spectrum of 2 in CDCl ₃ solution.....	118
B.6 Comparison of the experimental XRD pattern of bulk sample of 1 with the simulated XRD pattern from the mixed <i>anti</i> -isomer crystal data.....	118

LIST OF FIGURES (Continued)

Figure	Page
B.7 Comparison of the experimental and simulated XRD pattern of 2	119
B.8 Comparison of DFT structures of different isomers of [(μ -SMe)(μ -SPh)Fe ₂ (CO) ₆] and [(μ -SMe)(μ -STh)Fe ₂ (CO) ₆].....	134
C.1 Voltammograms of 1 in the absence/presence of acetic acid under N ₂ atmosphere.....	135
C.2 Voltammograms of 2 in the absence/presence of acetic acid under N ₂ atmosphere.....	135
C.3 Voltammograms of <i>anti</i> -[(μ -SMe) ₂ Fe ₂ (CO) ₆] in the absence/presence of acetic acid under N ₂ atmosphere	136
C.4 Voltammograms 2 in the absence/presence of phenol (p <i>K</i> _a , 29.14) under N ₂ atmosphere.....	136
C.5 Voltammograms 2 in the absence/presence of 4-bromophenol (p <i>K</i> _a , 25.53) under N ₂ atmosphere.....	137
C.6 Voltammograms of 2 in the absence/presence of cyanoacetic acid (p <i>K</i> _a , 18) under N ₂ atmosphere	137
C.7 Direct reduction at GC electrode surface of HOAc under N ₂ atmosphere	138
C.8 Direct reduction at GC electrode surface of HOAc under CO atmosphere	138

LIST OF FIGURES (Continued)

Figure	Page
C.9 ^1H -NMR spectrum of <i>anti</i> - $[(\mu\text{-SMe})_2\text{Fe}_2(\text{CO})_6]$ in CDCl_3 solution.....	140
C.10 IR absorption spectrum in CO stretching region of <i>anti</i> - $[(\mu\text{-SMe})_2\text{Fe}_2(\text{CO})_6]$ in hexane	140
C.11 Voltammograms of <i>anti</i> - $[(\mu\text{-SMe})_2\text{Fe}_2(\text{CO})_6]$ in the absence of acid under N_2 atmosphere	141



LIST OF SCHEMES

Scheme	Page
1.1 BDT initiation and ECEC mechanism for catalytic reduction of protons to H ₂	11
1.2 Proposed ECEC and ECECE mechanisms of PDT electrocatalyzed proton reduction from experimentally characterization by Pickett.....	15
1.3 Proposed mechanisms of catalytic proton reduction of PDT	16
1.4 DFT proposed mechanisms of catalytic proton reduction of Fp ₂	17
1.5 Proposed EECC electrocatalytic mechanism for H ₂ production of [(μ-SEt) ₂ Fe ₂ (CO) ₆].....	19
3.1 Synthesis of [(μ-SMe)(μ-SPh)Fe ₂ (CO) ₆].....	43

LIST OF SYMBOLS AND ABBREVIATIONS

α	unit cell angle between b and c dimensions
\AA	ångstrom
β	unit cell angle between a and c dimension
δ	chemical shift
γ	unit cell angle between a and b dimension
λ	wavelength
ρ	electron density
μ	micro (10^{-6})
μ	bridging mode
θ	Bragg angle or scattering angle
%	percentage
Z	number of formula units in the unit cell
Z'	number of formula units in the asymmetric unit
a	unit cell dimension a
b	unit cell dimension b
c	unit cell dimension c
A	ampere
ADF	Amsterdam density functional
a	axial position
BDT	μ -(1,2-benzenedithiolato)diironhexacarbonyl
calc.	calculated

LIST OF SYMBOLS AND ABBREVIATIONS (Continued)

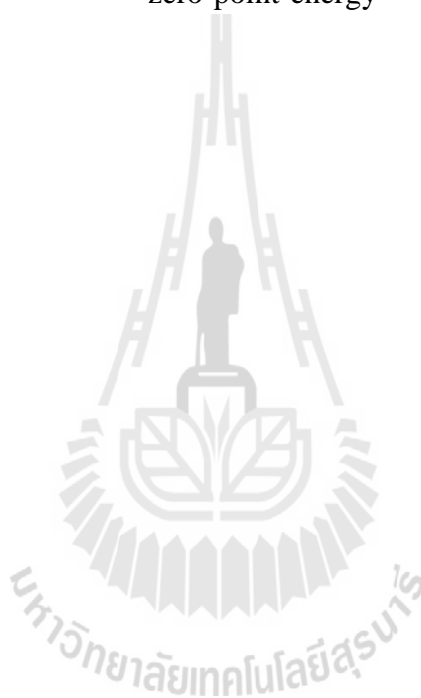
ν_{CO}	carbonyl stretching frequency
COSMO	conductor-like screening model
CV	cyclic voltammogram
$^{\circ}\text{C}$	degrees Celsius
D	density
DFT	density functional theory
eV	electron volt
e	equatorial position
XC	exchange-correlation
Fc	ferrocene
Fc^+	ferrocenium ion
Fc^+/Fc	ferrocenium/ferrocene redox couple
GGA	generalized gradient approximation
GCE	glassy carbon electrode
g	gram
HOMO	highest occupied molecular orbital
hr	hour
<i>I</i>	current
IR	infrared
<i>IE</i>	ionization energy
KE_e	kinetic energy of the photoelectron
L	litre
LDA	local density approximation

LIST OF SYMBOLS AND ABBREVIATIONS (Continued)

LUMO	lowest unoccupied molecular orbital
mp	melting point
Me	methyl group
μA	microampere
mg	milligram
mL	milliliter
mM	millimolar
mmol	millimole
min	minute
OPBE	optimized Perdew-Becke exchange
ppm	part per million
Ph	phenyl group
m^{-3}	per cubic meter
PDT	μ -(1,3-propanedithiolato)diironhexacarbonyl
R_f	retention factor
s	second
STO	Slater-type orbital
T	temperature in Kelvin
THF	tetrahydrofuran
Th	thienyl group
TZP	triple-zeta with one polarization function

LIST OF SYMBOLS AND ABBREVIATIONS (Continued)

UPS	ultraviolet photoelectron spectroscopy
V	volt
VWN	Vosko-Wilk-Nusair
VWN-Stoll	VWN function with Stoll correction
cm^{-1}	wavenumber (per centimeter)
ZORA	zeroth-order relativistic approximation
ZPE	zero-point-energy

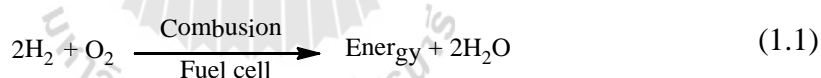


CHAPTER I

INTRODUCTION AND LITERATURE REVIEW

1.1 Hydrogen as Future Fuel

Hydrogen (H₂) is one of the most promising alternative energy fuels being considered today since H₂ is an ideally clean energy. The combustion or fuel cell processes of hydrogen, energy is obtained and only water as by product as shown in equation 1.1. This by product water is remarkable as clean enough to be a drinking water for the crews in spacecraft. Because H₂ is a carbon-free energy, it can serve to reduce demand on fossil fuels which are a contributor to the greenhouse gas CO₂ in the atmosphere (International Energy Agency, 2011).



H₂ is a flammable and explosive gas and burns with a nearly invisible flame so it requires proper handling to avoid flammable or explosive environments (Rajeshwar, McConnell and Licht, 2008). At 25 °C and atmospheric pressure, H₂ is 14.6 times lighter than air so this is an important safety consideration in that a hydrogen leak will spread out quickly. Comparison of H₂ properties with other common fuels is shown in Table 1.1. H₂ has the higher energy content per unit mass (33.3 kWh kg⁻¹) than any fuel combining with very light weight properties making it especially valuable for transportation and also spacecraft technology While energy content per volume of H₂ is low due to low density of the gaseous state.

Table 1.1 Comparison of hydrogen properties with other common fuels. At 25 °C and 1 atm for gases (Rajeshwar, McConnell, and Licht, 2008).

	Hydrogen	Methane	Gasoline	Diesel	Methanol
LHV, kJ g ⁻¹	119.9	50.0	44.5	42.5	18.1
Density, kg m ⁻³	0.0838	0.71	702	855	799
Energy density, MJ m ⁻³	10.8	32.6	31,240	36,340	14500
Energy density, kWh m ⁻³	3.0	9.1	8680	10090	4030
Energy, kWh kg ⁻¹	33.3	12.8	12.4	11.8	5.0

LHV = Lower heating value, Energy density = LHV*density,

Conversion factor, 1 kWh = 3.6 MJ.

Hydrogen is not a primary source of energy, it has been called an energy carrier, energy is chemically stored in H₂ and efficiently released as electricity by use of fuel cells. H₂ can be produced in different ways including, *e.g.* from fossil fuel such as steam reforming of natural gas and combustion of coal in which significant amounts of CO₂ are generated in the H₂ manufacture process itself. Another approach is biomass gasification, heating organic materials such as wood and crop wastes, so that H₂ is released with carbon monoxide as by product. A carbon-free method to produce H₂ is water splitting by applying electricity and generally using a platinum electrode. However electricity costs are a key factor when producing hydrogen via electrolysis and also platinum is far too expensive which limited in practical use in a hydrogen fuel cell economy (Stephens and Chorkendorff, 2011).

In nature, H₂ is efficiently produced by a class of metalloenzymes called hydrogenases normally found in green algae and cyanobacteria. Hydrogenase can produce H₂ from water via photosynthesis. Thus, the ideal goal for the hydrogen

economy would be to produce H₂ from solar power which is an ultimate source of energy as shown in Figure 1.1.

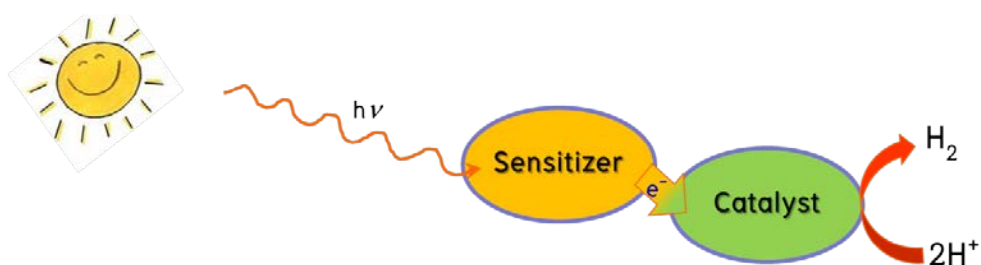


Figure 1.1 Cartoon drawing of ideal hydrogen production (Krassen, Ott, and Heberle, 2011).

1.2 [2Fe₂S] Complexes from Nature: Hydrogenase Enzymes

Hydrogenase enzymes are a family of enzyme that can catalyze the reversible two-electron reduction of two protons to yield molecular hydrogen as shown in equation 1.2. Electrons from an electron carrier combine with proton from the cell environment at the hydrogenase active site to produce H₂ (Fontecilla-Camps, Volbeda, Cavazza, and Nicolet, 2007). Hydrogenases were first discovered in colon bacteria (Stephenson and Stickland, 1931). Hydrogenase enzyme efficiently catalyzes the production of H₂ from water at neutral pH and low reduction potential about -0.100 to -0.550 V vs. NHE depending on the environment (Vignais, Billoud, and Meyer, 2001). Therefore, it is important to analyze this enzyme further to gain understanding as to how it functions.



Hydrogenase enzymes can be classified into three major groups based on the metal containing active site: i) [FeFe]-hydrogenases containing a diiron center

(Nicolet, Cavazza, and Fontecilla-Camps, 2002; Nicolet *et al.*, 2001), ii) [NiFe]-hydrogenases containing Ni and Fe in the center (Armstrong, 2004; Frey, 2002), and iii) [Fe]-hydrogenases containing a single iron atom in the active site, which do not contain iron-sulfur clusters (Shima *et al.*, 2008; Hiromoto *et al.*, 2009). The active site structures of three types of hydrogenase enzymes are shown in Figure 1.2.

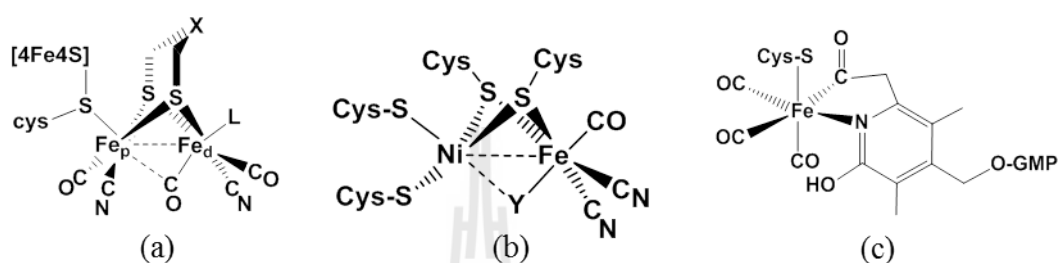


Figure 1.2 Structures of the hydrogenase active sites. a) [FeFe]-hydrogenase from *Desulfovibrio desulfuricans* and *Clostridium pasteurianum*, b) [NiFe]-hydrogenase from *Desulfovibrio Gigas*, and c) [Fe]-hydrogenase from *Methanocaldococcus jannaschii*.

Among three types of hydrogenases, the [FeFe]-hydrogenases are the most efficient catalysts known for proton reduction producing dihydrogen. All [FeFe]-hydrogenases generate H_2 at very high turnover frequencies estimated to be ~ 6000 - 9000 mol of H_2 per mol of enzyme per second and the reduction of protons occurs at very low reduction potentials, ~ -0.4 V vs. NHE correlated with -1.02 V vs. ferrocene redox couple potentials (Fc^+/Fc). This means that the energy required to reduce protons by these enzymes is low therefore the enzyme is energetically efficient for producing H_2 (Adams, 1990; Vincent, Parkin, and Armstrong, 2007).

The active site of [FeFe]-hydrogenases consists of two iron centers surrounded by CO and CN^- ligands. One carbonyl ligand resides in a semi-bridging position

between the two iron centers. While the [4Fe4S] cluster is linked to the “proximal” iron atom (Fe_p), Fe atom close to [4Fe4S] cubane, in a “butterfly” [2Fe2S] cluster, through a sulfur atom of a cysteine residue and it serves as a redox center for shuttling electrons to the [2Fe2S] active site as shown in Figure 1.3. The “distal” iron center (Fe_d), Fe atom far away from [4Fe4S] cubane, has a labile ligand site (L). The nature of this labile ligand depends on the oxidation state and environment in the catalytic cycle. If site L is occupied by a CO ligand upon exposure to carbon monoxide it can inhibit the enzyme. Therefore it has been suggested that site L is the putative hydrogen binding site during the catalysis (Gordon and Kubas, 2010).

The nature of X at the bridge-head of the dithiolate linker is not known with certainty due to the limitation of macromolecule X-ray crystallography. It was initially assigned as CH_2 but the alternative that $\text{X} = \text{NH}$ was later proposed as more likely (Nicolet, Cavazza, and Fontecilla-Camps, 2002). However, a dithiomethylether bridge ($\text{X} = \text{O}$) is also a possibility (Pandey, Harris, Giles, Peters, and Szilagyi, 2008).

Although, hydrogenase enzyme efficiently produces H_2 , the use of enzyme directly as catalyst for H_2 production is limited. Limitations of using isolated enzymes as catalysts in large scale hydrogen production are their light and air sensitivity, low natural abundance and the difficulty in the anaerobic purification process, which can easily allow the active site to get oxidized to the inactive state. Thus, the current challenge of the H_2 economy is to find an efficient synthetic catalyst for H_2 production based on inexpensive metals. Much effort has been devoted on the development of an efficient synthetic catalyst by mimicking of the hydrogenase active site instead of using the enzymes themselves.

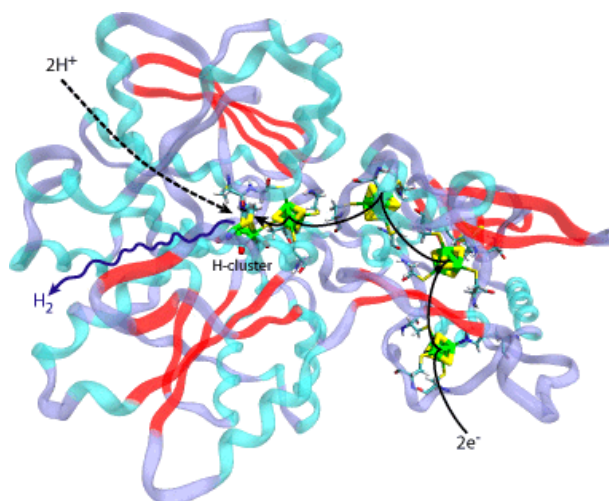


Figure 1.3 Ribbon representation of *Clostridium pasteurianum* (CpI) hydrogenase with the [FeFe] active site and [4Fe4S] clusters chain shown as capped stick models. This CpI hydrogenase image was made with VMD and is owned by the Theoretical and Computational Biophysics Group, NIH Center for Macromolecular Modeling and Bioinformatics, at the Beckman Institute, University of Illinois at Urbana-Champaign (used with permission).

1.3 [2Fe2S] Complexes for Hydrogen Production

Good progress has been made in the mimicking of the active sites of the [NiFe]- and [FeFe]-hydrogenases. Although the active sites of [FeFe]-hydrogenase and [NiFe]-hydrogenase are structurally similar, the two families are unrelated. The [FeFe]-hydrogenases are more involved in hydrogen production while [NiFe]-hydrogenases preferentially catalyze the oxidation of hydrogen and the activity of [NiFe]-hydrogenases is lower than that of [FeFe]-hydrogenases. However the latter seems to be more sensitive towards oxygen and inhibition by carbon monoxide (Frey, 2002; Hatchikian, Forget, Fernandez, Williams, and Cammack, 1992).

Several analogous molecules of the active sites of [FeFe]-hydrogenase enzymes have been synthesized, including attempts to synthesize exact models of the [FeFe]-hydrogenase active site developed by Pickett *et al.* with the formula $[\text{Fe}_4\text{S}_4(\text{SCH}_3)_3\{\text{Fe}_2(\text{CH}_3\text{C}(\text{CH}_2\text{S})_3)(\text{CO})_5\}]^{2-}$ as shown in Figure 1.4. This structure is closest to that of the [FeFe]-hydrogenase enzyme active site. The model consists of a [4Fe4S] cluster moiety containing a methylthiol link to one iron center via a S atom and was made simpler by all five diatomic ligands around Fe centers being carbonyl ligands (Tard *et al.*, 2005). The reduction potential is reported as -1.28 V vs. Fc^+/Fc while the enzyme active site is reported as -1.02 V vs. Fc^+/Fc (Adams, 1990). However, this system is not a practical catalyst for hydrogen production because this compound is too air sensitive and the synthesis method is expensive and takes multiple steps.

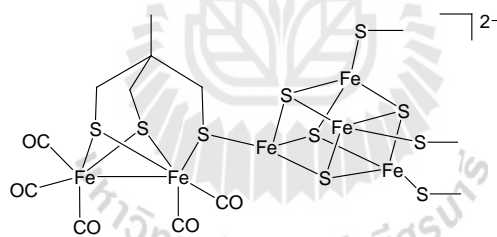


Figure 1.4 Structural diagram of $[\text{Fe}_4\text{S}_4(\text{SCH}_3)_3\{\text{Fe}_2(\text{CH}_3\text{C}(\text{CH}_2\text{S})_3)(\text{CO})_5\}]^{2-}$ (Tard *et al.*, 2005)

Even though this model compound is very similar to the native active site the reduction potential producing hydrogen is still too low. One major characteristic of a natural enzyme that is absent from the synthetic models and difficult to mimic is the protein environment surrounding the actual active site that plays an important role to aid in activity and blocking degradation.

Instead of efforts to synthetically actual enzyme active site, it may be more useful to begin with a simple model sharing similar activity to the enzyme, gain an understanding of the mechanisms, and then work towards a more complex system.

Many [2Fe2S] model complexes of the general form shown in Figure 1.5 have been reported. The well-known series is $[(\mu\text{-SRS})\text{Fe}_2(\text{CO})_6]$, when SRS is dithiolated ligand, and PR_3/CO -substituted derivatives (Seyferth, Henderson, and Song, 1982; Georgakaki, Thomson, Lyon, Hall, and Darensbourg, 2003; Capon, Gloaguen, Schollhammer, and Talarmin, 2005; Rauchfuss, 2004). In these model compounds, each iron atom is in the +1 oxidation state, and the known structures have Fe–Fe distances of 2.5–2.6 Å (Darensbourg, Lyon, and Smee, 2000; Felton *et al.*, 2007), well within the normal bonding range. As predicted by the 18-electron rule these diiron complexes are diamagnetic. The coordination geometry about iron is described as pseudo-octahedral (Teo, Hall, Fenske, and Dahl, 1975).

Most of the synthetic models are able to electrocatalyze the reduction of protons but they are all much less efficient than the enzyme (Capon, Gloaguen, Pétilion, Schollhammer, and Talarmin, 2008; Felton *et al.*, 2009). The most important criteria for a good proton reduction catalyst are i) reversibility, ii) high turnover frequency and iii) performance at low overpotential. At present, no catalyst based on the [FeFe]-hydrogenase active site has so far met these criteria satisfactorily. Thus, designing efficient synthetic models of the [FeFe]-hydrogenase active site is still challenging (Artero, and Fontecave, 2005).

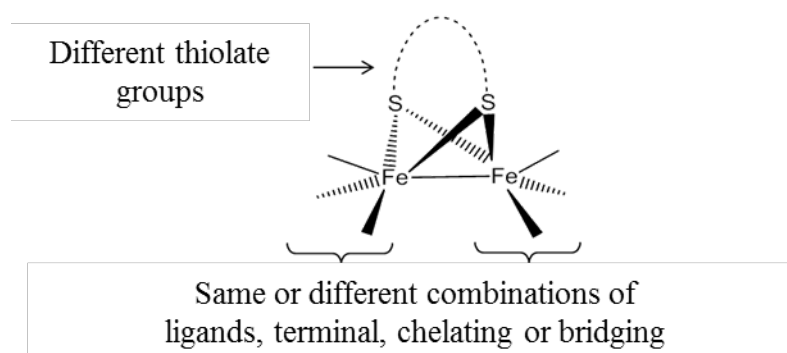


Figure 1.5 Model of general hydrogenase inspired catalysts.

Previously Studied Diiron Catalysts and Mechanisms

I. Dithiolato Diiron Hexacarbonyl, $[(\mu\text{-SRS})\text{Fe}_2(\text{CO})_6]$

The catalytic mechanisms of the $[\text{FeFe}]$ hydrogenase enzymes are still not entirely understood. Recent studies have suggested that the protonation occurs at the $[\text{2Fe2S}]$ core (Armstrong, 2004; Greco, Bruschi, De Gioia, and Ryde, 2007). This suggests the basicity of the $[\text{2Fe2S}]$ core is one of the important criteria for designing an efficient catalyst which provides a protonation site. Most of the synthetic $[\text{2Fe2S}]$ complexes are able to catalyze proton reduction, however, with different relative efficiencies and offer with different mechanisms. The combination of experimental and theoretical study leads to further understanding of the catalytically active molecular geometries and electronic properties of the synthetic models which may be crucial to understanding the catalytic mechanism of the actual enzyme.

There are many proposed mechanisms with different active catalyst intermediates for $[(\mu\text{-SRS})\text{Fe}_2(\text{CO})_6]$. The reduced intermediates proposed and/or reported in the literature include:

- i) Rotated structure: an apical CO ligand on one Fe atom rotates to bridging position between two Fe atoms and leaves an empty coordination site on that Fe atom.

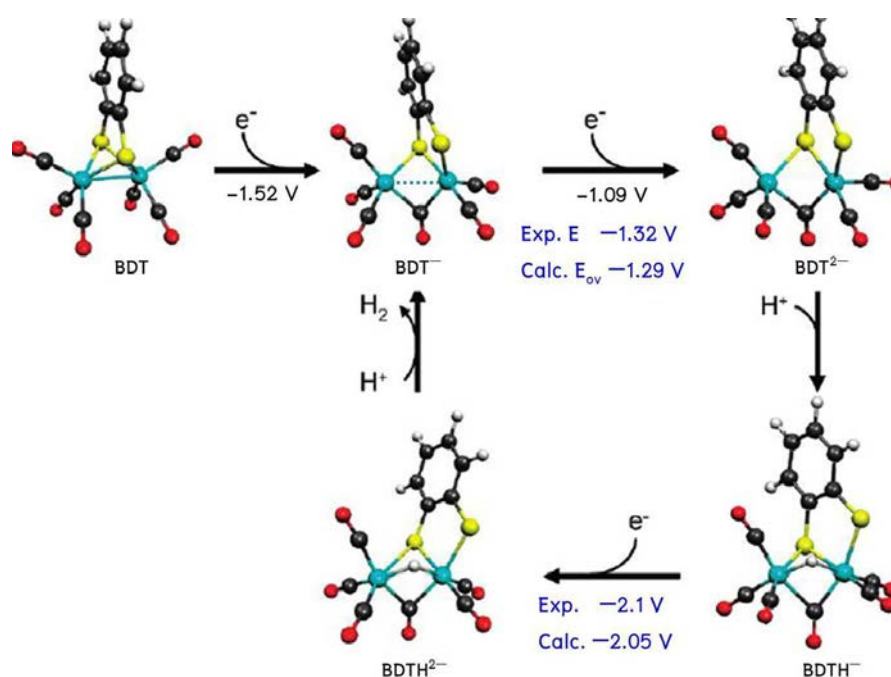
- ii) Dimerization: a reduced $[2Fe_2S]$ of a $[2Fe_2S]$ cluster dimerized with another $[2Fe_2S]$ species produced tetrairon species.
- iii) Fe–Fe bond cleavage: reduction of the Fe–Fe bond may lead to lengthening and breaking of the Fe–Fe bond.

i) Rotated Structure Intermediate

The catalytic mechanism including a rotated structure intermediate was proposed for electrocatalytic proton reduction of acetic acid by $[(\mu-1,2\text{-benzenedithiolato})Fe_2(CO)_6]$ complex (BDT) by Lichtenberger and coworkers using gas-phase *UV* photoelectron spectroscopy, electrochemistry and supporting each of these techniques with density functional theory (DFT) calculations (Felton *et al.*, 2007). An initial two electron reduction occurs at approximately -1.3 V vs. Fc^+/Fc with the peak shape being attributed to potential inversion, a process in which a second electron reduction step occurs more easily than the first electron reduction step and the average potential for the two reduction events is observed. The catalytic proton reduction occurs at about -2.1 V vs. Fc^+/Fc which is less negative compared to $[(\mu-1,3\text{-propanedithiolato})Fe_2(CO)_6]$ complex (PDT), -2.35 V (Chong *et al.*, 2003) due to the extended delocalization of electron density from the metal center to the benzene ring of the catalyst. Furthermore, a catalytic mechanism was proposed involves an electrochemical process (*i.e.* reduction), E, followed by a chemical process (protonation), C, and then a subsequent electrochemical step, E, and a final chemical step, C, to evolve molecular hydrogen as shown in Scheme 1.1. No evidence of dimerization or extensive degradation has been reported.

The DFT structure of the BDT anion showing a rotated structure, a bridging carbonyl, and one of the iron-sulfur bonds cleaved to allow an open coordination site.

This is an important feature similar to the enzyme active site. Recently, the BDT^{2-} intermediate was successfully synthesized and unambiguously characterized by X-ray crystallography as shown in Figure 1.6 which is a good validation of the DFT structure (Wright, Zhang, Yang, Fasulo, and Tilley, 2012).



Scheme 1.1 BDT initiation and ECEC mechanism for catalytic reduction of protons to H_2 . Experimental (Exp.) and calculated (Calc.) reduction potentials were shown (Felton *et al.*, 2007).

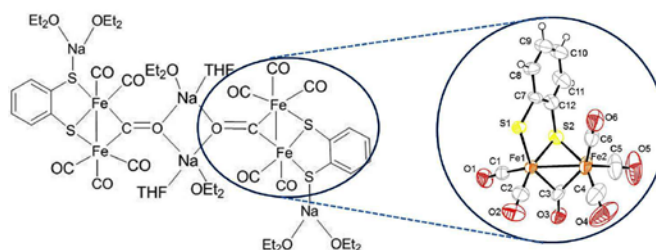


Figure 1.6 Structural diagram of $\{[\text{Na}_2(\text{THF})(\text{OEt}_2)_3][\text{BDT}^{2-}]\}_2$ (Wright, Zhang, Yang, Fasulo, and Tilley, 2012).

ii) Dimerization

In a desire to replicate a three-atom dithiolate linker which is structurally similar to that in the [FeFe]-hydrogenase active site, propanedithiolate diiron (PDT) complexes (Lyon, Georgakaki, Reibenspies, and Darensbourg, 2001; Razavet *et al.*, 2003), azadithiolate diiron (ADT) complexes (Li and Rauchfuss, 2002; Ott, Kritikos, Åkermark, Sun, and Lomoth, 2004), oxadithiolate diiron (ODT) complexes (Song, Yang, Bian, and Hu, 2004), and thiadithiolate diiron (SDT) (Song *et al.*, 2007) complexes have been studied. Among these models, the PDT and its derivatives are the most extensively studied (Georgakaki, Miller, Darensbourg, 2003; Georgakaki, Thomson, Lyon, Hall, and Darensbourg, 2003; Schwartz, Ekström, Lomoth, and Ott, 2006).

$[(\mu\text{-}1,3\text{-propanedithiolato})\text{Fe}_2(\text{CO})_6]$ (PDT)

PDT containing a three-atom bridge between the sulfur atoms was attractive because it is structurally similar to the [FeFe]-hydrogenase active site with a similar Fe–Fe distance of the [2Fe2S] core within 0.1 Å (Darensbourg, Lyon, and Smee, 2000). The initial reduction potential of PDT was reported at -1.67 V vs. Fc^+/Fc in acetonitrile (Felton *et al.*, 2009) with moderate reversibility. The second reduction potential of PDT was measured at -2.35 V, and the increase in the peak height with addition of acetic acid suggested production of H_2 via electrocatalysis (Chong *et al.*, 2003; Mejia-Rodriguez, Chong, Reibenspies, Soriaga, and Darensbourg, 2004). Previous studies have shown that the initial reduction is a one electron reduction accompanied by dimerization forming a tetrairon complex in solution and may also undergo other degradation pathways (Borg, Tye, Hall, and Best, 2007; Borg *et al.*, 2004).

The tetranuclear intermediate can be isolated by reduction of PDT in THF with one equivalent of decamethylcobaltocene (Cp^*_2Co). X-ray crystallography confirms that the structure of the reduced intermediate consists of two diiron units bridged by a propanedithiolate moiety formulated as $[\text{Fe}_2(\mu\text{-S}_2\text{C}_3\text{H}_6)(\text{CO})_5(\text{SCH}_2\text{CH}_2\text{CH}_2\text{-}\mu\text{-S})\text{Fe}_2(\mu\text{-CO})(\text{CO})_6]^{2-}$, shown in Figure 1.7.

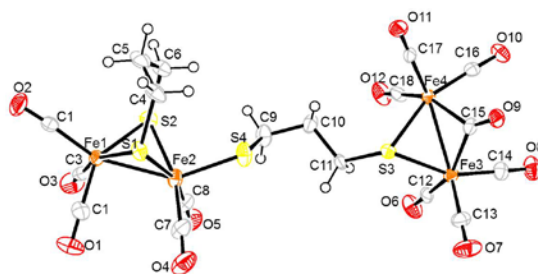


Figure 1.7 ORTEP diagram of the dimerized structure of PDT dianion with 50% thermal ellipsoids (Aguirre de Carcer, 2007).

One of the diiron units has a $\mu\text{-CO}$ ligand and six terminal CO ligands and the other diiron subunit exhibits a bridging propanedithiolate moiety. The IR spectrum of the tetrairon dianion in the CO stretching region consists of intense bands about 2010–1920 cm^{-1} corresponding to terminal CO and one lower energy band at 1736 cm^{-1} consistent with the presence of a bridging CO group. The reduction reaction of PDT can be reversed by treatment of the tetranuclear dianion with two equivalent of $[\text{Cp}_2\text{Fe}][\text{PF}_6]$, reforming PDT in near-quantitative yield (Aguirre de Carcer, 2007).

$[(\mu\text{-1,2-ethanedithiolato})\text{Fe}_2(\text{CO})_6]$ (EDT)

The reductive intermediate of EDT was proposed to be a tetrairon dianion (Best, Borg, White, Razavet, and Pickett, 2007) with a different dimer structure from PDT. The reduced intermediate was prepared by chemical reduction using

Li[HB(Et)₃] followed by addition of [N(Et)₄]Cl to allow isolation of a microcrystalline solid suitable for X-ray crystallography. The molecular structure contains a tetrairon core, [Fe₄(μ-S(CH₂)₂S)₂(μ-(CO))₂(CO)₈]²⁻, with two diiron units bridged by CO ligands and an Fe–Fe bond between two [2Fe₂S] units as shown in Figure 1.8. The IR spectrum in the carbonyl region of chemically reduced product is similar to the reduction product of EDT in solution suggesting that the species are identical.

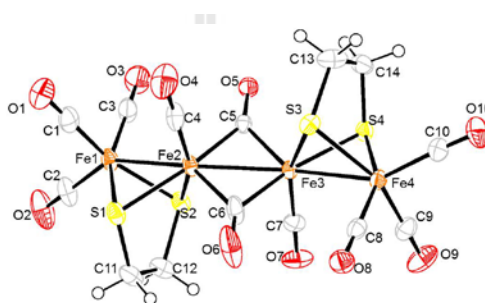
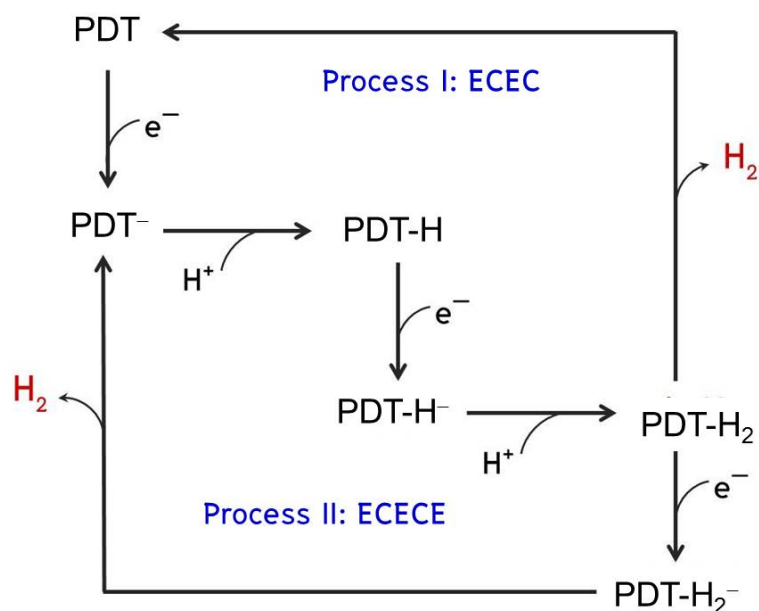


Figure 1.8 Structural diagram of [Fe₄(μ-S(CH₂)₂S)₂(μ-(CO))₂(CO)₈]²⁻ with 50% thermal ellipsoids (Best, Borg, White, Razavet, and Pickett. 2007).

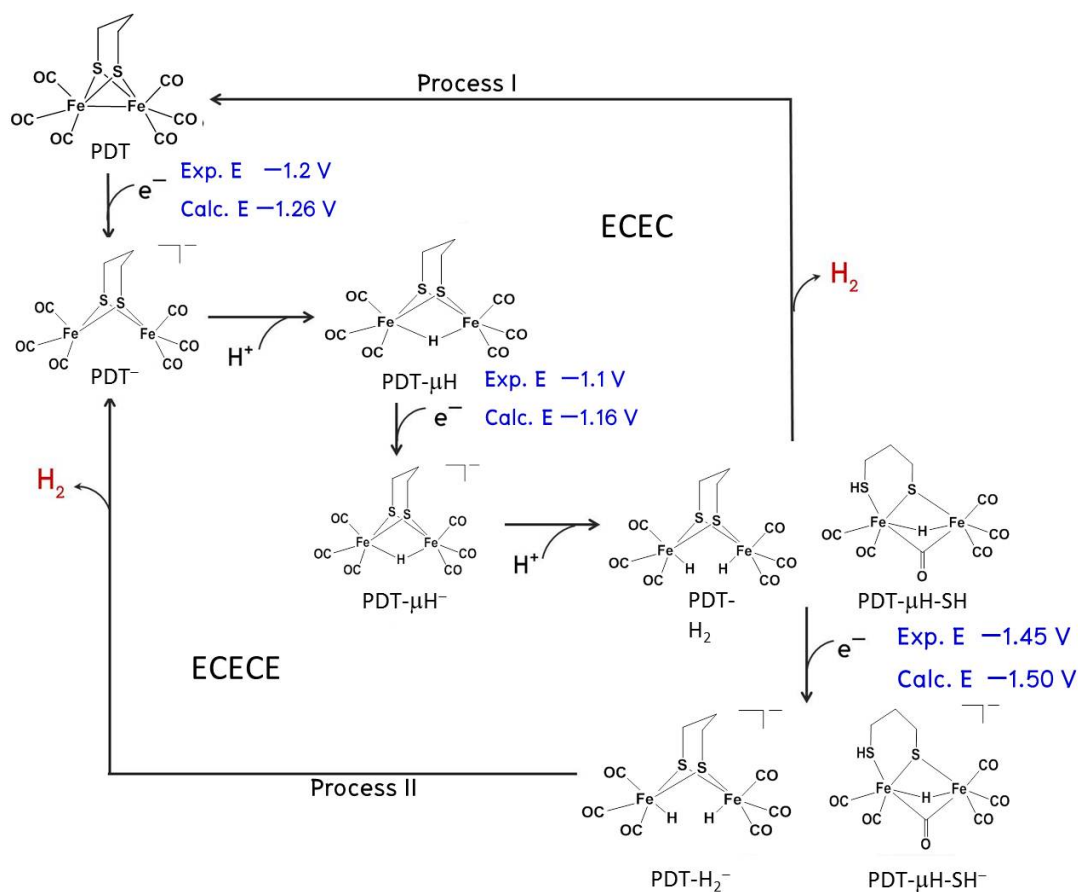
iii) Fe–Fe Bond Cleavage

PDT is one of the simplest functional models so PDT is widely used for electrocatalytic proton reduction studies. Pickett and coworkers proposed a proton reduction mechanism of strong acid, *p*-toluenesulfonic acid (HOTs), by PDT using cyclic voltammetry and spectroelectrochemistry. The proposed catalytic scheme is shown in Scheme 1.2. Process I involve ECEC mechanism similar to BDT but PDT act as active catalyst. Process II, similar to process I but there is one more electrochemical step include in final step providing ECEEC mechanism and PDT anion is active catalyst.



Scheme 1.2 Proposed ECEC and ECECE mechanisms of PDT electrocatalyzed proton reduction from experimental characterization by Pickett (Borg *et al.*, 2004).

De Gioia and coworkers used electrochemistry combined with DFT calculations to model the catalytic intermediate species in each catalytic step as shown in Scheme 1.3. The catalytic cycle starts with a monoelectron reduction with Fe–Fe bond cleavage in the anionic complex, then the first proton can protonate one iron center at this stage may due to the acid strength of used acid. The results suggest two reduction processes corresponding to two catalytic peaks observed at -1.12 V related to process I and at more negative potential -1.34 V related to process II. The $\text{PDT-}\mu\text{H-SH}$ in the catalytic cycle model is a rotated structure similar to that observed in the BDT reduced intermediate.



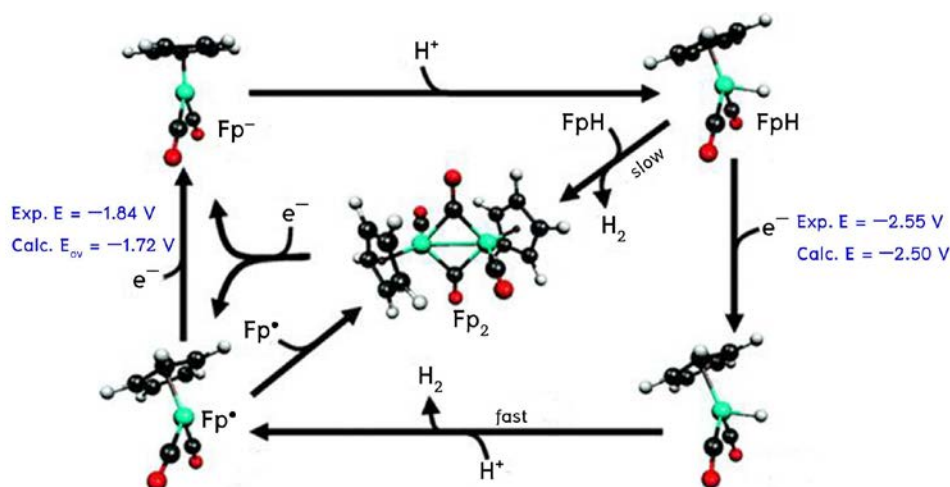
Scheme 1.3 Proposed mechanism of catalytic proton reduction of PDT. Scheme from Greco *et al.* (2007) with modification.

II. Cyclopentadienyliron Dicarbonyl Dimer (Fp_2), $[(\eta^5\text{-C}_5\text{H}_5)\text{Fe}(\text{CO})_2]_2$

Fp_2 does not contain a Fe–S bond and catalyzes the proton reduction similar to a [Fe]-hydrogenase that does not contain the $[2\text{Fe}_2\text{S}]$ cluster. Understanding the electrocatalyzed proton reduction of Fp_2 may help to propose a mechanism for similar complexes. Fp_2 has been well studied for electrocatalysis of the proton reduction and computation has been used to propose the catalytic reductive mechanism in weak acid (Felton *et al.*, 2008).

The two electron reductions break the Fe–Fe bond in Fp_2 to give Fp monomer anions that act as the active catalyst. The initial electron reduction occurs at about

-1.84 V vs. Fc^+/Fc and the catalytic peak is present at about -2.55 V vs. Fc^+/Fc for which DFT calculations give good agreement as shown in Scheme 1.4. This proposed mechanism agrees with the behavior proposed in BDT, ECEC mechanism, but has a different reduced intermediate.



Scheme 1.4 Proposed mechanism of catalytic proton reduction of Fp_2 (Felton *et al.*, 2008).

III. Bisthiolato Diiron Hexacarbonyl, $[(\mu\text{-SR})_2\text{Fe}_2(\text{CO})_6]$

Although dithiolate-bridged diiron carbonyls, $[(\mu\text{-SRS})\text{Fe}_2(\text{CO})_6]$, and their variously substituted analogues are widely studied for production of dihydrogen, they still show large overpotentials (Felton *et al.*, 2009). The lowest overpotential for electrocatalyzed proton reduction of acetic acid in acetonitrile so far reported at 0.2 V was obtained from bis-(μ -thiolato) diiron complexes, $[(\mu\text{-S-2-(4-FC}_6\text{H}_4)\text{CONHC}_6\text{H}_4)_2\text{Fe}_2(\text{CO})_6]$ (Yu *et al.*, 2008).

Many $[(\mu\text{-SR})_2\text{Fe}_2(\text{CO})_6]$ complexes such as R = methyl, ethyl and phenyl (Felton *et al.*, 2009) have been studied for electrocatalytic proton reduction and are also of interest due to the structural isomerization. There are four possible isomers

which differ in the orientation of the carbon atom α to the thiolate sulfur atoms. Structures of the possible isomers are shown in Figure 1.9. The *anti* forms refer to the axial (**a**), equatorial (**e**) substitutions (Figures 1.9a and b) which are equivalent if two thiolate ligands are the same. The *syn-endo* form refers to diequatorial substitution (Figure 1.9c), whereas the *syn-exo* form refers to diaxial substitution (Figure 1.9d) (Tye, Darensbourg, and Hall, 2006; Adeleke, Chen, and Liu, 1992). Three different isomers, **i-iii**, can exist and can be detected in solution while the sterically hindered isomer **iv** has not been observed. Computed optimized structures of these isomers on both rotated and unrotated structures agree that *syn-exo* isomer is the less stable isomeric form (Tye, Darensbourg, and Hall, 2006).

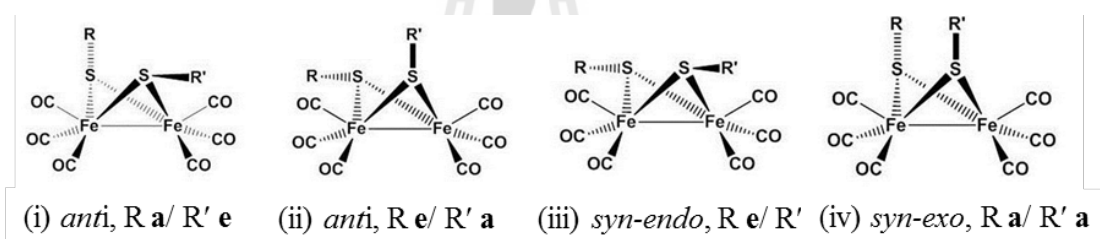
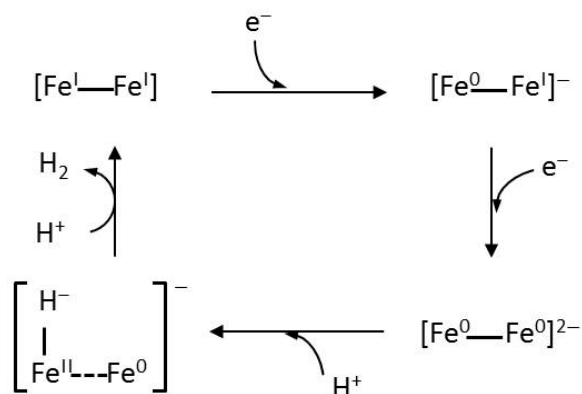


Figure 1.9 Possible isomers of $[(\mu\text{-SR})(\mu\text{-SR}')\text{Fe}_2(\text{CO})_6]$.

[Bis-(μ -ethylthiolato) $\text{Fe}_2(\text{CO})_6$]

The *syn-endo* $(\mu\text{-SEt})_2\text{Fe}_2(\text{CO})_6$ complex, initial reduction -1.31 V vs. NHE (-1.71 V vs. Fc^+/Fc) and catalytic potential at -1.94 V vs. NHE (-2.3 V vs. Fc^+/Fc). The mechanism for H_2 production was proposed to be an EECC similar to BDT and Fp_2 in presence of acetic acid as shown in Scheme 1.5.



Scheme 1.5 Proposed EECC electrocatalysis mechanism for H₂ production of [(μ-SEt)₂Fe₂(CO)₆] (Chong *et al.*, 2003).

In the absence of acetic acid, the cyclic voltammograms measured in CO-saturated or N₂-saturated CH₃CN solutions are fairly similar. In the presence of acetic acid, under N₂ an electrochemical response at -1.45 V vs. NHE (-1.85 V vs. Fc⁺/Fc) is observed and this peak disappears under CO saturated solution. This observation was interpreted to signify that the oxidative addition of a proton to the reduced Fe⁰Fe^I, to form H-Fe^{II}-Fe^I, prompts CO mobility and replacement by CH₃CN giving rise to an additional and more negative electrochemical response (Chong *et al.*, 2003). These processes are impeded by added CO, and are similar to the CO-inhibited enzyme (Bennett, Lemon, and Peters, 2000). No computational studies on the reduced intermediate structure of this model have been performed.

From study of many complexes, Lichtenberger and coworkers reported a correlation between catalytic efficiency as indicated by the catalytic current and overpotential, with a low overpotential being associated with the low catalytic current. (Felton *et al.*, 2007; 2008). Thus designing a new catalyst with low overpotential with high catalytic efficiency is still challenging.

In this work, asymmetrical bis-(μ -thiolato) diiron complexes, $[(\mu\text{-SR})(\mu\text{-SR}')\text{Fe}_2(\text{CO})_6]$ were studied to gain more insight into the electrocatalytic proton reduction mechanism of hydrogenase mimics in general. Inspired by dye-sensitized cells, thiophene and oligothiophene have received much attention for decorating the $[(\mu\text{-S}_2)\text{Fe}_2(\text{CO})_6]$ core because of their optoelectronic properties. The $[(\mu\text{-SCH}_3)(\mu\text{-SC}_4\text{H}_3\text{S})\text{Fe}_2(\text{CO})_6]$ was designed as a first step toward (μ -oligothienylthiolate) $[\text{Fe}(\text{CO})_3]_2$ for photo-assisted H_2 production.

1.4 Research Objectives

- 1.4.1) To synthesize organometallic compounds with the $[2\text{Fe}_2\text{S}]$ core, $[(\mu\text{-SR})(\mu\text{-SR}')\text{Fe}_2(\text{CO})_6]$, for hydrogenase active-site-inspired catalysts.
- 1.4.2) To study the synthesized complexes by spectroscopic techniques and to investigate the catalytic hydrogen production by electrochemical methods.
- 1.4.3) To gain an understanding of the proton reduction mechanism by combining computational and experimental results.

CHAPTER II

GENERAL BACKGROUND

Organometallic compounds contain at least one metal carbon bond. One potential application of organometallic compounds is the use of organometallic compounds as catalysts. The structure of enzyme active sites can inspire the development of organometallic catalysts. The active-site of the [FeFe]-hydrogenase enzyme (Nicolet *et al.*, 2001) inspires for a dihydrogen production catalyst (Darensbourg, Lyon, and Smees, 2000). Synthesis and characterization of complexes that are closely related to enzyme active sites allows simplification of the investigation into the fundamental properties of the active sites (Felton *et al.*, 2007; Lyon, Georgakaki, Reibenspies, and Darensbourg, 1999; Tard *et al.*, 2005). Many techniques such as cyclic voltammetry, photoelectron spectroscopy, infrared spectroscopy, and density functional theory calculations can be combined to gain understanding of the active-site inspired complexes. Each technique offers unique information about the complexes, and contributes to a complete analysis of their properties.

The synthetic techniques for preparing the [FeFe]-hydrogenase catalyst mimics are also important because the preparation of these compounds generally start from air and/or moisture sensitive reagents such as diiron nonacarbonyl (Cabeza, Martinez-Garcia, Riera, Ardura, and Garcia-Granda, 1998), iron pentacarbonyl (Seyferth, Henderson, and Song, 1982), Grignard reagents, organolithium compounds (Seyferth, Henderson, Song, and Womack, 1985). Therefore, the experiments dealing

with these types of compounds were carried out using air-free techniques when it need.

2.1 The Manipulation of Air-Sensitive Compounds

Many different routes to prepare model complexes of the active site have been developed (Capon, Gloaguen, Petillon, Schollhammer, and Talarmin, 2008; Seyferth, Henderson, Song, and Womack, 1985). The two most common types of air-free technique involve Schlenk lines and gloveboxes.

Schlenk and Vacuum Line Techniques

Schlenk and vacuum lines as shown in Figure 2.1 consist of a glass double manifold, one side connected to a vacuum pump and the other side to an inert gas supply such as Ar or N₂. Two manifolds joined by series of T-valves which allow switching the workstation between inert gas and vacuum, and allow several pieces of apparatus to be independently used at the same time.

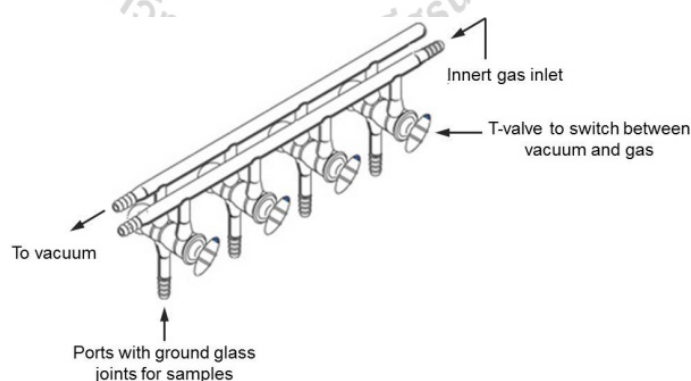


Figure 2.1 Double manifold for Schlenk line. Figure from Ctech Global Pte Ltd (used with permission).

Attached to the manifold are a source of purified nitrogen or argon gas and a source of vacuum. The source of purified nitrogen has an oil bubbler which serves as an approximate flow indicator. The vacuum part of the Schlenk line is a mechanical pump connected to a low-temperature trap to protect the pump from harmful vapors. The trap has to be submerged in a Dewar container with liquid nitrogen (or an isopropanol/dry ice bath), when the pump is running. The choice of dry ice or liquid nitrogen to cool the trap depends on the volatility of the solvents being used. Use of dry ice is only possible when all the solvents are high boiling liquids. This trap must be of large volume and easily removable since it may accumulate a considerable amount of condensate. For reactions which are completed in a relatively short time or for moderately air sensitive materials Tygon tubing is acceptable for connecting the various components. If the reactions have greater air sensitivity or the length of reaction time is long, butyl rubber tubing must be used to solve the problem of gas diffusion which occurs with Tygon tubing.

Inert Atmosphere Glovebox

The inert atmosphere glovebox provides a straightforward method for handling air-sensitive compounds without having to use complicated Schlenk-like glassware. Gloveboxes maintain their inert atmosphere either by constant purging of the box with a positive pressure of inert gas, or by removing the moisture and oxygen from the inert atmosphere of the glovebox by recycling an inert atmosphere through a catalyst. In its simplest form, a glovebox consists of the actual box which is a large aluminum chamber with a plastic front window and a pair of gloves, and an airlocked antechamber to facilitate taking things in and out of the box without admitting air. The entire box is flushed with an inert gas to remove any air or water from the working chamber. The pressure regulator is an important component for the glovebox.

The chamber pressure is set to tolerate only a few millibar of positive and negative pressure and automatically pumps nitrogen out if the pressure gets too high or draws fresh nitrogen in from a tank if the pressure gets too low. The chamber pressure can also be regulated manually with a foot pedal (Shriver and Drezdson, 1986). Some volatile chemicals absolutely cannot be used in the glovebox because they will permanently poison the catalyst. Typically, for gloveboxes employing copper-based catalysts the following volatile chemicals should be avoided: amines, halogenated solvents, alcohols, phosphines, and thiols.

Drying and Degassing Solvents

Solvents which have been exposed to the atmosphere contain appreciable amounts of dissolved gases and water that should be eliminated before use. This can become a major task especially when the reagents to be used are sensitive towards water, *e.g.* Grignard reagents. Distillation is one method for purification of organic solvents. Water containing in solvent can often be removed by distillation and O₂ can be simply removed by bubbling inert gases through the solvent for some period of time.

Freeze-Pump-Thaw is one of the most effective ways to degas volatile solvents in a Schlenk and/or vacuum line. This is accomplished by:

- 1) Freeze: cool the solvent to liquid nitrogen temperature to freeze it.
- 2) Pump: apply a vacuum to the solvent at this temperature.
- 3) Thaw: close the stopcock or valve so the solvent is isolated from the vacuum, and allowing the sample to melt.
- 4) Refreeze and pump it away any noncondensable gases which boiled out of the materials.

This process is generally repeated several times. NOTE liquid nitrogen may break glass apparatus when they are quickly thawed. The easiest course of prevention is to use a round-bottomed container which is one-fourth full or less.

Liquid Transfer Techniques

Syringe: Moderate accuracy in liquid transfer operations can be achieved using syringe graduations. The syringe should be flushed with inert gas before filling, and air should be expelled from the filled syringe by pointing the needle up and squirting out all bubbles before use.

Cannulation: The transfer of liquids between two flasks may be accomplished with a cannula. A cannula is usually made from stainless-steel syringe needle stock which is commercially available in convenient lengths. The diagram of cannulation set up shown in Figure 2.2. The solution is forced through the cannula by a pressure differential between two flasks created by opening the inert gas inlet to the flask that contains the solution to be transferred. This would pressurize the receiving flask so the sidearm of the receiving flask is either opened to the bubbler to maintain 1 atm pressure, or is briefly opened to the vacuum source to maintain slightly less than 1 atm of pressure. In comparison with syringe techniques, the use of cannula provides better air exclusion and greater convenience for the transfer of large volumes of solution. However, syringe techniques are much better suited for the quantitative dispensing of liquids.

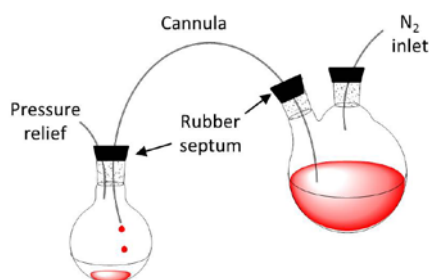


Figure 2.2 Solution transfer using a stainless-steel cannula.

Low Temperature Baths

Low temperature baths are useful in air sensitive techniques. In case we need to add solid to a reaction mixture, we can open the reaction flask stopcock and quickly add solid reagent because cooling of reaction mixture to very low temperature can slow air diffusion into the reaction mixture. The simplest and cheapest cooling bath is an ice/water mixture, which maintains a temperature of 0 °C. For lower temperatures, three main types of cooling baths are typical:

Ice: A slurry of ice and an inorganic salt such as sodium chloride or calcium chloride provide temperatures down to about -40 °C. The temperature depends on the amount and type of salt used, based on the freezing point depression effect.

Dry ice baths: Dry ice baths are less reliable in temperature because the equilibrium temperature strongly depends on the partial pressure of CO₂ above the bath. For example, dry ice freshly powdered in air had a temperature 8 °C, below the normal sublimation temperature of -78 °C. At atmospheric condition, a slurry of dry ice and a suitable organic solvents, such as acetone, can also provide temperatures down to about -78 °C.

Liquid nitrogen: Liquid nitrogen is the most commonly used refrigerant for the manipulation of the condensation materials on a vacuum system because it is easy to use, inexpensive, will not support combustion and can provide temperatures down to about its boiling point of -196 °C (77 K). Furthermore, its boiling point is low enough to lower the vapor pressure of most materials below 10⁻³ torr, which is necessary for the quantitative transfer of condensable materials on the vacuum system. Liquid nitrogen should be stored in Dewars, metal tank with insulator and narrow-mouth. NOTE never seal a Dewar of liquid nitrogen, because the insulation on

a Dewar is never perfect, so the liquid is constantly boiling and a sealed Dewar will eventually explode.

Adding of organic solvents to low temperature baths can provide wide range of low temperature as show in Table 2.1

Table 2.1 Common cooling bath mixtures (Gordon and Ford, 1972).

Mixture	Temperature (°C)
Ethylene glycol/CO ₂	-15
CCl ₄ /CO ₂	-23
MeCN/CO ₂	-42
Acetone/CO ₂	-77
MeOH/N ₂	-98
n-Pentane/N ₂	-131

2.2 NMR Spectroscopy

Synthetic model complexes normally have an initial Fe(I)-Fe(I) oxidation state, each Fe(I) has a d^7 electron configuration and the unpaired electron from each Fe contribute to Fe-Fe bond which each iron satisfies the 18-electron rule. Thus, the complexes are diamagnetic and can be studied by NMR spectroscopy. In this work, NMR is use as a basic technique for preliminary structural characterization. In the current system, $(\mu\text{-R})_2\text{Fe}_2(\text{CO})_6$, NMR spectroscopy is a useful tool to identify the isomeric form of the complexes because the orientation of the thiolated ligand around iron centers is different in each isomeric form and they can be distinguished by NMR chemical shifts (Seyferth, Henderson, Song, and Womack, 1985).

2.3 IR Spectroscopy

An IR spectrum results from the energy transition between different vibrational modes of a molecule. In order for the vibrational mode to be IR active the vibration must produce a change in dipole moment. Therefore, it is a useful technique to study polar groups such as the carbonyl or cyanide ligand that exhibit strong absorptions or high intensity stretching bands in the IR spectrum. The vibrational frequencies for stretching bonds in molecules are related to the strength of the chemical bonds and the masses of the atoms. The C≡O vibration (ν_{CO}) in free carbon monoxide gas occurs at 2143 cm^{-1} . When coordinated to a metal, the carbonyl stretching frequency is decreased (terminal, $1850\text{--}2150\text{ cm}^{-1}$ and bridging, $1700\text{--}1850\text{ cm}^{-1}$). There are three metal–CO bonding interactions: i) CO to metal σ -bonding, ii) metal to CO π -backbonding and iii) CO to metal π -bonding, as shown in Figure 2.3.

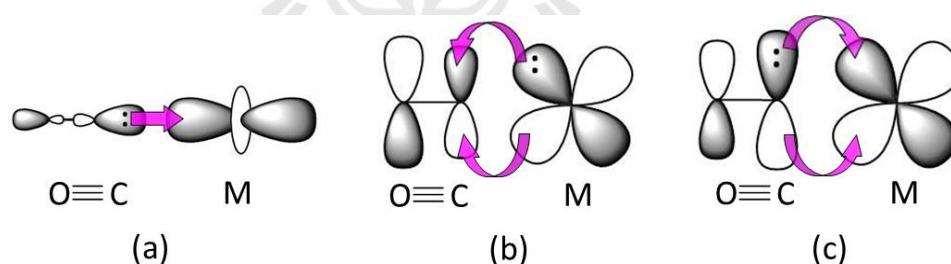


Figure 2.3 Three types of metal–CO interactions. (a) CO to metal σ -bonding, (b) metal to CO π -backbonding, and (c) CO to metal π -bonding (Schwartz *et al.*, 2008).

The lowest unoccupied molecular orbital (LUMO) of CO is a π^* antibonding orbital, shown in Figure 2.4, that acts as an acceptor orbital when interacting with filled d-orbitals on metals. This is the reason why coordination to electron rich metal

centers shifts the ν_{CO} stretching frequency to lower energy as the $\text{C}\equiv\text{O}$ bond weakens due to the d to π^* backbonding. Another factor that affects CO stretching frequency is the coordination mode of the carbonyl ligand to metal such as terminal, μ_2 -bridging, or μ_3 -bridging mode. The synergic bonding (*i.e.* σ bonding and π^* backbonding) between the CO ligand and the metal center renders IR spectroscopy a very powerful tool to probe the electronic environment in metal-carbonyl complexes.

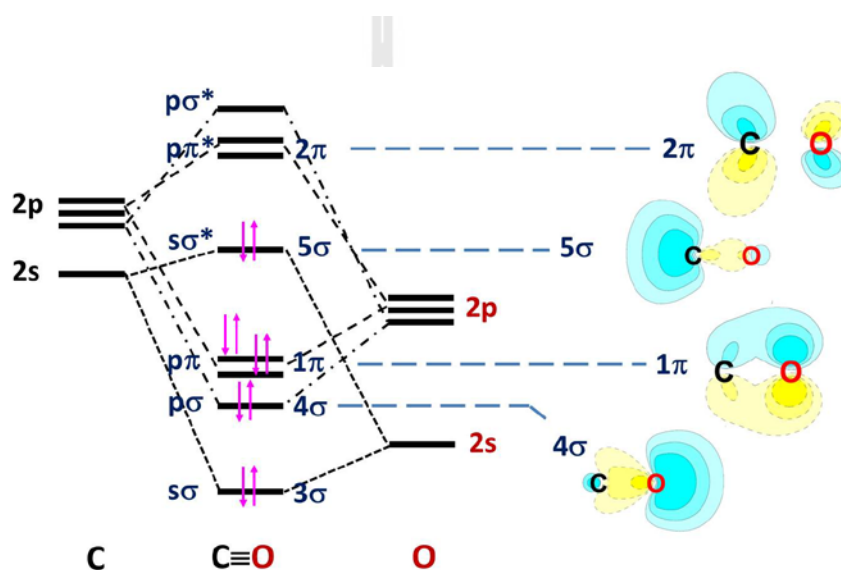


Figure 2.4 Molecular orbital diagram of carbonyl. Figure modified from Lichtenberger, The University of Arizona (2011).

For diiron dithiolate hydrogenase mimics, the thiolate ligands also affect the electron density on the iron centers. IR spectroscopy is a powerful technique to investigate this phenomenon by looking at the CO stretching region (2200-1600 cm^{-1}). The electron density at the diiron center determines the magnitude of backbonding from metal d orbital into the CO antibonding orbitals which affects the CO stretching frequencies in the IR spectrum (Petro *et al.*, 2008; Si, Hu, and Chen, 2008; Tye, Darensbourg, and Hall, 2006; Zilberman, Stiefel, Cohen, and Car, 2007).

IR spectrum in carbonyl stretching region of some $[\text{Fe}_2(\mu\text{-S}_2\text{R})(\text{CO})_6]$ complex are shown in Figure 2.5 and shift depending on the electronic properties of the bridging dithiolate ligand (Schwartz *et al.*, 2008; Schwartz, Singh, Eriksson, Lomoth, and Ott, 2008).

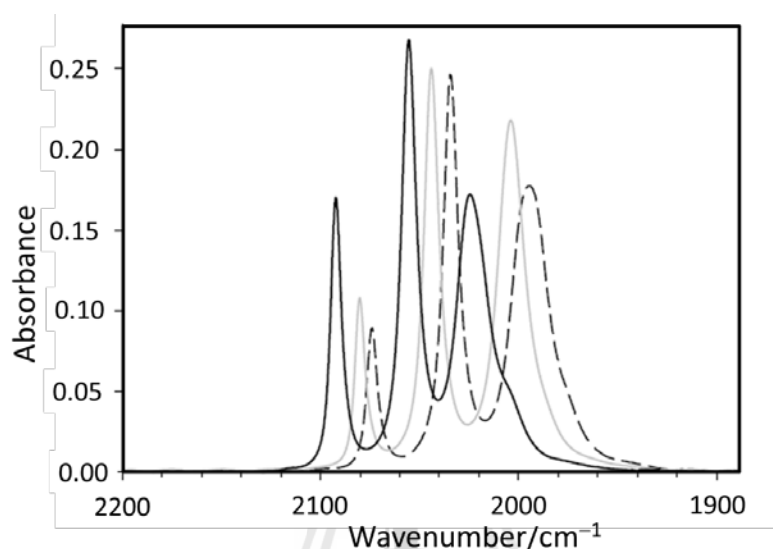


Figure 2.5 IR spectrum in carbonyl stretching region of $\text{Fe}_2\text{cdt}(\text{CO})_6$ (black line) $[\text{Fe}_2(\mu\text{-bdt})(\text{CO})_6]$ (gray line) and $[\text{Fe}_2(\mu\text{-pdt})(\text{CO})_6]$ (dashed line) in CH_3CN . cdt = carborane dithiolate, bdt = benzene-1,2-dithiolate, pdt = propane-1,3-dithiolate (Figure from Schwartz *et al.*, 2009).

2.4 Gas-phase Ultraviolet Photoelectron Spectroscopy

Gas-phase ultraviolet photoelectron spectroscopy (UPS) is the technique for giving the most direct probe of electronic structure of a compound in the absence of intermolecular interactions from the surrounding environment by measuring kinetic energies of outgoing electrons (Solomon, Basumallick, Chen, and Kennepohl, 2005; Gruhn *et al.*, 2002). UPS is based on Einstein's photoelectric effect (Einstein, 1905) shown in Figure 2.6. A photon ($h\nu$) can remove an electron from a material if the

photon's energy is greater than the electron binding energy, and any photon energy in excess is carried by the outgoing electron in the form of kinetic energy (KE_{e^-}).

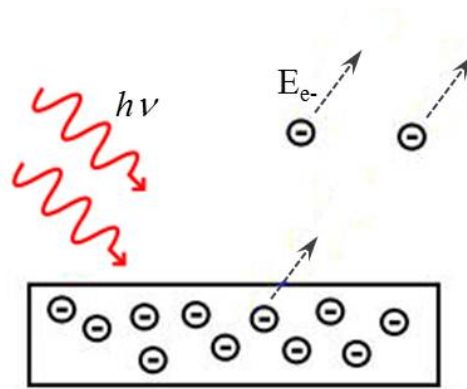


Figure 2.6 Schematic illustration of the photoelectric effect. Figure modified from Lichtenberger, The University of Arizona (2004).

The kinetic energy of the ejected photoelectron is measured by a photoelectron spectrometer. The difference between the photon energy, which is known, and the electron kinetic energy, which is measured, is the ionization energy (IE) as shown in equation 2.1.

$$h\nu = IE + KE_{e^-} \quad (2.1)$$

The UPS instrument is based on 3 steps

- 1) Photon induced photoelectric effect
- 2) Ejected electron are separated according to kinetic energy
- 3) Photoelectron are counted and plotted between ionization energy and electron count.

UPS components consist of five main parts as shown in Figure 2.7.

- 1) Photon source is gas discharge source in quartz discharge tube.

He I source applies power in negative polarity, 1000 V and 150 mA, photon energy 21.2 eV.

He II source applies power in positive polarity, 1000-1100 V and 250 mA, photon energy 40.8 eV.

- 2) Sample chamber is aluminium or stainless steel sample cell depending on the sublimation temperature of sample. An aluminium cell is used for high volatile sample or low sublimation temperature and stainless steel sample cells are used for high sublimation temperature for low volatility samples.
- 3) Electron kinetic analyzer hemispherical stainless steel coated with graphite in isopropanol solution to prevent electron scattering.
- 4) Detector/electron counter is a Channeltron single channel electron multiplier as used in mass spectroscopy
- 5) Vacuum system is turbopump and drive backing pump

UPS needs low pressure $\sim 10^{-6}$ torr to

- operate Channeltron (detector)
- provide sufficient mean-free-part for the photoelectron
- permit large neutral molecules to be introduced into the gas phase

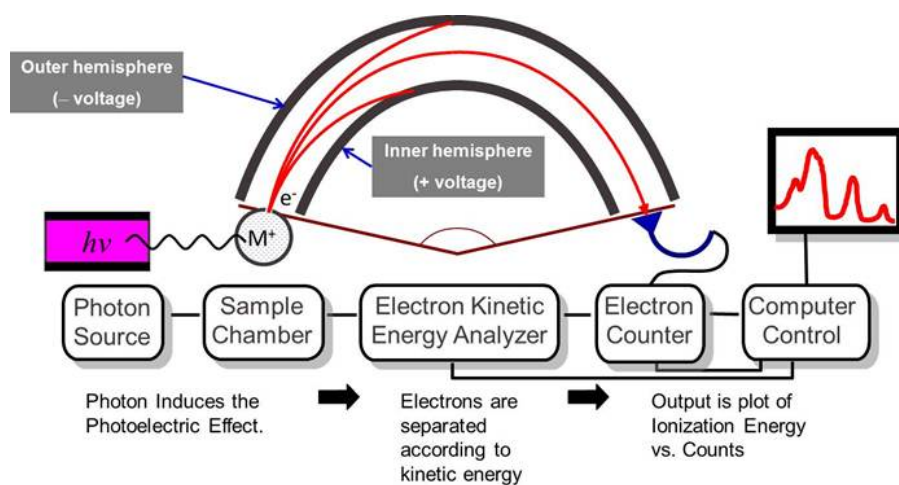


Figure 2.7 Components of a gas phase UPS instrument. Figure from Lichtenberger, The University of Arizona (2004).

2.5 Cyclic Voltammetry

Cyclic voltammetry (CV) is a tool commonly used in the electrochemical characterization of redox-active compounds. A cyclic voltammogram is a plot of current versus the applied potential and it generally displays a peak in the current-potential plot (I - E plot) on both the forward and reverse scans. The CV apparatus is computer controlled. It consists of a potentiostat with scan capability and contains a display of current versus potential. A three electrode system is typically used consisting of a working electrode, counter electrode, and reference electrode. The electrochemical cell-top contains four holes. One for each of the electrodes and one for introducing an atmosphere of gas (typically used for deoxygenation by bubbling a stream of nitrogen prior to measurement).

From the I - E plot or voltammograms, the magnitude of the peak is called the peak current (I_{pa} and I_{pc}) and the position of the peak along the potential axis is called the peak potential (E_{pa} and E_{pc}). A CV can be used to determine if a redox process is reversible, such as determining if a reduced product is stable on the time scale of the electrochemical experiment. This is determined by comparing the peak currents, I_{pc} and I_{pa} , and differences in potentials for the reduction and subsequent oxidation of the reduced species during the forward and reverse scans and vice versa.

The ferrocenium/ferrocene (Fc^+/Fc) redox couple is an example of a well-behaved electrochemically reversible system in acetonitrile solution as shown in Figure 2.8. Nearly equivalent amounts of current, I_{pc} and I_{pa} , indicate chemical reversibility, suggesting the complex is robust. The (Fc^+/Fc) redox couple as shown in equation 2.2 is often used as a pseudo reference when reporting formal potentials of inorganic/organometallic complexes and is also commonly used as an internal standard for calibrating reduction and oxidation potentials makes them an ideal

molecular system for investigating the relation of energies between onset ionization energy (IE) and half wave reduction potential ($E_{1/2}$)

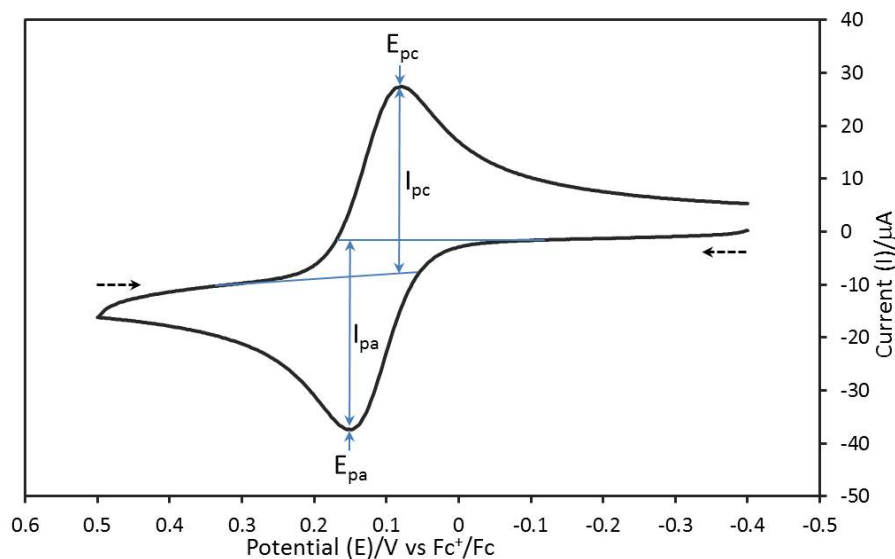


Figure 2.8 Cyclic voltammogram of ferrocene in acetonitrile representing a reversible process.

Voltammetry and Catalytic Efficiency for Hydrogen Generation

Voltammetry is widely used for the evaluation of hydrogenase mimics and other potential catalysts for hydrogen generation using various dipolar aprotic solvents. The most important properties for a good proton reduction catalyst that can be determined from cyclic voltammogram are i) reversibility, ii) high catalytic peak current corresponding to acid concentration, and iii) performance at low overpotential. The overpotential for catalytic production of hydrogen using acids as proton source is defined by the difference between the standard potential for proton reduction of acid, E°_{HA} , and the potential at which catalysis occurs. E°_{HA} is defined by the half reaction

in equation 2.3, where HA represents a weak acid of known pK_a . (Felton, Glass, Lichtenberger, and Evans, 2006)



Effective catalysts show enhanced current in the presence of a proton donor at the potential where the catalyst precursor is reduced. It is thermodynamically impossible for reduction of acid to occur at less negative potentials than the standard reduction potential of acid, the most effective catalysts will operate at potentials as close as possible to the reduction of acid (E°_{HA}). The pK_a and E°_{HA} of some acid use as proton sources in proton reduction are listed in Table 2.2. In addition, direct reduction of acid (reduction of just acid itself) at the electrode surface may compete with the catalyzed reduction. The type of electrode greatly influences the range of reduction potentials that can be detected and direct reduction of acid, thus the choice of electrode is important to keep in mind. The voltamograms of acetic acid using different electrodes are shown in Figure 2.9 and the standard reduction potential of acetic acid producing molecular hydrogen occurs at $-1.46 \text{ V vs. Fc}^+/\text{Fc}$ (indicated as vertical dotted line in the graph for comparison). Platinum (Pt) electrode shows direct reduction of acetic acid at about $-1.7 \text{ V vs. Fc}^+/\text{Fc}$ which is quite a small overpotential, so direct reduction can directly interfere with the peak current from the actual catalysis event. Glassy carbon (GC) electrodes, commonly used in such evaluations, show a larger overpotential for direct reduction of acid however, catalysis at very negative potentials will be contaminated by significant direct reduction of acid. The direct reduction at a mercury (Hg) or amalgamated gold (Au(Hg)) electrode occurs at high negative potentials about $-2.7 \text{ V vs. Fc}^+/\text{Fc}$ so it can avoid contamination of catalytic with direct reduction.

Table 2.2 Acid dissociation constants (pK_a) and standard potentials for the HA/A⁻, H₂ half reaction of some acids in acetonitrile (Felton, Glass, Lichtenberger and Evans, 2006).

acid	pK_a	$E^\circ_{\text{HA vs. Fc}^+/\text{Fc}}$
perchloric acid	2.1	-0.26
trifluoromethanesulfonic acid	2.6	-0.29
<i>p</i> -toluenesulfonic acid	8.7	-0.65
methanesulfonic acid	10.0	-0.73
trichloroacetic acid	10.6	-0.77
dichloroacetic acid	13.2	-0.92
chloroacetic acid	15.3	-1.05
4-nitrophenol	18.5	-1.36
benzoic acid	20.7	-1.36
acetic acid	22.3	-1.46
phenol	27.5	-1.75

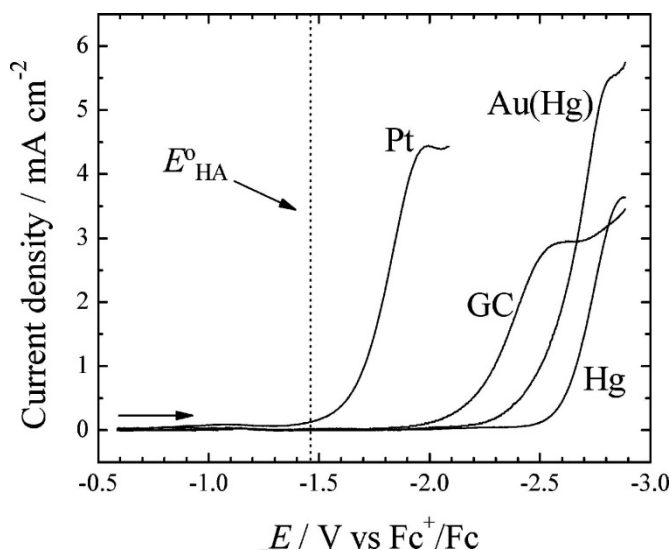


Figure 2.9 Linear sweep voltammograms of 10 mM acetic acid in acetonitrile at various electrodes as indicated. 0.10 M Bu_4NPF_6 supporting electrolyte and 1.0 V/s scans. The electrode areas differed so the current density has been plotted. The reversible potential for reduction of acetic acid (-1.46 V vs. Fc^+/Fc) is shown as a dotted line for comparison (Figure from Felton *et al.*, 2006).

There are other sources of current that can interfere with the catalytic current which may be Faradaic or other background currents. Faradaic disturbance may be the electrolysis of impurities, electrolyte electrolysis, electrode material reaction, while capacitive currents are the major non-Faradaic source of error. This can be corrected by subtracting the background current from the current of electrocatalyzed proton reduction.

2.6 X-ray Crystallography

X-ray crystallography is the most powerful and unambiguous method for structure determination. The basic requirement to conduct an X-ray diffraction

experiment is a single crystal of suitable size that can hold out exposure to X-rays of a given energy for the duration of the X-ray experiment. The mathematical expression used to describe how X-rays interact with a crystal to produce a diffraction pattern is given by Bragg's Law (Equation 2.4):

$$n\lambda = 2d\sin\theta \quad (2.4)$$

Where: n is an integer, λ is the wavelength of the radiation, d is the perpendicular spacing between adjacent planes in the crystal lattice, θ is the angle of incidence and reflection of the X-ray beam as shown in Figure 2.10.

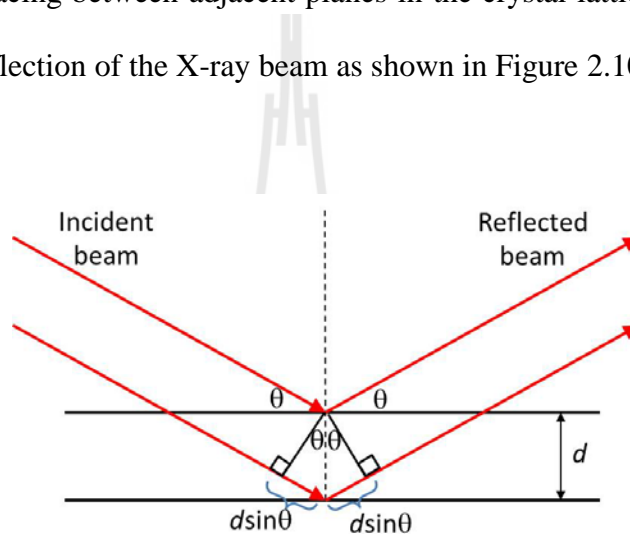


Figure 2.10 Reflection of X-ray beams relative to planes of atoms in a solid (Scintag, 1999).

X-ray data collected from a single crystal diffraction yields an intensity, Miller indices, and the diffraction angle (2θ) for each reflection. The intensity of the reflection depends on the nature and arrangement of the atoms in the unit cell and 2θ is dependent only on the dimensions of the crystal lattice. For reflection to occur, Bragg's law must be satisfied. In general, the structure solution can be obtained from direct or Patterson methods and refined by least square refinement. The success or quality of the refined structure can be assessed in several ways, the most important

one is discrepancy indices. When we compare the observed structure factors (F_o) with those calculated from the correct model (F_c) they must agree. The conventional discrepancy index (or residual) is defined as in equation 2.5.

$$R_1 = \frac{\sum(|F_o| - |F_c|)}{\sum|F_o|} \quad (2.5)$$

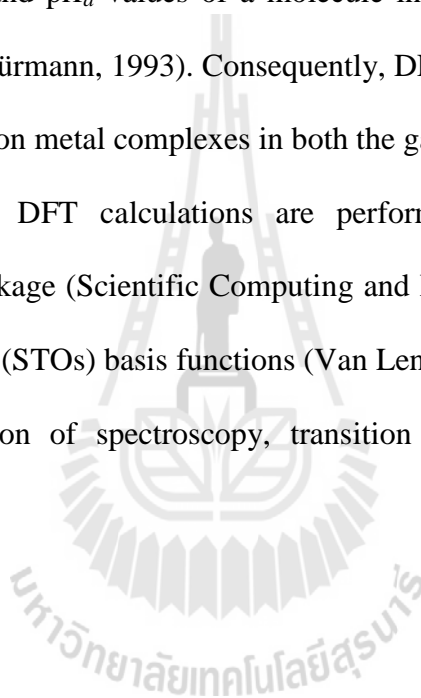
For perfect data and a perfect model R_1 would be zero. Discrepancy indices in the range of 0.02-0.05 (2-5%) are common for the most reliably determined structures of small molecules.

2.7 Density Functional Theory

Density functional theory (DFT) calculations have become an important and widely utilized tool for the understanding and prediction of many chemical properties, structure, and experimental observables such as reactivity and spectroscopy. DFT methods are appealing for computations on large molecules or complexes containing transition metals because of the inclusion of electron correlation effects at a low computational cost. DFT is based on approximations of the exchange-correlation (XC) functions that describe the effects of the Pauli principle and the Coulomb potential beyond a pure electrostatic interaction of the electrons. The XC functionals are semi-empirical and the two common approximations are local density approximation (LDA) (Kohn and Sham, 1965; Ceperley and Alder, 1980) and generalized gradient approximation (GGA). LDA approximations such as VWN (Vosko, Wilk, and Nusair, 1980) and VWN-Stoll (Stoll, Pavlidou, and Preuß, 1978) approximate the XC function of the uniform electron gas at every point in the system regardless of the homogeneity of the real charge density. GGA approximations such as OPBE (Swart, Ehlers, and Lammertsma, 2004) and PBE (Perdew, Burke, and

Ernzerhof, 1996), approximate the XC function of the nonuniform electron charge densities by correcting charge density deviation of the system using the gradient of the atomic charge density. Advancements of solvation calculations through the conductor like screening model (COSMO), a dielectric model in which the solute molecule is embedded in a molecule-shaped cavity surrounded by a dielectric medium with given dielectric constant (solvent), allowed for prediction of solvation energies, reduction potentials, and pK_a values of a molecule in a variety of solvents (Klamt, 1995; Klamt and Schüürmann, 1993). Consequently, DFT proves to be a valuable tool for analysis on transition metal complexes in both the gas-phase and solution-phase.

In this work, DFT calculations are performed on Amsterdam Density Functional (ADF) package (Scientific Computing and Modelling, 2010) which based on Slater-type orbitals (STOs) basis functions (Van Lenthe and Baerends, 2003). ADF allows the computation of spectroscopy, transition metals, and heavy elements problems.



CHAPTER III

EXPERIMENTAL

3.1 Preparation of Materials

All reactions were performed under Ar atmosphere using standard Schlenk line techniques. All glassware was dried in a 110 °C oven overnight before use. Commercially available chemicals, iron pentacarbonyl (Aldrich, >99.99%), 2-bromothiophene (Aldrich, 98%), bromobenzene (Aldrich, 99%), iodomethane (Aldrich, 99%) and DrysolTHF were used as received. Solvents were deoxygenated by bubbling Ar through them for 30 min prior to use or used directly from a MBraun solvent purification system (EMD Omnisolv). All reactions were monitored by solution IR spectroscopy of the CO stretching region and/or by TLC on Merck aluminum TLC sheets. Work up and chromatographic separations were carried out in air using silica gel columns with pentane or hexane as eluents. Product yields were calculated based on utilized $[(\mu\text{-S})_2\text{Fe}_2(\text{CO})_6]$. Infrared spectra were collected in mineral oil or in hexane on round sodium chloride cells using a Nicolet 380 FT-IR spectrophotometer. ^1H and ^{13}C NMR spectra were acquired at room temperature on a Bruker AVIII 400 spectrometer using CDCl_3 as solvent. Elemental analyses were obtained from the Columbia Analytical Service, Tucson, AZ, USA.

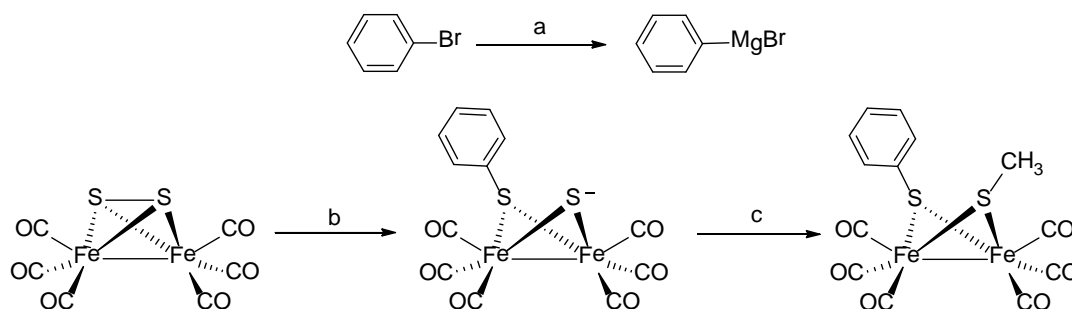
Synthesis of μ -dithiolatodiironhexacarbonyl, $[(\mu\text{-S})_2\text{Fe}_2(\text{CO})_6]$

The $[(\mu\text{-S}_2)\text{Fe}_2(\text{CO})_6]$ complex was prepared following the literature method with some modification (Seyferth, Henderson, and Song, 1982). A 2000 mL 3-neck flask, fitted with a mechanical stirrer, an Ar-inlet adapter, and septum sealing, was

flushed with Ar. $\text{Fe}(\text{CO})_5$, 20 mL (0.149 mol) was added to the flask followed by 100 mL MeOH, and 60 mL of freshly prepared 50% w/v aqueous KOH. The reaction was stirred for 15-20 min under Ar and the homogeneous solution cooled to 0 °C in an ice bath. S_8 , 26.13 g (0.102 mol) was added via a solids addition funnel and the turbid black mixture stirred for 20-30 min then 250 mL of H_2O , 500 mL of pentane, and 67.3 g (0.701 mol) of NH_4Cl were added. The ice bath was removed, and the reaction mixture was stirred at room temperature for 3 hr. The resulting reaction mixture consisted of a dark red pentane layer and a black oily aqueous phase. The remainder of the preparation was carried out without inert atmosphere precautions, the pentane layer was filtered through Celite. The aqueous phase was extracted again with 200 mL of pentane, which was also filtered through the Celite. The deep red pentane fractions were combined, dried over Na_2SO_4 , and evaporated to dryness using a rotary evaporator. The solid product was purified by silica gel flash column chromatography with pentane or hexane as eluent or by vacuum sublimation at room temperature. Yield 6.3 g (18.3 mmol), 25% based on $\text{Fe}(\text{CO})_5$. R_f : 0.71, IR (mineral oil or hexane, ν_{CO} , cm^{-1}): 2082 (m), 2042 (m), 2005 (vs) and 1990 (w).

Synthesis of $[(\mu\text{-SMe})(\mu\text{-SPh})\text{Fe}_2(\text{CO})_6]$, Me = CH_3 , Ph = C_6H_5

The synthesis of $[(\mu\text{-SMe})(\mu\text{-SPh})\text{Fe}_2(\text{CO})_6]$ followed the literature method (Seyferth, Henderson, Song, and Womack, 1985) with some modification as shown in Scheme 3.1



Scheme 3.1 Synthesis of $[(\mu\text{-SMe})(\mu\text{-SPh})\text{Fe}_2(\text{CO})_6]$. (a) THF, Mg, reflux, 3h, (b) THF, PhMgBr , $-78\text{ }^\circ\text{C}$, 30 min, (c) MeI $-78\text{ }^\circ\text{C}$ 30 min, $25\text{ }^\circ\text{C}$, 20 hr.

PhMgBr was prepared as follows: 0.14 g (5 mmol) of Mg turnings was placed in a 5 mL round bottom flask fitted with a condenser, purged with Ar for 40 min, then a solution of 0.31 mL (3 mmol) of bromobenzene in 2 mL dry THF was added via cannula. The reaction mixture was refluxed for 3 hr, cooled to room temperature, and kept under Ar atmosphere until used.

1.02 g (3 mmol) of $[(\mu\text{-S}_2)\text{Fe}_2(\text{CO})_6]$ was added to a 25 mL round bottom flask, purged with Ar for 40 min, and 5 mL of dry THF added to the flask via syringe. The mixture was stirred and cooled to $-78\text{ }^\circ\text{C}$ in a dry ice/acetone bath. A solution of freshly prepared PhMgBr was slowly added to the reaction flask dropwise over 15 min with stirring. The reaction mixture was stirred at $-78\text{ }^\circ\text{C}$ for 30 min and then 0.21 mL (3 mmol) of iodomethane was added via syringe. The reaction was stirred at $-78\text{ }^\circ\text{C}$ for 30 min and then warmed to room temperature and stirred overnight and the solvent removed by rotary evaporation. The dark red crude product was purified by silica gel chromatographic column, 2.5 x 25 cm, using hexane or pentane as eluents. Two product fractions were isolated, R_f 0.50 and 0.40. After removing solvent by rotary

evaporation to give a red oil product form with R_f 0.50 and a red solid product form with R_f 0.4.

Synthesis of $[(\mu\text{-SMe})(\mu\text{-STh})\text{Fe}_2(\text{CO})_6]$, Th = $\text{C}_4\text{H}_3\text{S}$

The $[(\mu\text{-SMe})(\mu\text{-STh})\text{Fe}_2(\text{CO})_6]$ complex was synthesized in the same manner except 2-bromothiophene was used instead of bromobenzene. A pale yellow solution of thienyl magnesium bromide (2-ThMgBr) was first prepared from the reaction of 0.30 mL (3.0 mmol) of 2-bromothiophene and 0.14 g (5.0 mmol) of magnesium turning in 2 mL dry THF under reflux condition for 3 hr. A solution of 1.02 g (3 mmol) of $[(\mu\text{-S}_2)\text{Fe}_2(\text{CO})_6]$ in 5 mL dry THF, cooled to $-78\text{ }^\circ\text{C}$ with stirring, was treated with 2-ThMgBr solution in drop wise via cannula. The mixture was stirred at $-78\text{ }^\circ\text{C}$ for 30 min then 0.21 mL (3 mmol) of iodomethane was added. The reaction was stirred at $-78\text{ }^\circ\text{C}$ for 30 min and then warmed to room temperature and stirred overnight and the solvent removed by rotary evaporation. Product fractions were isolated, R_f 0.46 and 0.32. A red oil product form with R_f 0.46 and a red solid form product with R_f 0.32 were obtained.

3.2 Characterizations

X-ray structure determination

Suitable dark red crystals of the complexes were obtained by recrystallization from saturated pentane solutions kept at $-18\text{ }^\circ\text{C}$ for several days. All X-ray crystallography data was submitted to the X-ray Diffraction Facility in the Chemistry Department and was collected by Dr. Sue A. Roberts using a Bruker-ApexII diffractometer equipped with a Mo K_α X-radiation source ($\lambda = 0.71073\text{ \AA}$). The crystal structures of $[(\mu\text{-SMe})(\mu\text{-SPh})\text{Fe}_2(\text{CO})_6]$ was solved by direct methods and the

crystal structures of $[(\mu\text{-SMe})(\mu\text{-STh})\text{Fe}_2(\text{CO})_6]$ was solved by Patterson methods and refined by full-matrix least-squares refinement on F^2 using the SHELXTL software (Sheldrick, 2008). All nonhydrogen atoms were refined anisotropically and hydrogen atoms were placed in idealized positions.

Electrochemistry

Cyclic voltammetry experiments were carried out using a potentiostat/Galvanostat model 273, EG & G Princeton Applied Research. A standard 3-electrode system was utilized including a Ag/0.01 M AgNO₃ reference electrode, a glassy-carbon working electrode (GCE) with 3 mm diameter determined area to 0.0878 cm², and a Pt wire counter electrode. The reference electrode was corrected against a 1.0 mM solution of ferrocene in acetonitrile and the potentials are reported versus Fc⁺/Fc (Gritzner and Kuta, 1984). General conditions for the cyclic voltammetry experiments included approximately 1 mM of each diiron compound in acetonitrile containing 0.1 M *n*-Bu₄NPF₆ as a supporting electrolyte, a scan rate of 0.1 V/s, ambient temperature, and 30 seconds waiting times between scans with stirring under N₂ or CO atmosphere. N₂ or CO was passed through the solution for 10 minutes before any electrochemical measurement. After bubbling through the solution, the tip of the deoxygenation tube was raised above the surface of the liquid and a flow of N₂ or CO gas continued throughout the experiment. During the course of the voltammetry, the solution remains quiescent and be oxygen free. The electrode was polished with 0.05 micron alumina in deionized water on a felt surface prior to each experiment to avoid reduced catalyst from a previous experiment to remain on the working electrode surface.

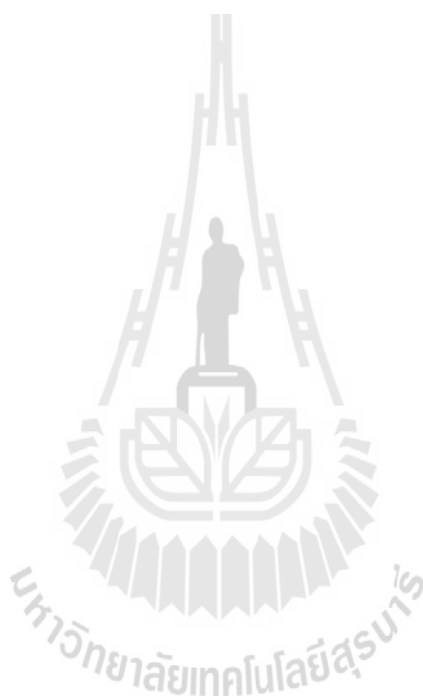
Gas-phase Ultraviolet Photoelectron Spectroscopy

Photoelectron spectra were recorded using an instrument that features a 36 cm hemispherical analyzer (McPherson) with custom-designed photon source, sample cells, detection and control electronics. Spectrum calibration was obtained with Ar, and data fitting by WinFp v22.09 program (Lichtenberger and Copenhaver, 1990). All samples were sublimed at 70-80 °C. The contour of ionization intensity were obtained at 21.2 eV (He I) and 40.8 eV (He II).

3.3 Density Functional Theory Calculations

All DFT calculations were performed using Amsterdam Density Functional (ADF) software version 2010.02 (Scientific Computing and Modelling, 2010). Typical input file for ADF calculation shown in Appendix A.1. Geometry optimizations and frequency calculations were carried out in the gas-phase using local density approximation (LDA) (Kohn and Sham, 1965; Ceperley and Alder, 1980) and the Vosko-Wilk-Nusair (VWN) functional (Vosko, Wilk, and Nusair, 1980) with the Stoll correction implemented (Stoll, Pavlidou, and Preuß, 1978). Single point energy and conductor-like screening model (COSMO) (Klamt, 1995; Klamt and Schüürmann, 1993) of solvation were calculated using generalized gradient approximation (GGA) and the Optimized Perdew-Becke exchange (OPBE) density functional (Swart, Ehlers, and Lammertsma, 2004) in a simulated acetonitrile solvated environment ($\epsilon = 37.5$). A polarization function of triple- ζ with one polarization function (TZP) and relativistic corrections zeroth-order relativistic approximation (ZORA) (Te Velde *et al.*, 2001), available in the ADF package were used in all calculations. All electronic structures with unpaired spins were calculated using an unrestricted framework. Free energy (G) values were calculated from the electronic self-consistent-field (SCF) energies. Figures of the optimized geometries were

generated with the program Molekel (Portmann, 2000) and orbital plots were created using the visualization program VMD (Humphrey, Dalke, and Schulten, 1996) with a surface cutoff value of 0.05.



CHAPTER IV

SPECTROSCOPIC, STRUCTURAL AND COMPUTATIONAL STUDIES OF

$[(\mu\text{-SR})(\mu\text{-SR}')\text{Fe}_2(\text{CO})_6]$

The hydrogenase active-site inspired complexes, $[(\mu\text{-SR})(\mu\text{-SR}')\text{Fe}_2(\text{CO})_6]$, R = CH₃ (Me), R' = C₆H₅ (Ph) or C₄H₃S (Th), were obtained from the reaction of $[(\mu\text{-S}_2)\text{Fe}_2(\text{CO})_6]$ with corresponding aromatic magnesium bromide followed by methylation in THF at low temperature. Isolated diiron products were characterized by NMR, IR spectroscopy and gas phase UV photoelectron spectroscopy, elemental analysis, and X-ray crystallography.

4.1 NMR Spectroscopy

NMR spectra were measured for isolated products collected after column chromatography. Products for some fractions were not pure, exhibiting proton chemical shifts from minor isomers. The chemical shift of the methyl protons can be used for isomer identification (Seyferth, Henderson, Song, and Womack, 1985). The synthesized complexes, $[(\mu\text{-SR})(\mu\text{-SR}')\text{Fe}_2(\text{CO})_6]$, can have different isomers depending on the orientation of R and R' substituent. Thus, the abbreviations of isomers are introduced for convenience when mentioning the isomers. The isomers of complexes are represented in form R **a** (or **e**)/R' **a** (or **e**), **a** defines the axial position and **e** defines the equatorial position. For example, Me **a**/Ph **e** indicates the isomer of $[(\mu\text{-SMe})(\mu\text{-SPh})\text{Fe}_2(\text{CO})_6]$ with Me in an axial

position and Ph in an equatorial position.

$[(\mu\text{-SMe})(\mu\text{-SPh})\text{Fe}_2(\text{CO})_6]$

The $^1\text{H-NMR}$ spectrum exhibits three singlet methyl proton resonances at $\delta = 1.72$, 2.07 , and 2.16 ppm assigned to Me **a/Ph e**, Me **e/Ph a.**, and Me **e/Ph e** isomers, respectively. At $\delta = 2.16$ ppm assigned to the *syn-endo* isomer, Me **e/Ph e**, because the singlet line occur close to one which methyl is in an equatorial site rather than one in which the methyl is in an axial site as the *syn-exo* isomer, Me **a/Ph a**, does not exist. The *syn-endo* isomer is a kinetic product and can convert to an *anti*-isomer, but the *anti*-isomer does not convert back to the *syn-endo* isomer, thus the *anti*-isomer product increases with increasing reaction time (Seyferth, Henderson, Song, and Womack, 1985; Adeleke, Chen, and Liu, 1992). In this experimental, the synthesized complexes were prepared with 20 hr reaction time lead to the *anti*-isomer is the predominant from and the *syn-endo* isomer present as an impurity and not isolated. Three isomers exist, two *anti*-isomers, Me **a/Ph e** and Me **e/Ph a**, are isolated with Me **e/Ph a** isomer as major product.

Me **a/Ph e** isomer, red oil product; 0.289 g, 22% (5:1 mixture of Me **a/Ph e**:Me **e/Ph a**); R_f (hexane) 0.50; IR (mineral oil, νCO , cm^{-1}): 2072 (m), 2035 (vs), 2001 (s) and 1996 (s); $^1\text{H-NMR}$ (CDCl_3): δ (ppm), 1.72 (s, 3H), 7.26-7.24 (m, 3H), 7.41-7.38 (m, 2H).

Me **e/Ph a** isomer, red solid product; 0.422 g, 32%; R_f (hexane) 0.40; Anal. found: C, 35.83; H; 1.89 (Calc. for $\text{C}_{13}\text{H}_8\text{Fe}_2\text{O}_6\text{S}_2$: C, 35.81; H, 1.85%); IR (mineral oil, νCO , cm^{-1}): 2072 (m), 2035 (vs), 2001 (s) and 1991 (s); $^1\text{H-NMR}$ (CDCl_3): δ (ppm), 2.07 (s, 3H), 7.20-7.14 (m, 2H), 7.27-7.21 (m, 3H); ^{13}C NMR (CDCl_3): δ (ppm) 22.30, 127.92, 128.29, 128.86, 134.18, 208.82. mp 66-65 °C.

$[(\mu\text{-SMe})(\mu\text{-STh})\text{Fe}_2(\text{CO})_6]$

Three singlet methyl proton resonances at 1.69, 2.12, and 2.15 ppm are observed and can be assigned to Me **a**/Th **e**, Me **e**/Th **a**, and Me **e**/Th **e** isomer, respectively. Two *anti*-isomeric products, Me **a**/Th **e**, Me **e**/Th **a**, were isolated with Me **e**/Th **a** isomer as major product.

Me **a**/Th **e** isomer, red oil; 0.264 g, 20% (6:1 mixture of Me **a**/Th **e**:Me **e**/Th **a**); R_f (hexane) 0.46; IR (hexane, ν_{CO} , cm^{-1}): 2076 (m), 2040 (vs), 2005 (s), and 2000 (s); $^1\text{H-NMR}$ (CDCl_3): δ (ppm), 1.69 (s, 3H), 6.84 (t, 1H), 7.09 (d, 1H), 7.24 (d, 1H).

Me **e**/Th **a** isomer, red solid; 0.399 g, 30%; R_f (hexane) 0.32; Anal. found: C, 30.00; H, 1.10; (Calc. for $\text{C}_{11}\text{H}_6\text{Fe}_2\text{O}_6\text{S}_3$: C, 29.89; H, 1.37%); IR (mineral oil, ν_{CO} , cm^{-1}), 2074 (m), 2039 (vs), 2004 (s), and 1995 (s); $^1\text{H-NMR}$ (CDCl_3): δ (ppm), 2.12 (s, 3H), 6.86 (dd, $J = 3.6, 5.2$ Hz, 1H), 6.96 (dd, $J = 1.2, 3.6$ Hz, 1H), 7.20 (dd, $J = 1.2, 5.2$ Hz, 1H); $^{13}\text{C NMR}$ (CDCl_3): δ (ppm) 21.86, 127.56, 128.61, 134.42, 208.25. mp 88-90 °C.

Structural diagrams of four isolated products are shown in Figure 4.1. The isomers with the methyl group in the axial position and the aromatic ring in the equatorial position (Figures 4.1a and 4.1c) for both compounds are not stable and slowly decompose at room temperature over several days. In this work, main characterizations for both formula complexes were carried out on more thermodynamically stable forms with the methyl groups in the equatorial position and the aromatic rings in the axial position as shown in Figures 4.1b and 4.1d which were designated as complex **1** for Me **e**/Ph **a** and complex **2** for Me **e**/Th **a**.

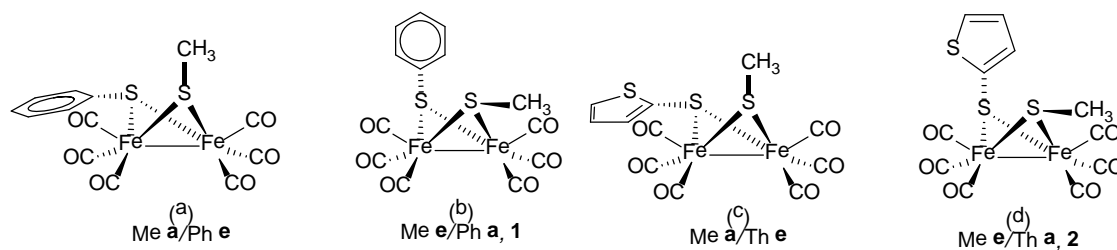


Figure 4.1 Structural diagrams of isolated products of $[(\mu\text{-SMe})(\mu\text{-SPh})\text{Fe}_2(\text{CO})_6]$ and $[(\mu\text{-SMe})(\mu\text{-STh})\text{Fe}_2(\text{CO})_6]$.

Attempts to study the equilibration between isomers by variable temperature NMR in 1,4-dioxane- d_8 solution were not definitive. It was not possible to observe any exchange of methyl groups between the axial and equatorial sites. When temperature was increased to 85 °C, some precipitate due to decomposition was observed, shown in Figure 4.2. This agrees with a reported study on $[(\mu\text{-SMe})_2\text{Fe}_2(\text{CO})_6]$ and the observation that the methyl thiolate-bridged compounds show no evidence of axial-equatorial R group exchange (Adams, Cotton, Cullen, Hunter, and Mihichuk, 1975).

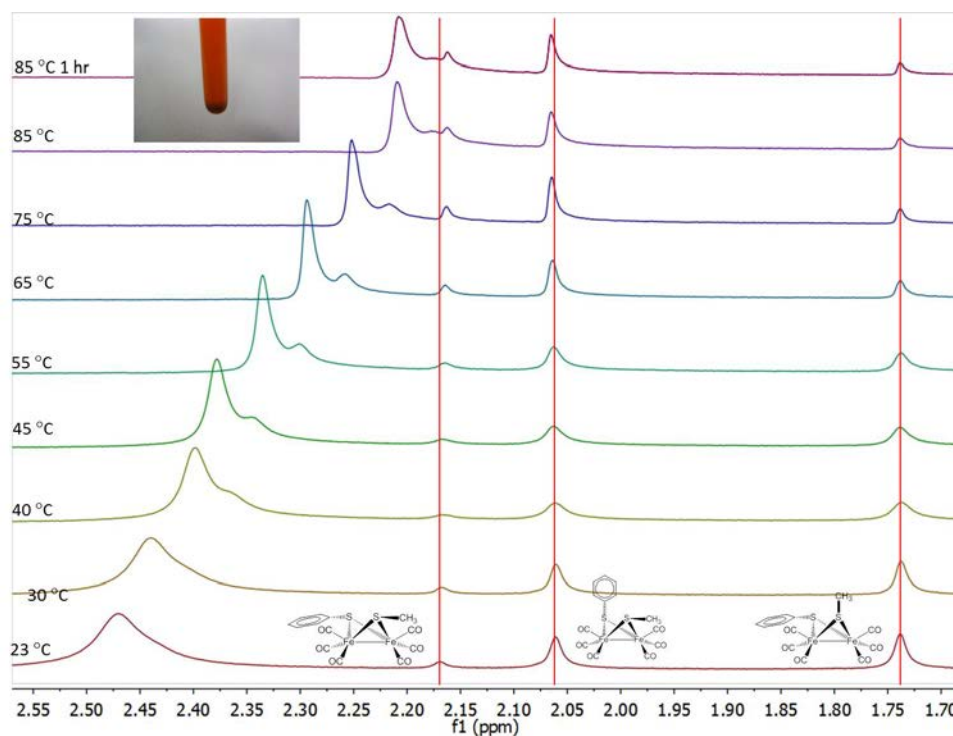


Figure 4.2 Variable temperature ^1H -NMR of mixed isomer of $[(\mu\text{-SMe})(\mu\text{-SPh})\text{Fe}_2(\text{CO})_6]$ in dioxane- d_8 solution. Inserted structural diagrams label ^1H chemical shift of methyl group correspond to difference isomer and inserted picture on top left is NMR tube containing sample after VT NMR.

4.2 X-ray Structure Determination

The crystallographic data for **1** and **2** are listed in Table 4.1 and the crystal morphology of the complexes are shown in Figure 4.3 The crystal of $[(\mu\text{-SMe})(\mu\text{-SPh})\text{Fe}_2(\text{CO})_6]$ crystallized from the mixed isomer solution of two *anti*-isomers, Me **a**/Ph **e** and Me **e**/Ph **a**, while the crystal of $[(\mu\text{-SMe})(\mu\text{-STh})\text{Fe}_2(\text{CO})_6]$ crystallized from solution of pure *anti*-isomer, Me **e**/Th **a** isomer.

Table 4.1 Summary of data collection and structure refinement parameters for complexes $[(\mu\text{-SMe})(\mu\text{-SPh})\text{Fe}_2(\text{CO})_6]$ and $[(\mu\text{-SMe})(\mu\text{-STh})\text{Fe}_2(\text{CO})_6]$.

Identification code	$[(\mu\text{-SMe})(\mu\text{-SPh})\text{Fe}_2(\text{CO})_6]$	$[(\mu\text{-SMe})(\mu\text{-STh})\text{Fe}_2(\text{CO})_6]$
Formula	$\text{C}_{13}\text{H}_8\text{Fe}_2\text{O}_6\text{S}_2$	$\text{C}_{11}\text{H}_6\text{Fe}_2\text{O}_6\text{S}_3$
<i>Mr</i>	436.01	442.04
Crystal system	Triclinic	Triclinic
Crystal color/habit	Orange/ square plate	Dark red/ block
Crystal size (mm)	0.50 x 0.30 x 0.05	0.20 x 0.20 x 0.10
Space group	$\text{P}\bar{1}$ (No. 2)	$\text{P}\bar{1}$ (No. 2)
<i>a</i> (Å)	13.5031(15)	7.5900(6)
<i>b</i> (Å)	15.1769(16)	8.9694(8)
<i>c</i> (Å)	16.8412(18)	12.7976(11)
α (°)	102.263(5)	77.388(2)
β (°)	97.249(5)	80.522(2)
γ (°)	90.311(5)	67.892(2)
<i>V</i> (Å ³)	3343.8(6)	784.41(12)
<i>Z</i>	8	2
<i>D</i> _{calc} (Mg m ⁻³)	1.732	1.872
Temperature (K)	200±2	100±2
μ (Mo <i>K</i> α) (mm ⁻¹)	2.008	2.270
<i>F</i> (000)	1744	440
θ range (°)	1.52 to 26.41	1.64 to 28.32
Data completeness (%)	99.4	99.7
Limiting indices	$-16 \leq h \leq 16$ $-18 \leq k \leq 18$ $-21 \leq l \leq 20$	$-10 \leq h \leq 5$ $-11 \leq k \leq 11$ $-17 \leq l \leq 15$
Reflection collected	66749	19954
<i>R</i> _{int}	0.0550	0.0321
Data/restraints/ parameters	13637/0/833	3893/0/223
<i>R</i> ₁ , <i>wR</i> ₂ [all data]	0.0523, 0.0716	0.0262, 0.0665
<i>R</i> ₁ , <i>wR</i> ₂ [<i>I</i> > 2σ(<i>I</i>)]	0.0311, 0.0631	0.0236, 0.0647
Goodness of fit on <i>F</i> ²	1.019	1.066
$\Delta\rho_{\text{min}}$, $\Delta\rho_{\text{max}}$ (e Å ⁻³)	0.411, -0.315	0.728, -0.490



Figure 4.3 Crystal morphology of $[(\mu\text{-SMe})(\mu\text{-SPh})\text{Fe}_2(\text{CO})_6]$ (a) and $[(\mu\text{-SMe})(\mu\text{-STh})\text{Fe}_2(\text{CO})_6]$ (b).

$[(\mu\text{-SMe})(\mu\text{-SPh})\text{Fe}_2(\text{CO})_6]$

The synthesis of $[(\mu\text{-SMe})(\mu\text{-SPh})\text{Fe}_2(\text{CO})_6]$ has been reported previously (Seyferth, Henderson, and Song, 1982), but the crystal structure has not been reported. Complex $[(\mu\text{-SMe})(\mu\text{-SPh})\text{Fe}_2(\text{CO})_6]$ exists as two conformational isomers in the crystalline state. The mixed isomers crystallize in the triclinic space group $P\bar{1}$ with four crystallographically independent dimer molecules in the crystallographic asymmetric unit ($Z' = 4$) showing two different *anti*-stereoisomers in 50:50 ratio as shown in Figure 4.4. Four independent molecules are *anti*-isomeric form, two molecules labeled as **A** and **B** possess Me e/Ph a isomer while two other molecules labeled as **C** and **D** contain Me a/Ph e isomer. Independent molecules have been separated for clarity show in Figure 4.5. Independent molecule **A**, **B**, **C**, and **D** contains two $\text{Fe}(\text{CO})_3$ units which are bridged by two different thiolate ligands, $-\text{SMe}$ and $-\text{SPh}$, resulting an $[\text{2Fe}_2\text{S}]$ core. The addition of three CO ligands on each Fe atoms provide distort octahedral geometries around each Fe atoms (Fe–Fe–Caxial angles $148.8\text{--}150.9^\circ$). Bond length of Fe–Fe of **A**, **B**, **C**, and **D** is $2.5116(6)$,

2.5111(6), 2.5135(6) and 2.5173(6) Å, respectively, fall in the normal Fe–Fe bond length (2.49–2.57 Å) (Yu *et al.*, 2008).

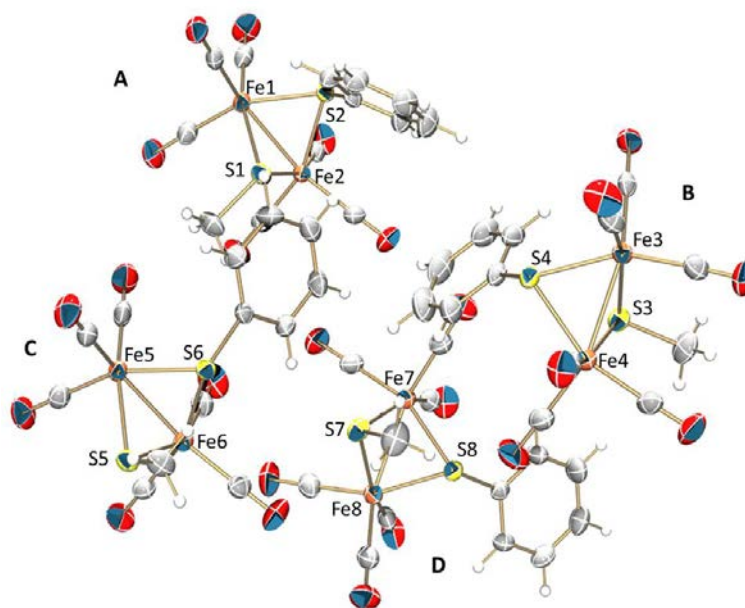


Figure 4.4 ORTEP diagram of the asymmetric unit of $[(\mu\text{-SMe})(\mu\text{-SPh})\text{Fe}_2(\text{CO})_6]$ with Fe and S atoms label. Anisotropic displacement ellipsoids at the 50% probability level for nonhydrogen atoms and H atoms are shown as small spheres of arbitrary radius.

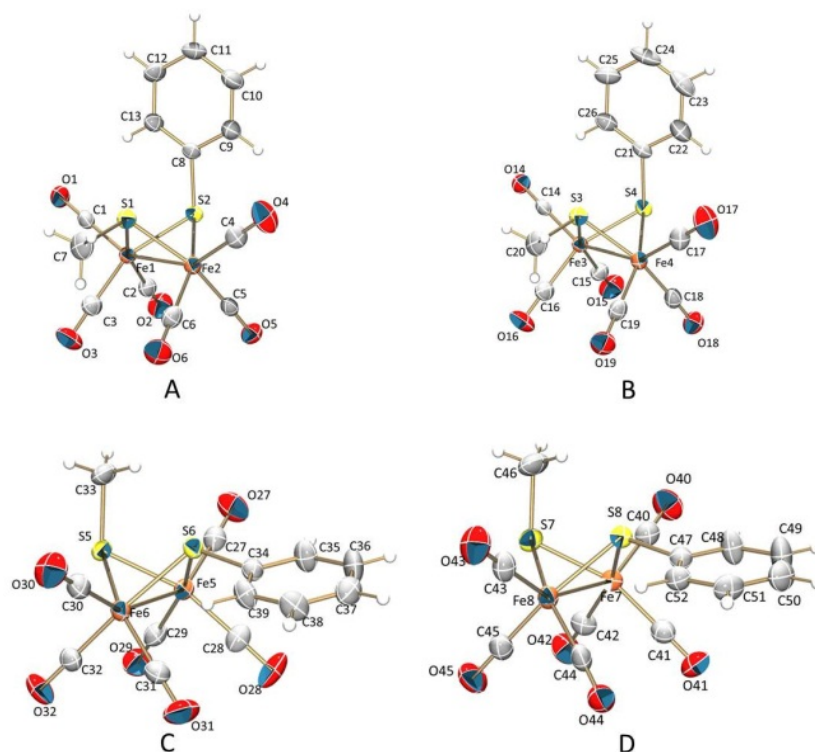


Figure 4.5 ORTEP diagrams of four crystallographically independent molecules, **A**, **B**, **C**, and **D**, of $[(\mu\text{-SMe})(\mu\text{-SPh})\text{Fe}_2(\text{CO})_6]$. Displacement ellipsoids are at the 50% probability level for nonhydrogen atoms. H atoms are shown as small spheres of arbitrary radius.

Each pair of isomeric molecules has a very similar conformation, bond lengths and angles. Performing a least-squares overlay of each pair of isomeric molecules on the two iron center as shown in Figure 4.6 showing excellent overlay between **A** and **B** with rmsd is 0.0003 \AA and good overlaying of **C** with **D** with rmsd is 0.0019 \AA .

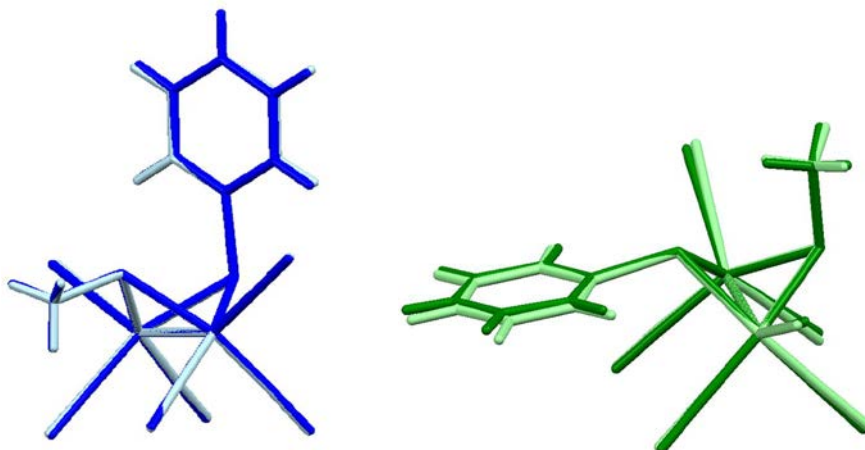


Figure 4.6 Least-squares overlays of each pair of isomeric molecules. Left: overlay molecule **A** with **B** (**A** = blue, **B** = light blue, rms deviation = 0.00026 Å); Right: overlay molecule **C** with **D** (right, **C** = green, **D** = light green, rms deviation = 0.00188 Å). The two iron centers were used as a pair for the overlay.

Comparison of structural parameters of between the DFT optimized structures and the crystal structures are provided in Appendix B (Table B1-2). Most importantly bond distances agree within 0.03 Å between DFT and crystal structures. Good agreements are observed on diiron cores, as shown in Figure 4.7 but the orientations of aromatic rings are quite different due to the effect of supramolecular interactions or packing of molecules in the crystals which computational methods cannot provide.

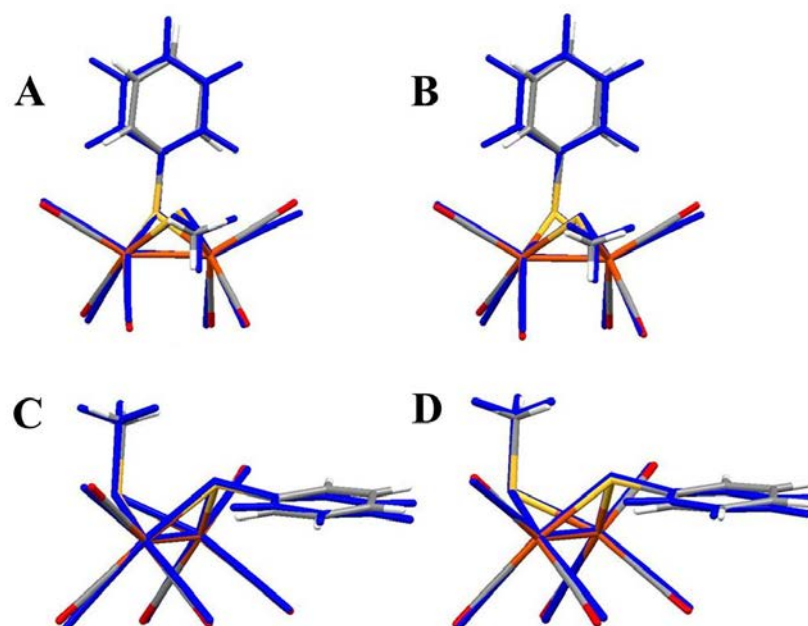


Figure 4.7 Overlay crystallographically independent molecule **A**, **B**, **C**, and **D** of $[(\mu\text{-SMe})(\mu\text{-SPh})\text{Fe}_2(\text{CO})_6]$ with DFT structures. rms deviations calculated to 0.00125, 0.00151, 0.00044, and 0.00231 Å for **A**, **B**, **C**, and **D** overlying, respectively. Atoms in crystallographically structures shown in VMD element color and in DFT structures label in blue.

The crystals crystallized with $Z = 8$ ($Z' = 4$). The Cambridge Structural Database structures in space group $P\bar{1}$ comprise 23.7% of the current total (145662 out of 615241 structures as of the May 2012 update (Allen, 2002). Of all reported $P\bar{1}$ structures, only 0.5 % show $Z' = 4$ (755 of 145662 structures). The subject of multiple molecules in the asymmetric unit is one of much recent interest for crystallography study. Different ideas have been put forward to rationalize this phenomenon, i) frustration packing caused by competing strong intermolecular interactions, (Anderson, Goeta, and Steed, 2008; Althoff *et al.*, 2006) ii) conformational flexibility

(Lloyd *et al.*, 2007) and iii) a kinetic product of crystallization or “crystal on the way” or incomplete crystallization used to describe some high $Z' > 1$ structures (Desiraju, 2006).

$[(\mu\text{-SMe})(\mu\text{-STh})\text{Fe}_2(\text{CO})_6]$

The X-ray single crystal structure analyses at 100 K reveals that compound $[(\mu\text{-SMe})(\mu\text{-STh})\text{Fe}_2(\text{CO})_6]$ crystallizes in the triclinic system with space group $P\bar{1}$. Only one conformation was found. The asymmetric unit consists of $[(\mu\text{-SMe})(\mu\text{-STh})\text{Fe}_2(\text{CO})_6]$ molecule in Me e/Th a isomeric form similar to isomers **A** and **B** of $[(\mu\text{-SMe})(\mu\text{-STh})\text{Fe}_2(\text{CO})_6]$. The Fe–Fe bond is 2.5215(3) Å which is clearly in bonding distance (Yu *et al.*, 2008). Each Fe atom exhibits distorted octahedral geometries with Fe–Fe–Caxial 150.5–151.5°. Overlay of the crystallographically structure of $[(\mu\text{-SMe})(\mu\text{-STh})\text{Fe}_2(\text{CO})_6]$ with DFT structure rms deviation calculated to 0.00521 Å. The molecular structure of **2** and overlay with the DFT structure is shown in Figure 4.8.

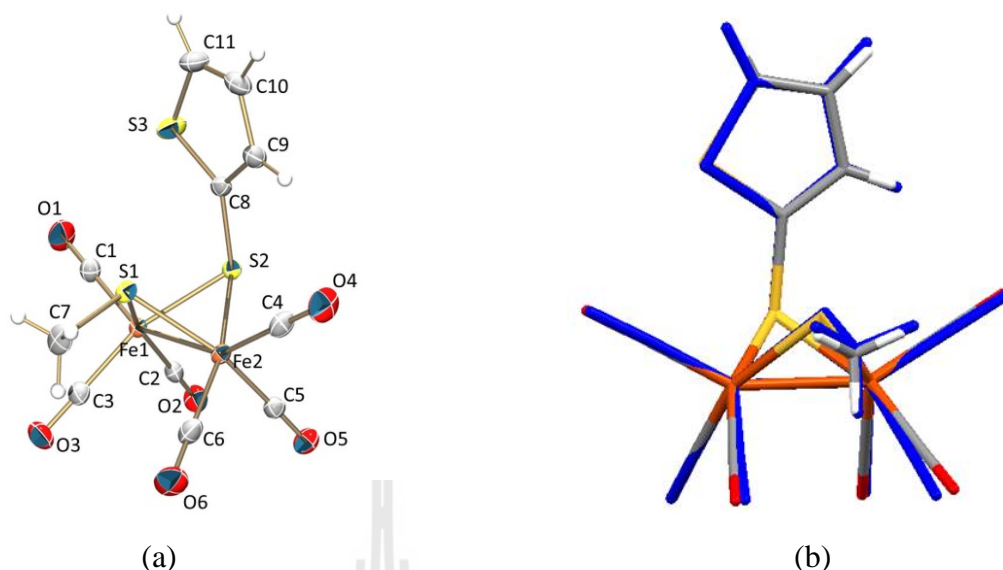


Figure 4.8 ORTEP diagram of molecular structure of **2** (a) and its overlay with DFT structure (b). Displacement ellipsoids of ORTEP diagram are at the 50% probability level for nonhydrogen atoms and H atoms are shown as small spheres of arbitrary radius. In overlay model, crystallographic structure of **2** shows in VMD colors and DFT structure show in dark blue.

The substituent groups on [2Fe2S] cores have an effect on Fe–Fe bond lengths. The Fe–Fe bond length in **2** of 2.5215(3) Å, is longer than that of the phenyl analogue, **A** (2.5116(6) Å) and **B** (2.5111(6) Å) molecules. The elongation of the Fe–Fe bond lengths in **2** could be due to the decrease in electron richness at the iron centers when the aromatic group is changed from phenyl to the thienyl group. The longer Fe–Fe distances in the neutral molecules and the shift in the carbonyl stretching are important factors to understand the electronic structure of molecules. The computations agree well with these observations.

4.3 Infrared Spectroscopy

IR spectroscopy is widely applied to study transition-metal carbonyl complexes due to the strong infrared absorption of carbonyl ligand providing some basic information about the electronic structure (Cotton, and Troup, 1974; Herrmann, 1981). The stretching frequencies of the carbonyl bands in the IR spectrum depend mainly on the bonding mode of the CO and the electron richness on the metals. The number of the carbonyl bands relates to number of CO ligands present and the symmetry of the metal complexes.

IR spectra of the CO stretching region have become an important information to the understanding of electron distributions in the diiron centers of [FeFe]-hydrogenase mimics (Schwartz *et al.*, 2008). The IR spectra on CO stretching region of **1** and **2** are shown in Figure 4.9. The CO stretching exhibits the same patterns, four strong absorption bands, because of the similarity of their conformation. The CO stretching of **1** shows slight red shifts compared to that of **2** because the phenyl group on **1** is a better electron donating ligand resulting in more metal to CO backbonding, weakening the CO bonds.

DFT calculation the total charge on the phenyl ring on **1** to be 0.099 and the total charge on the thienyl ring on **2** to 0.059 which is suggest that thienyl is more electron withdrawing ability than phenyl ring. Thus, the diiron center of **2** is less electron density supporting the blue shift in IR spectrum. This observation is good agree with the literature showing blue shift in carbonyl stretching region with substitute [2Fe2S] with electron withdrawing ligands (Schwartz, *et al.*, 2008; Schwartz, Singh, Eriksson, Lomoth, and Ott, 2008) .

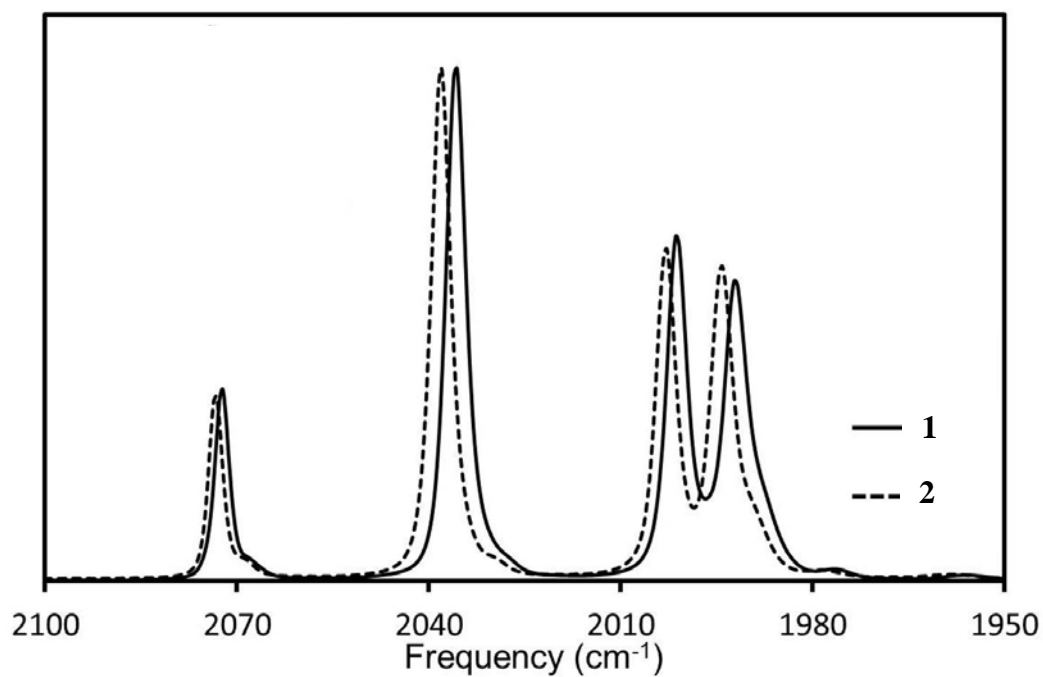


Figure 4.9 IR spectra in CO stretching region of **1** and **2**.

DFT calculation on the IR spectra in CO stretching frequencies show good agreement in both relative absorption intensities and frequencies (less than 0.5%) between the DFT calculated and experimental IR as shown in Figure 4.10.

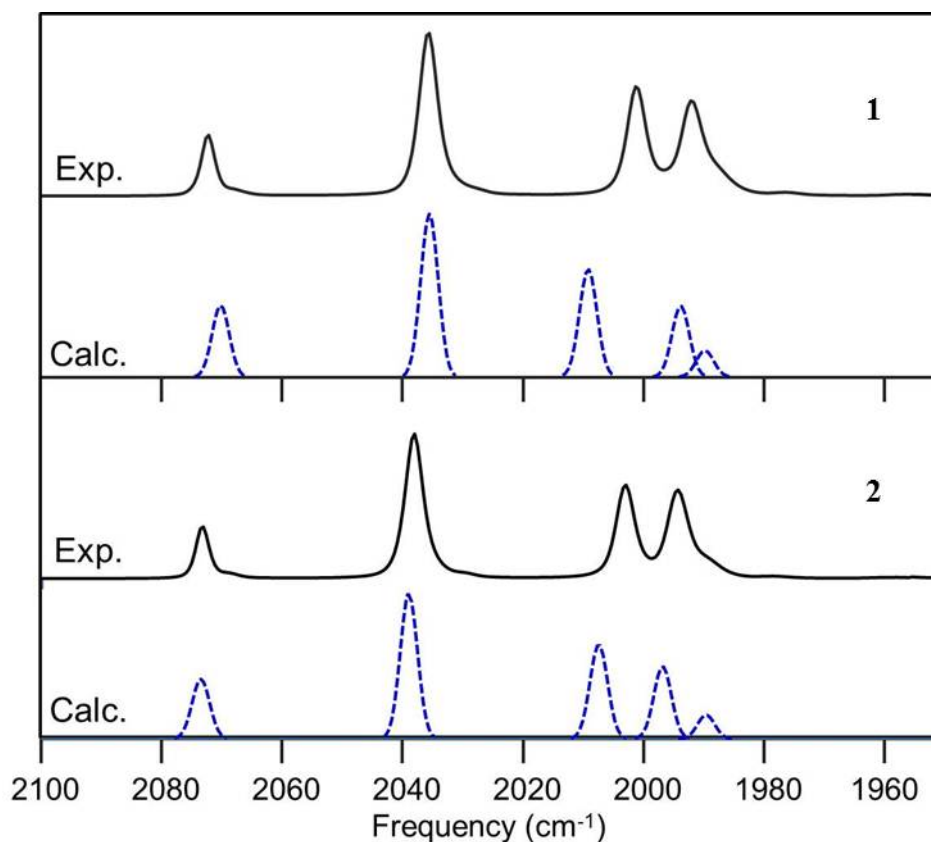


Figure 4.10 Comparison of the experimental IR spectra (in mineral oil) in the CO stretching region with DFT calculated IR spectra.

4.4 Gas-phase UV Photoelectron Spectroscopy

Gas-phase UV photoelectron spectra were collected for **1** and **2**. The ionization bands of the two complexes are similar and show characteristics of [2Fe2S] complexes (Chen *et al.*, 2010; Felton *et al.*, 2007). The first broad ionization bands appear around 7.2 eV and extend to roughly 9 eV containing mainly the iron-based *d*-electron ionizations. Ionizations starting just beyond 9 eV and continuing to higher energy are associated with ionizations of the thiolate ligands. The sulfur character that gives rise to these ionizations is shown by the considerable decrease in ionization intensity relative to the iron *d*-based region when the He II spectrum is compared to the He I spectrum as shown in Figure 4.11.

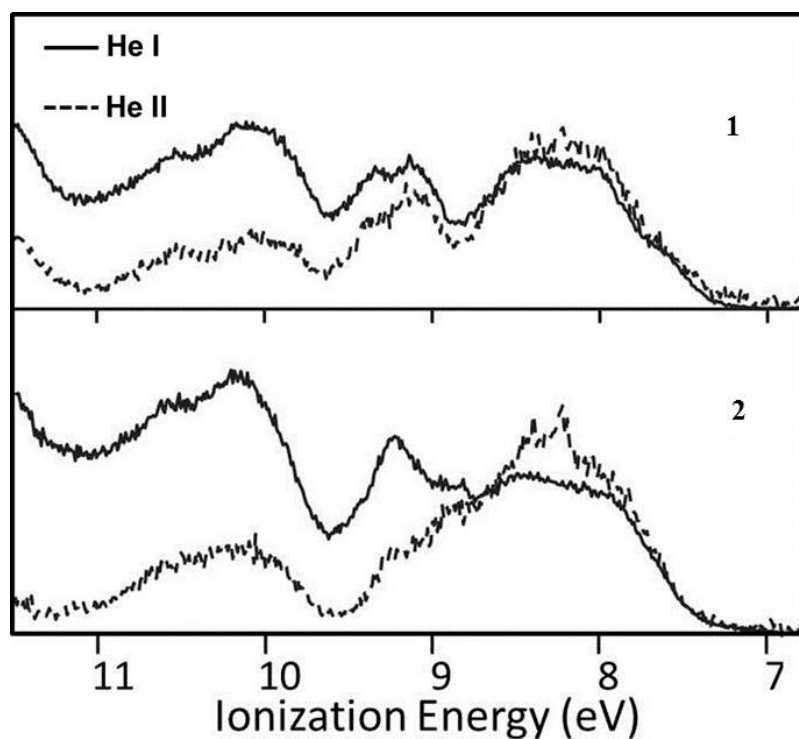


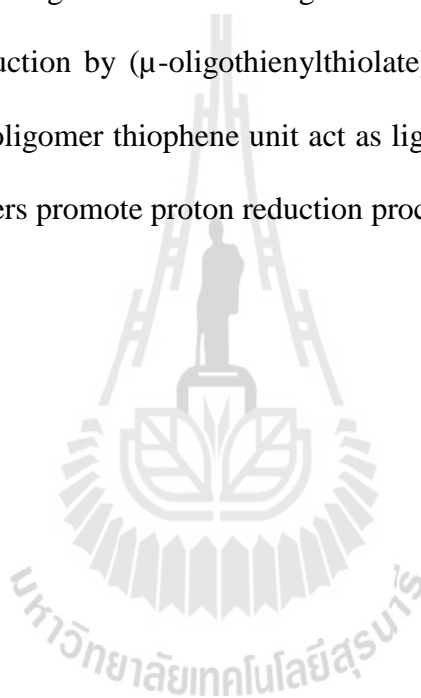
Figure 4.11 He I and He II photoelectron spectra of **1** and **2**.

Plots of DFT calculated LUMO and HOMOs of **1** and **2** are shown in Figures 4.12 and 4.13. The first broad ionization band starting from around 7.5 to 9.0 eV correspond to ionization of HOMO to HOMO-8 as shown in Figure 4.12 for **1** and 4.13 for **2** mainly composed of ionizations from the two Fe centers for **1** while complex **2** exhibits more ligand character as shown in more intense in He II spectrum. The second ionization band starting from 9.0 to 11.0 eV was found to contain substantially more S character related to ionization of HOMO-9 to HOMO-13 which is in agreement with the comparison of the He I and He II photoelectron spectra.

Photoelectron spectra suggest the first HOMO of **1** and **2** are different. Complex **1** exhibit Fe character while **2** show more ligand character consistent with DFT calculations showing **1** contains metal based HOMO while **2** contains thiophene

π orbital based HOMO which is more stable and shows slightly higher onset ionization.

Crystal colors support the HOMO difference between **1** and **2**. DFT calculation shows LUMO of both compounds are similar containing anti bonding metal-based orbitals. Crystals of **1** show orange color due to *d-d* transition while crystals of **2** show deep red color due to ligand to metal charge transfer which color is more intense. This investigation should be a good result to support the possibility of light driving H₂ production by (μ -oligothienylthiolate)[Fe(CO)₃]₂ for photo-assisted H₂ production which oligomer thiophene unit act as light absorption unit and transfer electron to diiron centers promote proton reduction process.



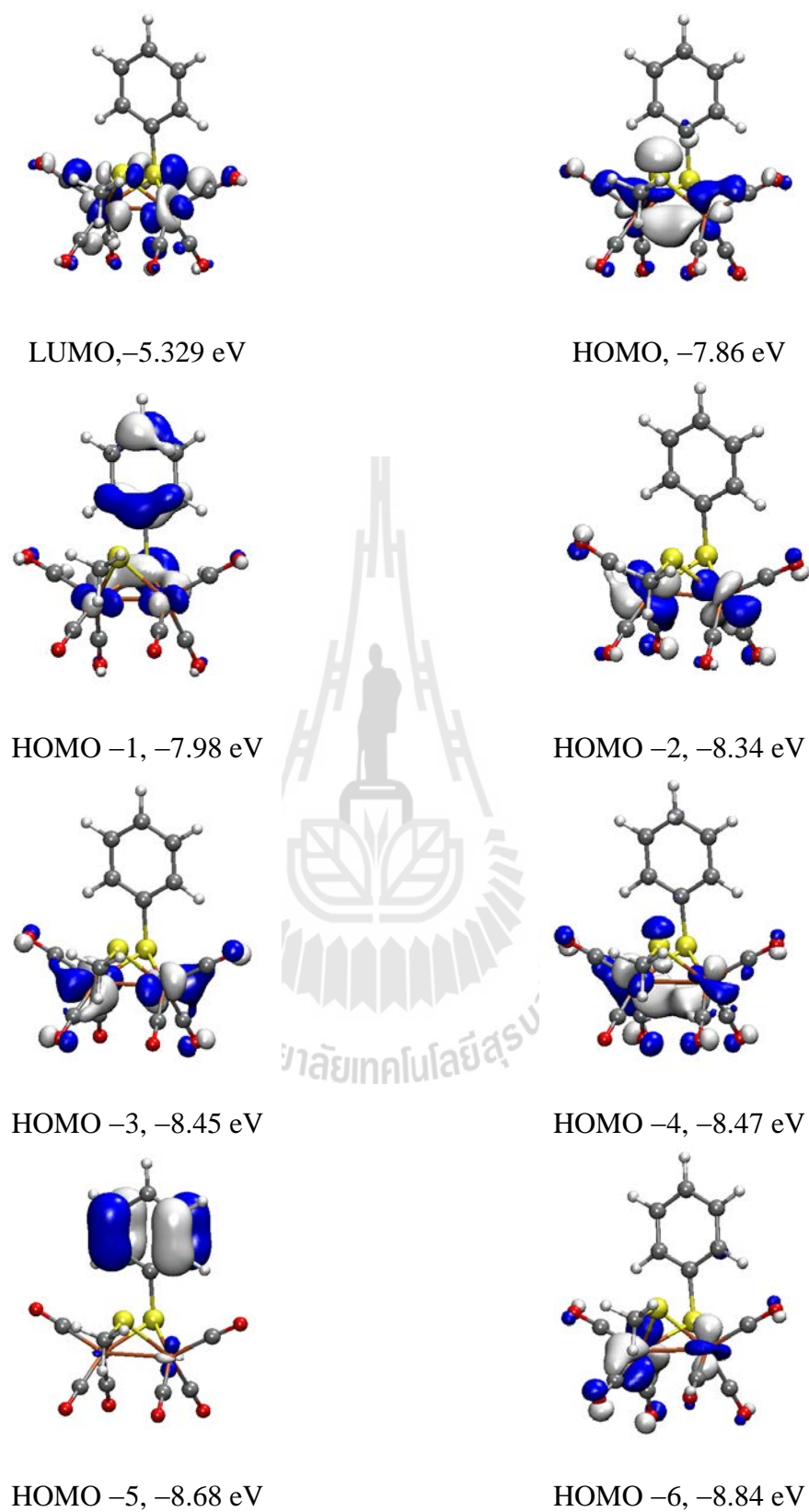


Figure 4.12 Plots of LUMO and HOMOs of **1**.

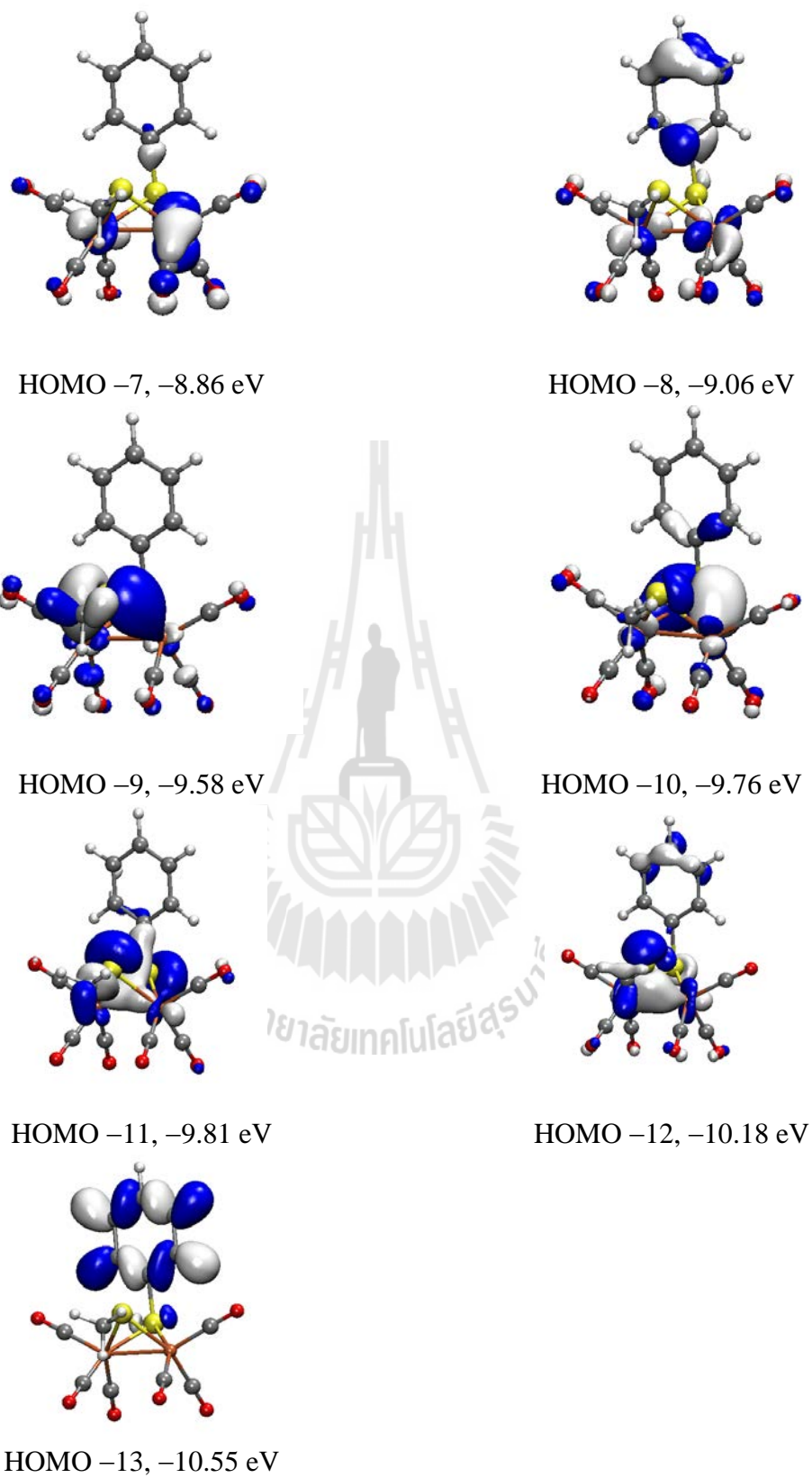


Figure 4.12 (Continued).

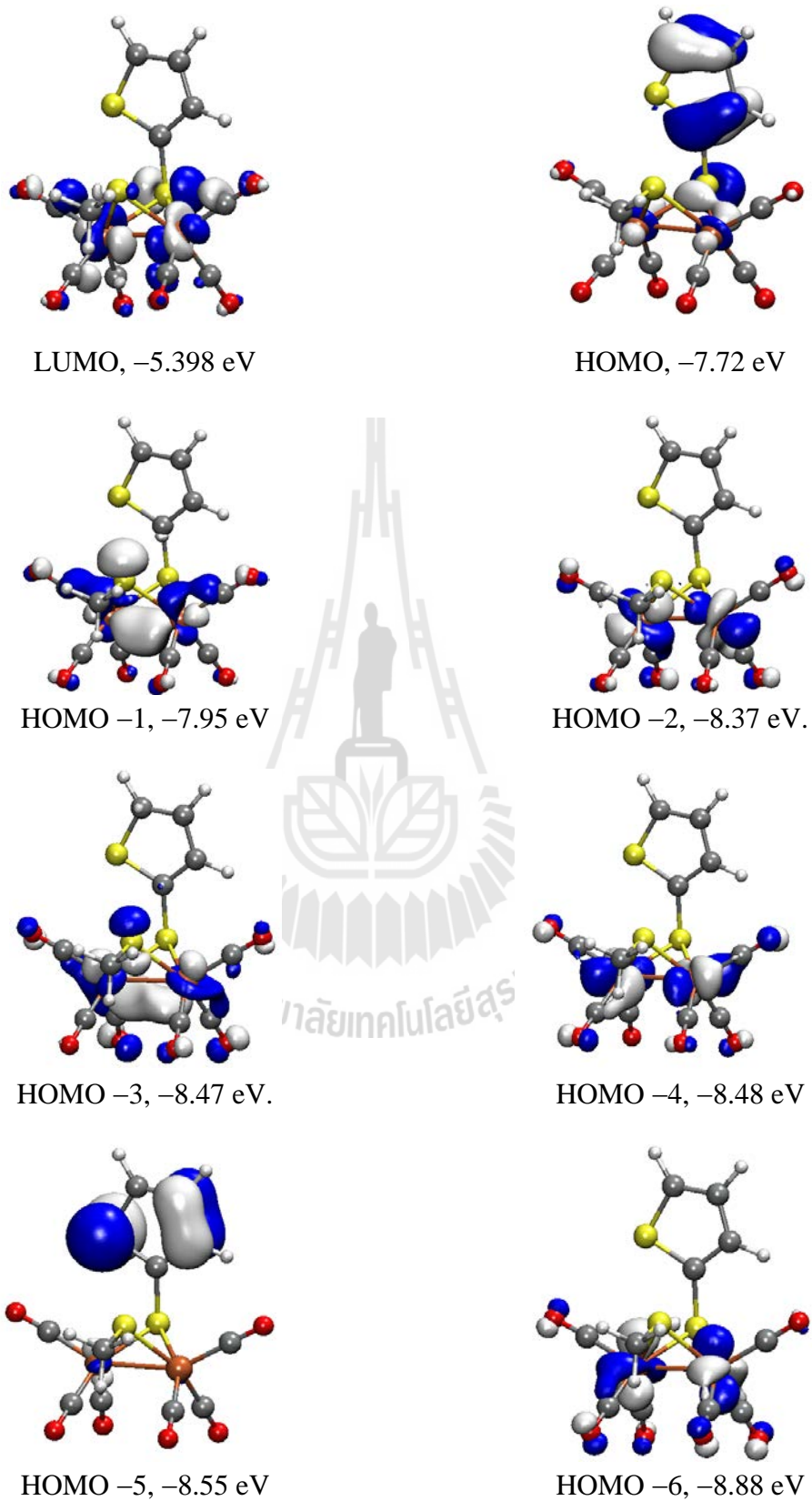


Figure 4.13 Plots of LUMO and HOMOs of **2**.

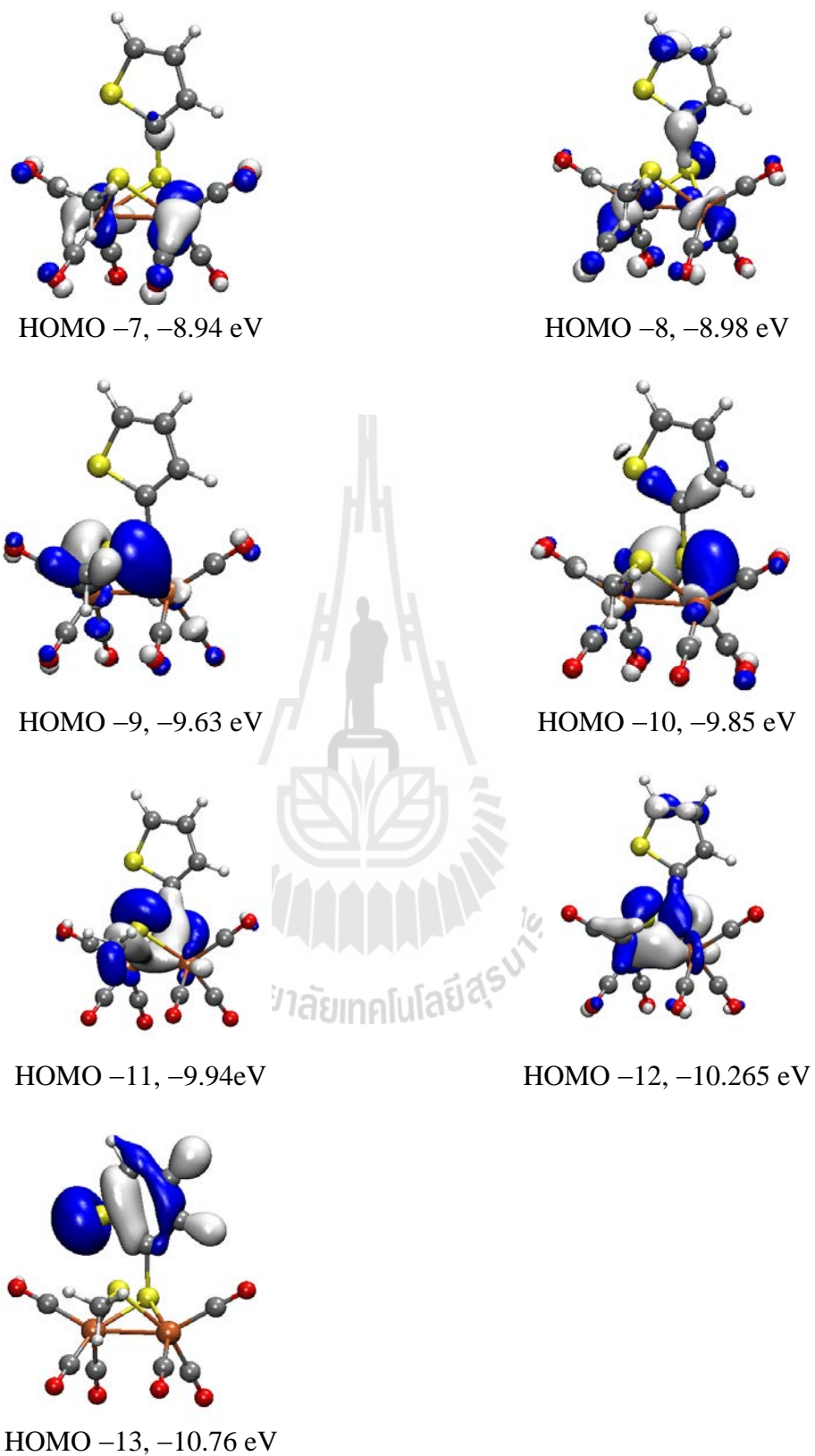


Figure 4.13 (Continued).

CHAPTER V

ELECTROCHEMICAL AND COMPUTATIONAL STUDIES

OF $[(\mu\text{-SR})(\mu\text{-SR}')\text{Fe}_2(\text{CO})_6]$

Cyclic voltammetry is an electrochemical technique. It is a useful method to investigate the chemical stability, the oxidation and/or reduction of molecules, and aid understanding catalytic behavior of compounds in solution.

In this study, two hydrogenase active-site mimics **1** and **2** as shown in Figure 5.1 were studied for electrocatalyzed proton reduction of acetic acid to produce molecular hydrogen.

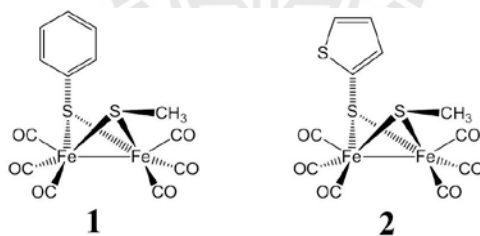


Figure 5.1 Structural diagrams of $[(\mu\text{-SMe})(\mu\text{-SPh})\text{Fe}_2(\text{CO})_6]$ (**1**) and $[(\mu\text{-SMe})(\mu\text{-STh})\text{Fe}_2(\text{CO})_6]$ (**2**)

5.1 Electrochemical Investigation

Cyclic voltammograms of oxidation and reduction scans of **1** and **2**, shown in Figure 5.2, were recorded in anhydrous CH_3CN with 0.1 M $n\text{-Bu}_4\text{NPF}_6$ as supporting electrolyte and GC electrode at a scan rate 0.100 V/s. Complexes **1** and **2** display irreversible reduction and oxidation processes. The reduction of **1** and **2** occurs at a

peak potential of -1.53 and -1.46 V vs. Fc^+/Fc , respectively. The first oxidation occurs at 0.67 V for **1** and 0.61 V for **2**. A 70 mV positive shift in reduction potential is observed from **1** to **2** because the thienyl ligand of **2** is a better electron-withdrawing substituent than the phenyl ligand of **1**, so the electron density on the metal centers of **2** is less than that of **1**. The oxidation scan shows the oxidation peak shifted in the opposite direction, a 60 mV negative shift, which is actually opposite of what one would expect based on the electron withdrawing ability of the thienyl ligand. Both the reduction and the oxidation should shift to positive direction if LUMO and HOMO are metal-based orbitals. This opposite shift of oxidation and reduction suggest that HOMO of **2** is the thiophene pi orbital instead. This observation taken together with the PES result strengthens the argument that the HOMOs of the two molecules are different.

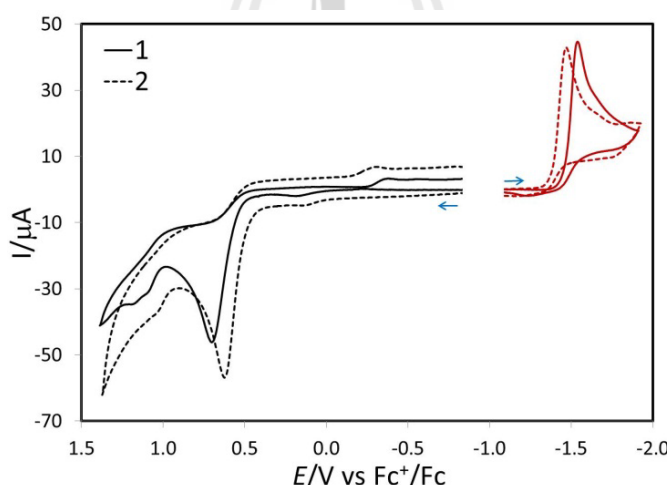


Figure 5.2 Reduction and oxidation scans of **1** and **2** in CH_3CN under N_2 atmosphere.

Arrows indicate the direction of scans.

Comparison of the peak currents of **1** and **2** (~ 45 μA) to known processes, $1 e^-$ reduction of PDT (35 μA) and $2 e^-$ reduction of BDT (60 μA) (Felton *et al.*, 2007), suggests that the reduction process of **1** and **2** is between a $1 e^-$ and a $2 e^-$ reduction process at 0.100 V/s. The initial reaction is suggested to be a $1 e^-$ process, but the product

of that step undergoes a structural change producing a form that is more easily reduced than the neutral starting molecule. This feature is called potential inversion and the potential of the intermediate is called an inversion potential which is the average potential of the first and second electron reduction. A $2 e^-$ reduction with potential inversion has been proposed for BDT and Fp_2 (Felton *et al.*, 2007; Felton *et al.*, 2008).

The negative scan through the first reduction and then continues the return scan in positive direction, a new oxidation peak at about -0.5 V vs. Fc^+/Fc is observed as shown in Figure 5.3, corresponding to the oxidation of products formed upon reduction. This oxidation peak is similar found in reported complexes; $[(\mu-SPh)_2Fe_2(CO)_6]$ (Si, Hu, and Chen, 2008), $[(\mu-S-2-RCONHC_6H_4)_2Fe_2(CO)_6]$ ($R = CH_3, CF_3, C_6H_5, 4-FC_6H_4$), $[(\mu-RS)_2Fe_2(CO)_6]$ ($R = Me, Et$) (Darchen, Mousser, and Patin, 1988) and PDT (Song *et al.*, 2006) and suggests this peak corresponds to an unidentified electroactive fragment.

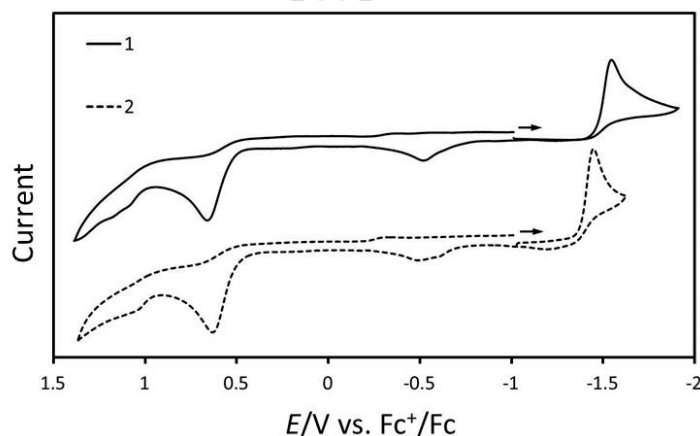


Figure 5.3 Cyclic voltammograms of **1** and **2**.

The oxidation peak at -0.5 V plays an important role in the recovery of the current in return scans. In return scans, a positive scan through oxidation of reduced species of about -0.5 V, then scan back toward negative potential, and most of the current can be recovered even at a faster scan rate (0.2 V/s) in Figure 5.4. Performing back scan at -0.2 V some current can be recovered as shown in Figure 5.5a while

diffusion will take at least 30 s to recover all the current as shown in figure 5.5b. This suggests that the reduced species may undergo a chemical transformation to a species that stabilizes the reduced species such that it is more difficult to oxidize on the return scan. Scan rate dependence on current recovery provides some information to support this investigation. If a slow scan rate is used (0.05 and 0.1 V/s), reduced species have enough time to diffuse away from the electrode surface then may react with other reactive species in the solution, degrade, or rearrange to a stable geometry, which could lead to observation of other oxidation events or inversion potential may occur and most of current can be recovered. While faster scan rates is used (0.2 V/s), 11 s total scan time, most of current still can be recovered while diffusion process takes at least 30 s equilibration time to recover most of the current.

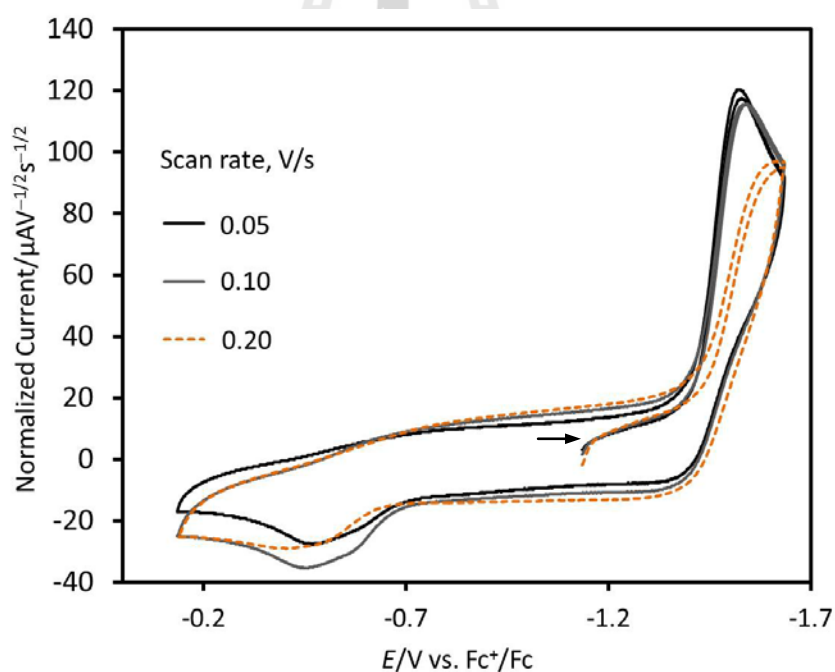


Figure 5.4 Cathodic current recoveries in return scan at varied scan rates of 2. Arrows indicate the direction of scans.

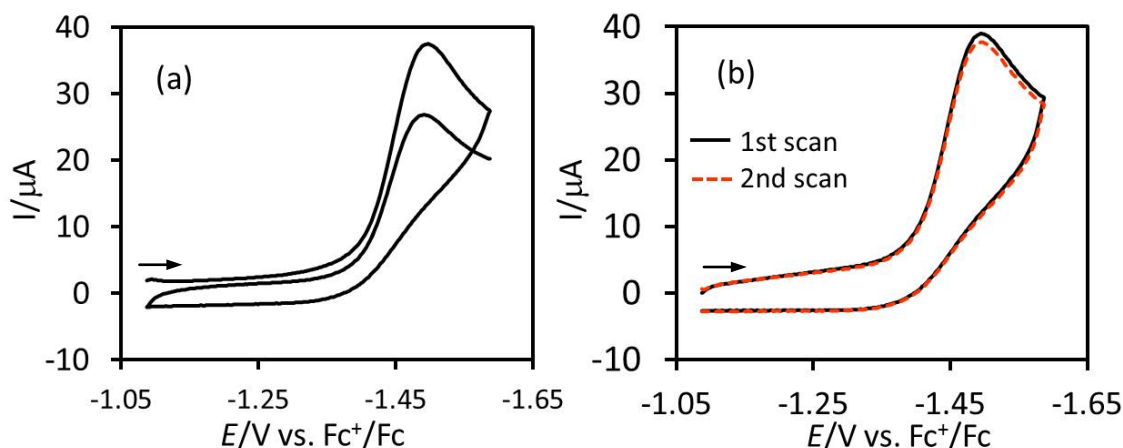


Figure 5.5 Cathodic current recoveries of **2** at different equilibration times. (a) 0 s equilibration time; (b) 30 s equilibration times between the 1st and the 2nd scan (b). Arrows indicate the direction of scans.

Scan Rate Dependence of Complex 2

Cyclic voltammograms of **2** in various scan rates provide supporting information for two electron reduction with inversion potential as shown in Figure 5.6. If slow and medium scan rates are used, the reduction undergoes $2 e^-$ processes suggesting that the reduced species from the first electron reduction has enough time to do structural change and can be reduced more easily with the second electron. At a faster scan rate, the normalized current is decreased close to a $1 e^-$ reduction process suggesting that structural rearrangement is slower than the scan rates, thus reduced species do not have enough time to rearrange geometry to gain another electron so it will be a $1 e^-$ process similar to those observed in PDT. Thus, the reduction process for **2** will be between $1 e^-$ and $2 e^-$ process.

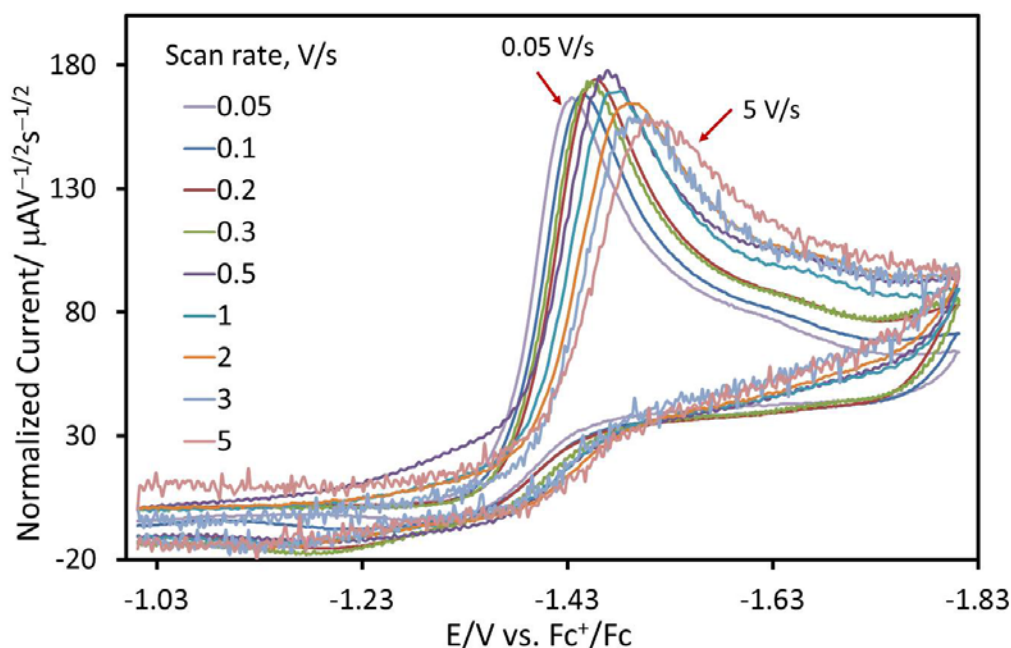


Figure 5.6 Cyclic voltammograms of **2** at various scan rates.

5.2 Electrocatalyzed Proton Reduction of Weak Acid

Electrocatalysis of the proton reduction of weak acids by **1** and **2** were tested with acetic acid (HOAc) in acetonitrile using a glassy carbon electrode. Voltammograms are shown in Figure 5.7. The current of the voltammetric peak associated with the first reduction at about -1.4 to -1.5 V does not change with adding acid. After adding acid a new peak at about -1.8 to -1.9 V is present and the current increases with increasing acid concentration. This behavior is analogous to that of known proton reduction catalyst complexes such as BDT and PDT (Felton *et al.*, 2007; Si, Hu, and Chen, 2008; Chong *et al.*, 2003; Yu *et al.*, 2008). Thus, the first reduction potential is related to primary reduction of neutral catalyst precursors to active states and the second potentials correspond to hydrogen production. When scan to more negative potential, the second catalytic peak was observed at about -2.2 to -2.3 V for both **1** and **2** (Figures C.1 and C.2 in Appendix C). This catalytic peak may interfere with the direct reduction of the HOAc

at the surface of the glassy carbon electrode.

A summary of electrochemical data of **1** and **2** in comparison with related complexes is shown in Table 5.1. The *anti*-[(μ -SMe)₂Fe₂(CO)₆] was prepared according to the literature procedure (Seyferth, Henderson, Song, and Womack, 1985). The cyclic voltammograms of *anti*-[(μ -SMe)₂Fe₂(CO)₆] with/without acid are similar in a behavior of **1** and **2**, see appendix C.11. The overpotentials of proton reduction from HOAc of **1** and **2** are relatively low compared to well-known BDT (Felton *et al.*, 2007) and PDT (Song *et al.*, 2008). At 20 mM HOAc, catalytic efficiency of **2** is comparable to that of BDT which falls in the top end of the medium range ($0.25 < C.E. < 0.75$). In fact, the catalysts with low overpotential all tend to have low catalytic efficiency (*C.E.*), an interesting exception is **2** with *C.E.* in the medium range and relatively low overpotential.

At added acid concentration of 2 mM to 20 mM, the currents of the catalytic peak of **2** is higher than those obtained from **1** until at 50 mM HOAc the catalytic current of **2** no longer increases and the peak potential shifts about 0.1 V in the negative direction. This observation suggests that a different reduction process may occur. Compounds with two catalytic processes have not previously been reported. Another observation on the presence of acid is a positive shift in the first reduction potential. The presence of HOAc results in a minimal shift (30-40 mV) of the primary reduction in a positive direction suggesting hydrogen bonding between the acid and catalyst and/or protonation of the catalyst precursor molecules which changes electron density on the metal centers (Yu *et al.*, 2008).

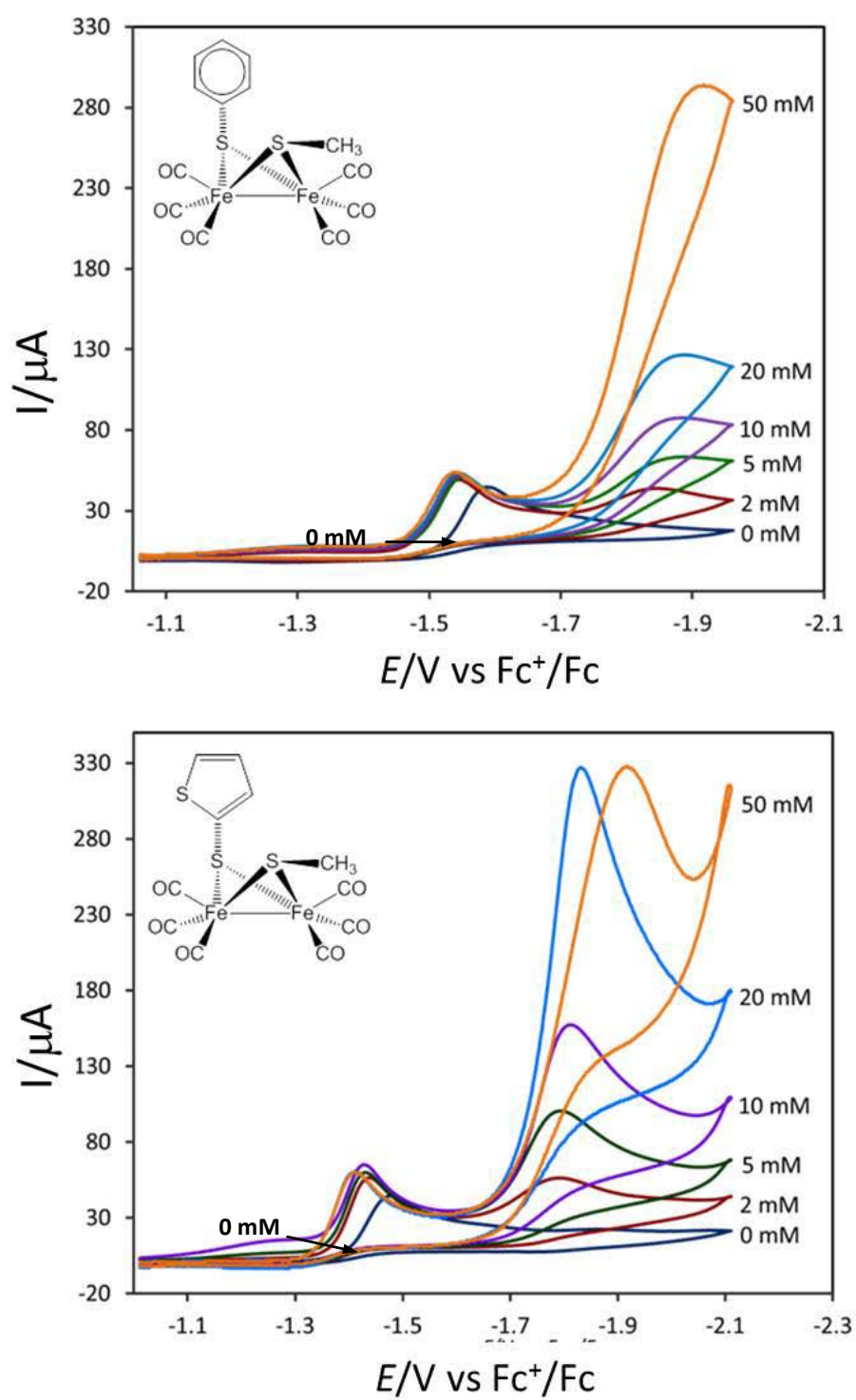


Figure 5.7 Cyclic voltammograms of **1** (top) and **2** (bottom) with varied concentrations of HOAc under N₂.

Table 5.1 Electrochemical data of **1**, **2**, and related diiron complexes in CH₃CN. All potentials are versus Fc⁺/Fc.

complex	E_{pa} [V]	E_{pc1} [V]	E_{pc2} [V]	E_{over}^c [V]	$C.E.^d$
1	0.68	-1.52	-1.88	-0.42	0.39 (M)
2	0.61	-1.46	-1.82	-0.36	0.66 (M)
BDT ^a	0.86	-1.32	-2.11	-0.65	0.66 (M)
PDT ^a	0.74	-1.74	-2.35	-0.89	0.06 (W)
<i>anti</i> -[(μ -SPh) ₂ Fe ₂ (CO) ₆] ^a	0.81	-1.44	-2.26	-0.80	0.22 (W)
<i>anti</i> -[(μ -SMe) ₂ Fe ₂ (CO) ₆] ^b	0.65	-1.66	-1.78	-0.28	0.09 (W)

^a All electrochemical data from Felton *et al.*, 2009.

^b *anti*-[(μ -SMe)₂Fe₂(CO)₆] was prepared for comparison the electrochemical data.

^c $E_{over} = E_{HOAc}^o - E_{pc2}$, E_{HOAc}^o , standard potential of HOAc (-1.46 V); E_{pc2} , the peak potential of the catalytic peak (Felton *et al.*, 2009). E_{over} for synthesized complexes calculated at 20 mM HOAc.

^d Catalytic efficiency ($C.E.$) = $(i_{cat}/i_d)/(C_{HOAc}/C_{cat})$, i_{cat} , the catalytic current; i_d , the current for reduction of the catalyst in the absence of acid; C_{HOAc} , the acid concentration; C_{cat} , the catalyst concentration (Felton *et al.*, 2009). $C.E.$ for synthesized complexes calculated at 20 mM HOAc.

Reduction Potential and Catalysis as Function of Acid Strength

Catalysis of **2** in the presence of different acids, phenol ($pK_a = 29.91$), 4-bromophenol ($pK_a = 25.53$), and cyanoacetic acid ($pK_a = 18$) (Eckert *et al.*, 2009) were investigated as shown in Figure 5.8.

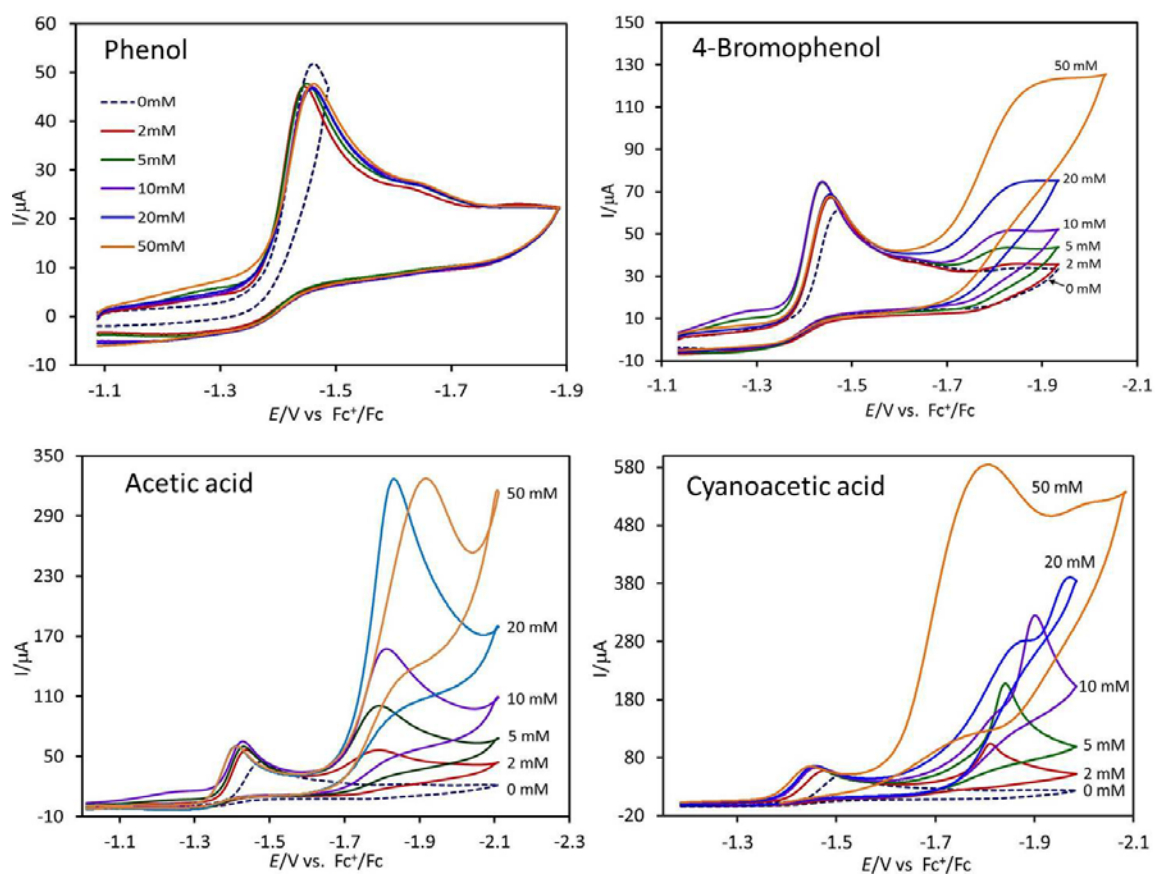


Figure 5.8 Cyclic voltammograms of **2** in the presence of different acids as indicated.

With the weakest acid, phenol, no potential shift and no catalytic current is observed, but as the acid strength is increased in the order 4-bromophenol < acetic acid < cyanoacetic acid, there is a corresponding increase in the catalytic current and potential shift in the first reduction peaks as summarized in Table 5.2.

Table 5.2 Peak shift on initial reduction and catalytic peak currents as function of acid strength.

acid	pK_a^a	peak shift (mV)	peak current at 10 mM acid (μA)
phenol	29.14	-	22
4-bromophenol	25.53	+16	15
acetic acid	23.51	+34	50
cyanoacetic acid	18	+42	100

^a pK_a from Eckert *et al.*, 2009

The positive shift in the first reduction peaks may be due to the protonation of reduced intermediates, stronger acids with more donation ability produce larger shifts on reduction. In the presence of 4-bromophenol, some catalysis occurs and in presence of the stronger cyanoacetic acid strong catalysis occurs and does not level off at 50 mM. However, there is some strange behavior at 20 mM and a strong shift to lower overpotential with high acid concentration which may indicate a different catalysis process.

Carbon Monoxide (CO) Atmospheric Dependence

Catalytic proton reduction under CO was studied for atmospheric dependence. The effect of atmosphere, either Ar or CO, was studied previously and in some cases, electrocatalytic proton reduction is strongly inhibited by CO as with PDT, but in other cases no effect on electrocatalysis is observed as with (μ -ethane-1,2-dithiolate) $Fe_2(CO)_6$ (EDT). This is punctuated by the formation of distinct reduced products (Borg, Tye, Hall, and Best, 2007; Chong *et al.*, 2003). Thus, the difference in CO inhibition is important

for understanding the intermediate and catalytic mechanism because DFT can predict on the favorable intermediate to react with CO.

In the absence of HOAc, the voltammograms of **2** scanned through the first reduction and continued to return scan to oxidation, compared with the oxidation scan shown in Figure 5.9, is similar to those observed under N₂ atmosphere. Reductive scans to more negative potential shown in Figure 5.10 show atmospheric dependence behavior. The first reduction occurs at -1.46 V with slightly more reversibility and more current. When scanned to more negative potential the second reduction peak at -2.3 V is observed with almost the same current of the first reduction peak. More peak current and reversibility under CO indicate the prevalence of the species formed in the cathodic scan. Also the small reduction event around -1.9 to -2.0 V seen under N₂ is not observed. The initial oxidation occurs at 0.66 V and the oxidation of reduction products are observed about -0.5 to -0.6 V.

In the presence of added HOAc under CO atmosphere shown in Figure 5.11, the catalytic reduction peak at -1.8 to -1.9 V observed under N₂ completely disappears. Either additional CO inhibits formation of the catalytically active species or CO reacts with the catalyst to effectively remove it from the cycle. This agrees with the protonation of reductive intermediate by donor molecules.

The first catalytic peak occurs at more negative potentials about -2.2 to -2.3 V attributed to the direct reduction of the HOAc at the surface of the GC electrode (-2.3 V vs. Fc⁺/Fc). The effect of direct reduction becomes a problem as more acid is added (Felton, Glass, Lichtenberger, and Evans, 2006).

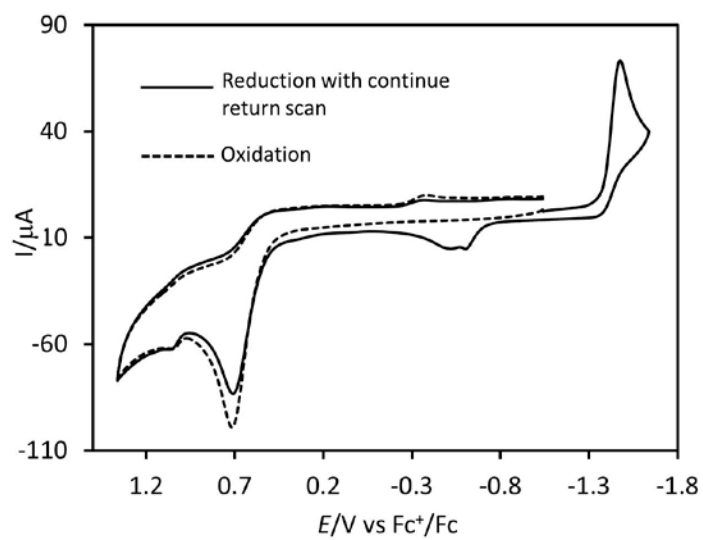


Figure 5.9 Cyclic voltammograms of **2** under CO atmosphere without added acid.

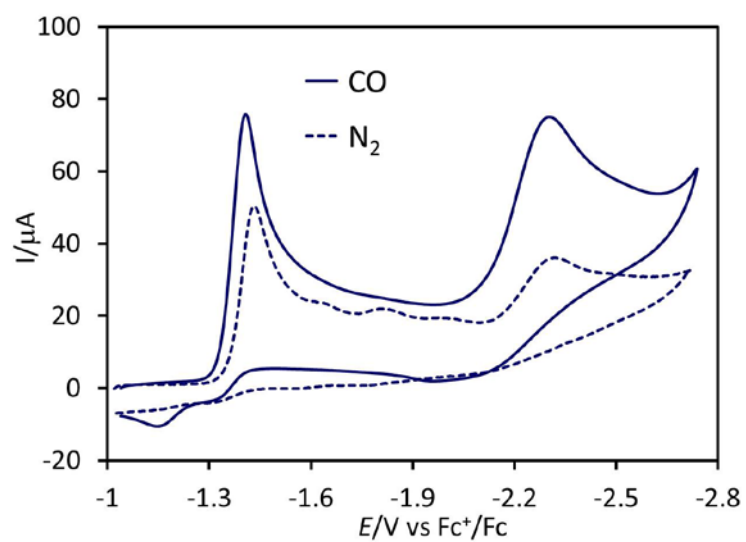


Figure 5.10 Atmospheric dependence of reduction scans of **2**.

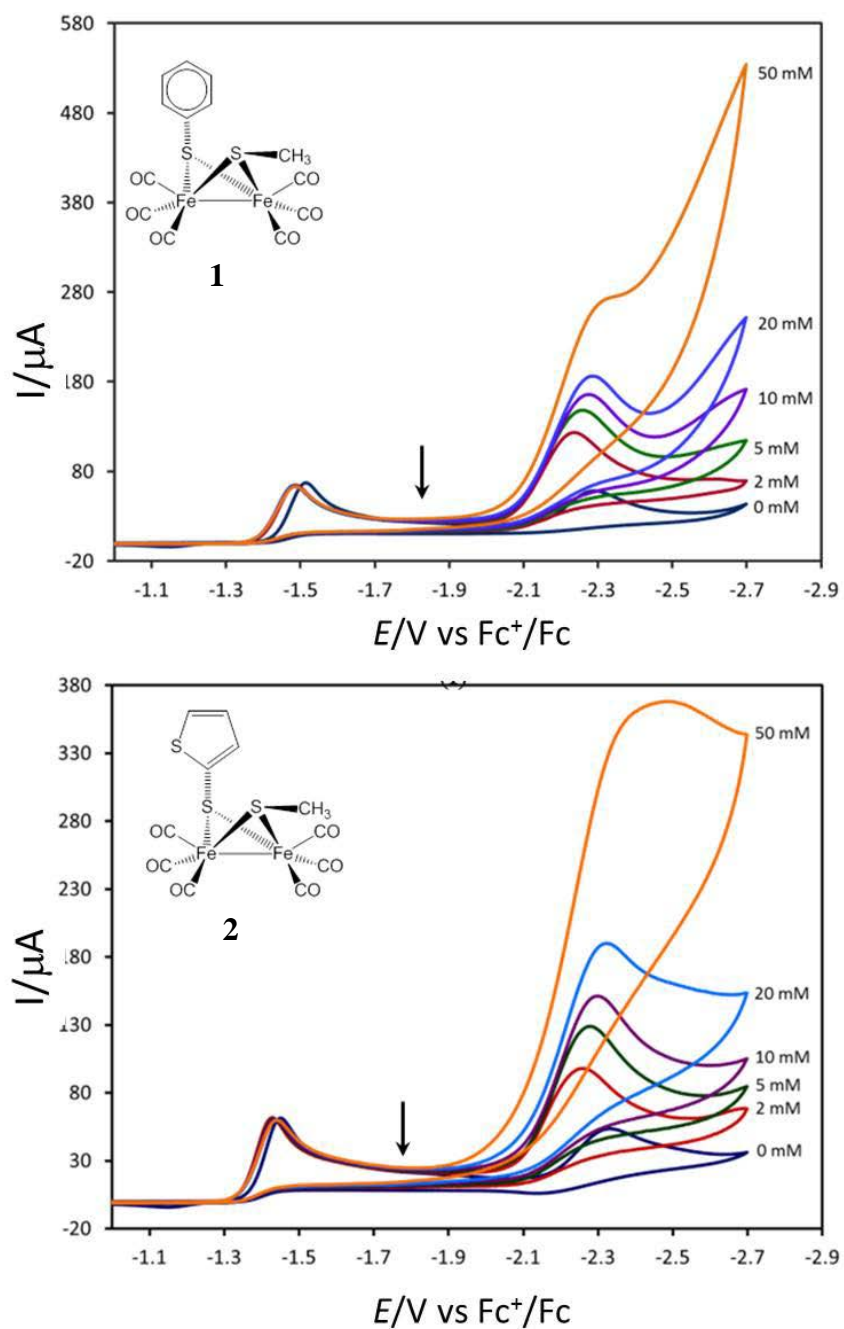


Figure 5.11 Voltammograms of **1** and **2** with varied concentrations of HOAc under CO atmosphere. Arrows indicate the potentials at catalytic reduction occur under N_2 which completely disappear under CO atmosphere.

Reduction Potential as Function of Repeating Scans

Under N_2 -saturated solution, reduction scan of **1** without acid were repeated 13 times with 30 s stirring and no polishing of the electrode between scans. The catalytic peak at around -2.2 V clearly shows a progressively positive shift from scan 1 to scan 13. After scan 13, the solution was stirred for 30 min, then taken another reduction scan, indicated as scan 14. The reduction peaks of scan 14 shifted back close to those of scan 1 as shown in Figure 5.12a. One possible explanation of this positive shift is electrode coating by reduced species. This electrode coating is not strong and can drift away if the solution is stirred. Under CO-saturated solution without acid, reduction scans were repeated 10 times, only minimal potential shift was observed suggesting no significant coating on the electrode surface as shown in Figure 5.12b. In the presence of 50 mM acetic acid under N_2 -saturated solution, the negative scan was repeated 16 times, reduction at around -2.2 V also shows progressive shifting in the positive direction to -2.0 V and no more shift for scans 17 and 18 suggesting that 16 scans provides the maximum coating on the electrode as shown in Figure 5.13a. Under CO with added 50 mM acetic acid shows similar results with no acid under CO atmosphere. The minimal shifts were observed as shown in Figure 5.13b, suggesting no electrode coating under CO-saturated solution with and without added acid.

The shift of catalytic potential about 0.2 V in a positive direction should be good potential for catalysis process because the catalytic cycle can be continued repeated while lowering potential is required.

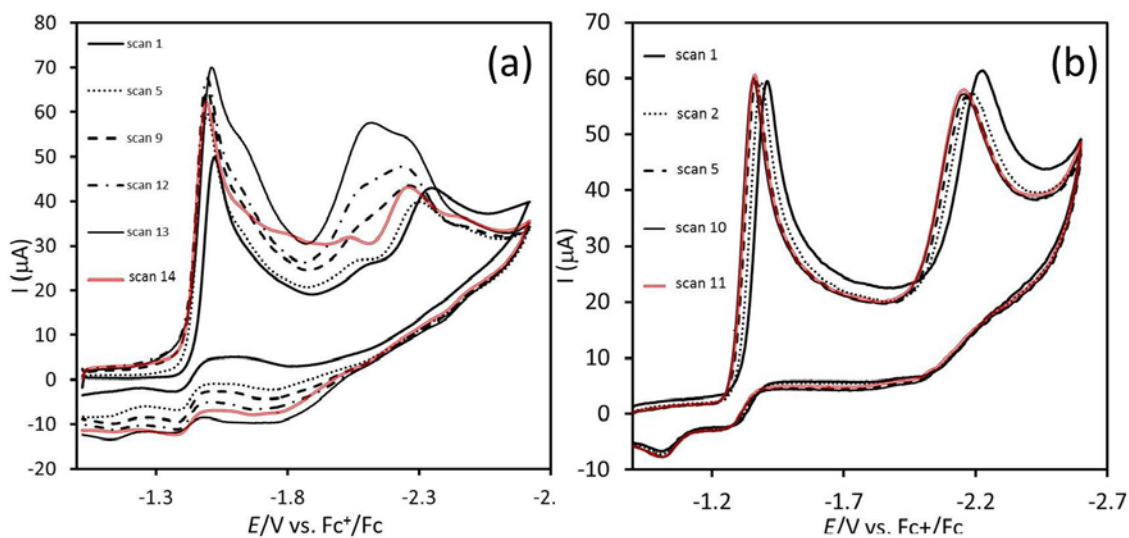


Figure 5.12 Reduction potential as function of repeating scan of **1** in the absence of acid under N₂ (a) and CO (b) atmospheres. Only representative scans are shown for clarify.

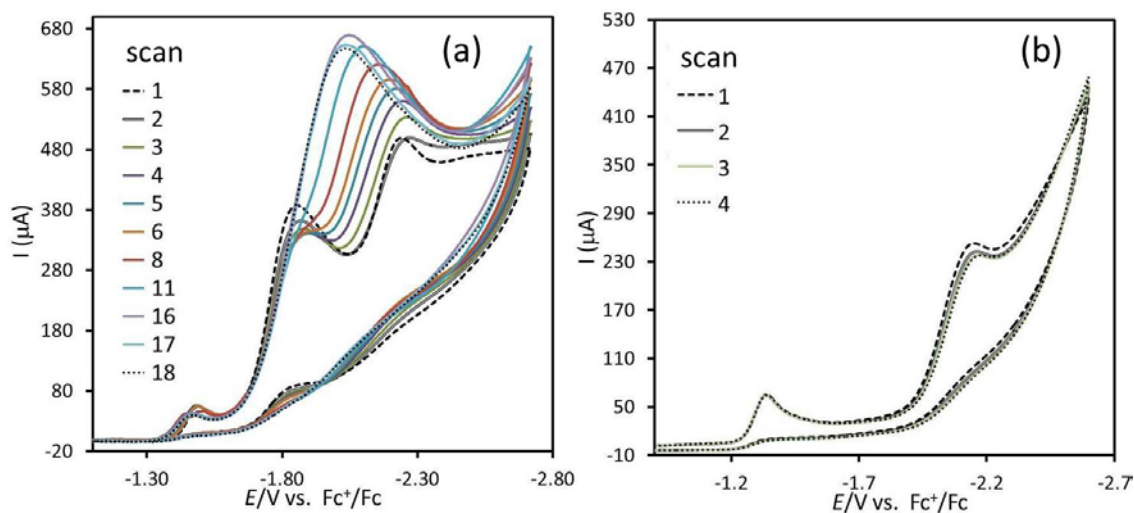


Figure 5.13 Catalytic potential as function of repeating scan of **1** in the presence of 50 mM acetic acid under N₂ (a) and CO (b) atmospheres. Only representative scans are shown for clarify.

5.3 IR Spectra of Reduced Species

In order to obtain further evidence to get more information on the structure of reduction products, a bulk electrolysis experiment on **1** was performed under CO in THF solution with Bu_4NPF_6 as supporting electrolyte. Reticulated vitreous carbon was used as working electrode due to its large surface area in order to increase the rate of electrolysis. The potential in the bulk electrolysis experiment was held at -1.6 V for 10 min to produce a large amount of reduction products of **1**. The IR spectrum in the νCO stretching region of the electrolyte solution before and after the bulk electrolysis experiment are shown in Figure 5.14.

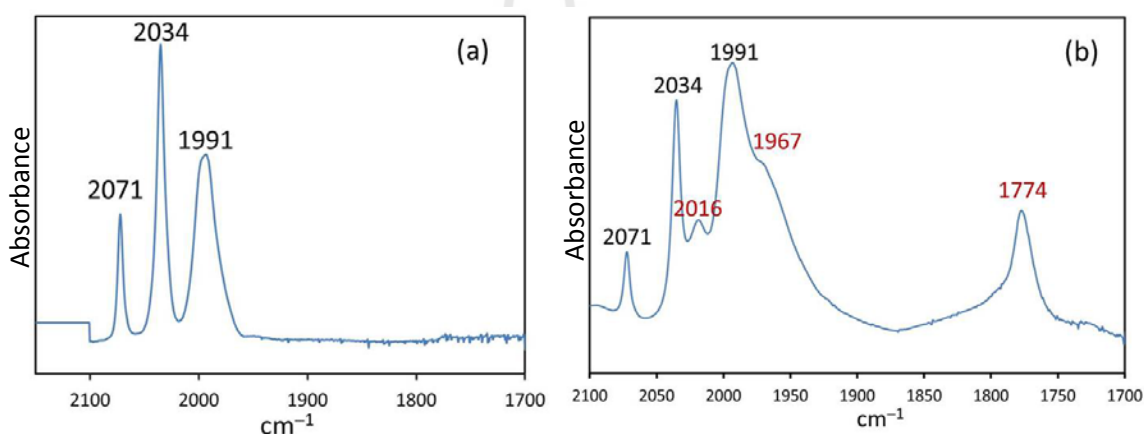


Figure 5.14 IR spectra in the νCO stretching region of electrolyte solution recorded prior (a) and after (b) 10 min bulk electrolysis of **1**. 4 mM of **1** in a CO-saturated THF (0.4 M $n\text{-Bu}_4\text{NPF}_6$) solution at -1.6 V electrolysis.

The IR spectrum of the electrolyte solution before bulk electrolysis, showed three νCO stretching bands at 2071, 2034, and 1991 cm^{-1} while the IR spectrum of the electrolyte solution after electrolysis shows the three original νCO stretching bands corresponding to unreacted complex **1** and new three bands at lower frequencies, 2016, 1967, and 1774 cm^{-1} corresponding to the reduction product of **1**. The new νCO stretching band at 1774 cm^{-1} corresponds to bridging CO coordination (1700-1850 cm^{-1})

indicating the formation of bridging CO in the reduced intermediate.

5.4 Density Functional Theory Study

The mechanism of the first reduction, two e^- process with potential inversion, has been proposed and the second reduction event observed in the presence of HOAc corresponds to the formation of molecular hydrogen (Song *et al.*, 2007; Song, Yin *et al.*, 2007; Chong *et al.*, 2003; Felton *et al.*, 2007). The electrocatalyzed proton reduction observed in **1** and **2** is fairly typical for many catalysts with neutral molecules as precatalysts and proton reduction catalyzed by their reduced species. However, the process of the catalysis peak is more complicated and there can be many different processes. DFT calculation is a useful method to provide a reasonable mechanism for molecular hydrogen production. Many proposed mechanisms for hydrogen production from $2Fe_2S$ complexes were developed through electrochemical data combined with DFT calculations, for example, protonation of the sulfur or carbonyl ligand (Borg *et al.*, 2004; Borg, Tye, Hall, and Best, 2007), disproportionation (Capon *et al.*, 2007), dimerization (Best, Borg, White, Razavet, and Pickett, 2007; Aguirre de Carcer, DiPasquale, Rheingold, and Heinekey, 2006) and protonation as bringing on diiron centers (Felton *et al.*, 2007).

In this work, some possible reduced intermediates have been investigated computationally to aid understanding of the reduction mechanism.

Proposed Reduced Species of **2**

The voltammogram of **2** is shown in Figure 5.15 with number labeling to indicate each stage of the proposed mechanism.

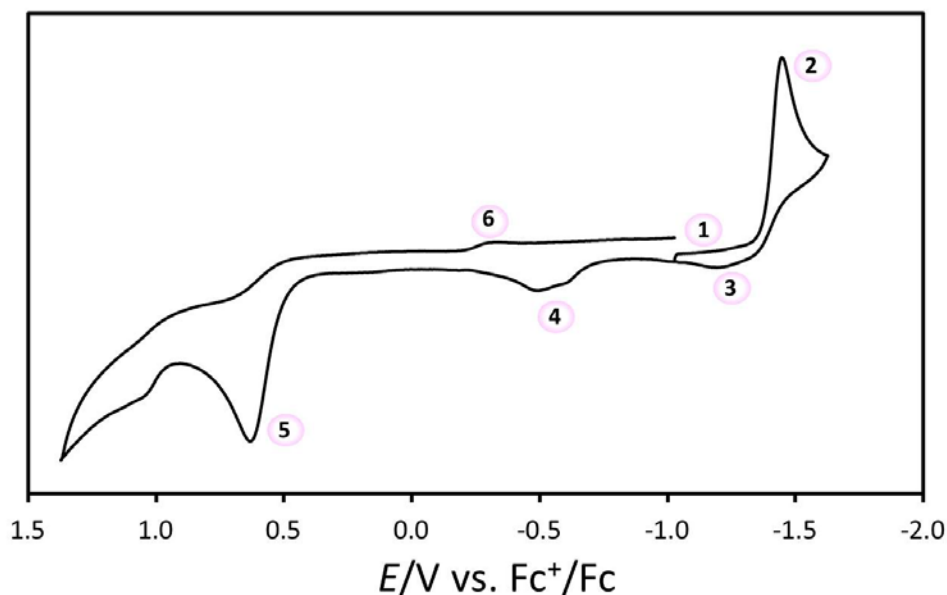


Figure 5.15 Voltammogram of **2** in the absence of HOAc under N₂ atmosphere.

In the absence of added acid, **2** undergoes an irreversible 2 electron reduction with potential inversion occurring at -1.46 V. The proposed steps in the process are described below and the calculation results summarized in Tables 5.3 and 5.4.

Stage 1 At the starting point, only the neutral complex **2** is present.

Stage 2 On a negative scan to around -1.5 V, a two electron reduction with potential inversion occurs at -1.46 V. Three possibilities of reduction pathway were calculated:

I. Introduction of the first electron produces a dimer anion with terminal CO ligands with a calculated reduction potential of -1.60 V, then the second electron comes in producing a dimer dianion which dissociates to two different monomer anions of $[(\mu\text{-SMe})\text{Fe}(\text{CO})_3]^-$ and $[(\mu\text{-STh})\text{Fe}(\text{CO})_3]^-$. The second reduction occurs more easily than the first reduction with potential calculated at -1.27 V. Thus, potential inversion of two electron reduction was calculated to -1.43 V which is close to the experimental value. The calculated ΔG for dissociation of the dimer dianion to monomer anions is favorable ($\Delta G = -11.75$ kcal/mol)





II. Introduction of the first electron produces a dimer anion in rotated form which contains a cleaved Fe–STh bond and bridging carbonyl giving structure change with a calculated reduction potential of -1.53 V and the second electron produces a rotated dimer dianion calculated to -1.18 V. Thus potential inversion of two electron reduction was calculated to -1.35 V.



Dissociation of dianion **2b** is calculated to be unfavorable.

III. Similar to process proposed in II but dianion (**2c**) contains a cleaved Fe–SMe bond instead of a cleaved Fe–STh bond. Because the two thiolate substituents in this complex are different, the calculated reduction potential with potential inversion is -1.53 V and dissociation of dianion **2c** is calculated to be unfavorable.



All of these will most closely correlate to the electrochemical experiment since the reduction observed is an average of two reduction processes is -1.46 V.

Stage 3 This reversible portion is proposed to be the oxidation of the rotated dimer dianion (**2b**) back to neutral dimer (**2**) which is calculated to occur at -1.35 V.

Stage 4 Oxidation of unknown reduced species. Calculated oxidation potential of two monomer anions is far from the experimental value that occur about -0.5 V



Thus, the monomer anion may not be the reduced products. Dimerization of iron dimer may be another possibility. However, there are many possible dimer structures such as dimerization by form Fe–Fe bond between two 2Fe2S units, dimerization through

S atom of thiolate group, or dimerization of thiophene unit because thiophene can be electropolymerized through active alpha carbon position (Wei, Chan, Tian, Jang, and Hsueh, 1991).

Stage 5 Irreversible two electron oxidation of complex **2**.

Stage 6 Reduction of unknown oxidative species.

Table 5.3 Proposed reduction mechanism with calculated reduction potential (V) and Gibbs energy of calculated reaction (kcal/mol).

1	$[(\mu\text{-SMe})(\mu\text{-STh})\text{Fe}_2(\text{CO})_6]$	
2	I. $[(\mu\text{-SMe})(\mu\text{-STh})\text{Fe}_2(\text{CO})_6] (\mathbf{2}) \longrightarrow [(\mu\text{-SMe})(\mu\text{-STh})\text{Fe}_2(\text{CO})_6]^{2-} (\mathbf{2a})$	-1.43 V
	$\mathbf{2a} \longrightarrow [(\text{SMe})\text{Fe}(\text{CO})_3]^- + [(\text{STh})\text{Fe}(\text{CO})_3]^-$	-11.72 kcal/mol
	II. $[(\mu\text{-SMe})(\mu\text{-STh})\text{Fe}_2(\text{CO})_6] (\mathbf{2}) \longrightarrow$	
	$[(\mu\text{-SMe})(\text{STh})\text{Fe}_2(\mu\text{-CO})(\text{CO})_5]^{2-} (\mathbf{2b})$	-1.35 V
	III. $[(\mu\text{-SMe})(\mu\text{-STh})\text{Fe}_2(\text{CO})_6] (\mathbf{2}) \longrightarrow$	
	$[(\text{SMe})(\mu\text{-STh})\text{Fe}_2(\mu\text{-CO})(\text{CO})_5]^{2-} (\mathbf{2c})$	-1.53 V
3	$[(\mu\text{-SMe})(\text{STh})\text{Fe}_2(\mu\text{-CO})(\text{CO})_5]^{2-} (\mathbf{2b}) \longrightarrow$	
	$[(\mu\text{-SMe})(\mu\text{-STh})\text{Fe}_2(\text{CO})_6] (\mathbf{2})$	-1.35 V
4	I. $[(\mu\text{-STh})\text{Fe}(\text{CO})_3]^- \longrightarrow [(\mu\text{-STh})\text{Fe}(\text{CO})_3]$	-1.03 V
	$[(\mu\text{-SMe})\text{Fe}(\text{CO})_3]^- \longrightarrow [(\mu\text{-SMe})\text{Fe}(\text{CO})_3]$	-0.71 V
	II. $[(\mu\text{-SMe})(\mu\text{-STh})\text{Fe}_2(\text{CO})_6]^- \longrightarrow [(\mu\text{-SMe})(\mu\text{-STh})\text{Fe}_2(\text{CO})_6] (\mathbf{2})$	-0.56 V
	$[(\mu\text{-STh})\text{Fe}(\text{CO})_3]^- + [(\mu\text{-SMe})\text{Fe}(\text{CO})_3] \longrightarrow [(\mu\text{-SMe})(\mu\text{-STh})\text{Fe}_2(\text{CO})_6]^-$	-12.87 kcal/mol
	$[(\mu\text{-SMe})\text{Fe}(\text{CO})_3]^- + [(\mu\text{-STh})\text{Fe}(\text{CO})_3] \longrightarrow [(\mu\text{-SMe})(\mu\text{-STh})\text{Fe}_2(\text{CO})_6]^-$	-5.57 kcal/mol
5	$[(\mu\text{-SMe})(\mu\text{-STh})\text{Fe}_2(\text{CO})_6] \longrightarrow \text{unknown}^{2+} \text{ or unknown } \text{A}^+ / \text{unknown } \text{B}^+$	
6	Reduction of unknown oxidative species	

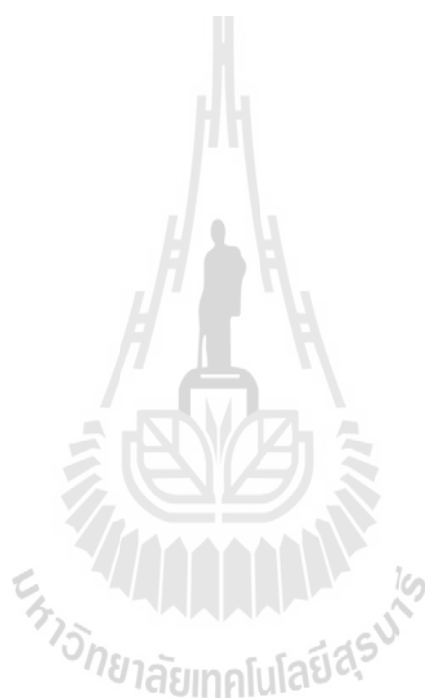
Table 5.4 Calculated pK_a and binding energy (kcal/mol) of MeCN or CO to proposed reduced species.

Protonated monomer anion		
$[(SMe)Fe(CO)_3]^- + H^+ \longrightarrow [(SMe)HFe(CO)_3]$		13.9
$[(STh)Fe(CO)_3]^- + H^+ \longrightarrow [(STh)HFe(CO)_3]$		15.2
Protonated rotated dimer anion		
$[(\mu-SMe)(STh)Fe_2(\mu-CO)(CO)_5]^{2-} + H^+ \longrightarrow [(\mu-SMe)(HSTh)Fe(CO)_5(\mu-CO)]^-$		20.7
$[(SMe)(\mu-STh)Fe_2(\mu-CO)(CO)_5]^{2-} + H^+ \longrightarrow [(HSM e)(\mu-STh)Fe(CO)_5(\mu-CO)]^-$		26.8
Binding energy of acetonitrile solvent to monomer anion		
$[(SMe)Fe(CO)_3]^- + MeCN \longrightarrow [(SMe)Fe(CO)_3(NCMe)]^-$		16.99 kcal/mol
$[(STh)Fe(CO)_3]^- + MeCN \longrightarrow [(STh)Fe(CO)_3(NCMe)]^-$		21.16 kcal/mol
Binding energy of CO to monomer anion		
$[(\mu-SMe)Fe(CO)_3]^- + CO \longrightarrow [(\mu-SMe)Fe(CO)_4]^-$		-15.23 kcal/mol
$[(\mu-STh)Fe(CO)_3]^- + CO \longrightarrow [(\mu-STh)Fe(CO)_4]^-$		-22.98 kcal/mol

Different protonated anions were calculated for pK_a to gain understanding how proton from acid binds to active catalysts before generates hydrogen. Calculated pK_a were proposed for protonation forms of monomer anions and rotated dimer anions. According to calculated pK_a , more possible protonation species should be protonated rotated dimer anion which proton protonated at Fe atom linked to methyl thiolate ligand, $[(HSM e)(\mu-STh)Fe(CO)_5(\mu-CO)]^-$, because calculated pK_a of this species is higher than pK_a of acetic acid ($pK_a = 22.3$) so acetic acid more favorable act as proton donor.

Binding energy of acetonitrile solvent to the monomer anion is not favorable suggesting that acetonitrile solvent does not bind to the Fe center so proton reduction processes can proceed. In saturated CO atmosphere, CO can bind to Fe centers of monomer anions and inhibit the proton reduction mechanism. However, calculated oxidation of monomer anion is far from observed values. This calculation agrees with IR

results which suggest that reduced species should contain bridging CO. However more evidence is still needed to gain understanding on the structure of the reduced intermediates.



CHAPTER VI

CONCLUSIONS AND FUTURE DIRECTIONS

6.1 Conclusions

An ideal hydrogen production for an alternative energy economy would be light-driven proton reduction and hopefully water would be a proton source with robustness, high efficiency and cheap catalysts. From the basic point of view, utilizing the combination of DFT calculations, with the outcome of electrochemical and spectroscopic techniques should help in the development and understanding [2Fe2S] catalysts in general and this capability may help to design new catalysts to reach the ideal.

Inspired by the active sites of hydrogenase enzymes, many active site mimic of the formula $[(\mu\text{-SR})_2\text{Fe}_2(\text{CO})_6]$ have been synthesized and studied for their ability to electrocatalyze hydrogen production (Felton *et al.*, 2009). This work focused on the synthesis and study of bis-thiolate diiron hexacarbonyl complexes for hydrogenase active-site-inspired catalysts. The formula complexes $[(\mu\text{-SR})(\mu\text{-SR}')\text{Fe}_2(\text{CO})_6]$, R = Me, R' = Ph or Th, were prepared by Grignard cleavage of $[(\mu\text{-S}_2)\text{Fe}_2(\text{CO})_6]$ followed by methylation. $^1\text{H-NMR}$ spectroscopy shows three isomeric products were formed, Me **a**/R **e**, Me **e**/R **a**, and Me **e**/R **e** isomer. The *anti*-isomers of each formula complexes were isolated and more thermodynamic stable isomers, Me **e**/Ph **a** (**1**) and Me **e**/Th **a** (**2**) have been fully characterized and studied for their ability to electrocatalyze proton reduction producing molecular hydrogen.

The electronic properties of diiron hexacarbonyl complexes can be

experimentally observed by spectroscopic, electrochemical, and structural studies. Electron richness of diiron centers can be observed from the red shift of the IR spectrum in the carbonyl stretching region, an anodic shift in reduction potential, lengthening of the Fe–Fe bond, and further supported by calculated HOMO by DFT. Complex **1** with a more electron rich in diiron center than that of **2** because thienyl group in **2** has a better electron-withdrawing ability.

The electrochemistry of **1** and **2** revealed their ability to be good catalysts. It catalyzed proton reduction from acetic acid in acetonitrile solution at relative low overpotentials. The first reduction is an irreversible two electron reduction with inversion potentials occurring at -1.4 to -1.5 V and the first catalytic reduction occurs about -1.7 to -1.8 V. It is noted that the cyclic voltammograms of **1** and **2** show strong atmospheric dependence. The catalytic process inhibited under a CO atmosphere suggests that the electroactive catalysts occurring under N_2 are noticeably suppressed. The significant different catalysis behavior was found for **2** at 50 mM acetic which no more current increase and also potential shift to negative direction suggesting a different process may take place.

In the presence of acid, the shift in initial reduction in positive direction is observed which suggest the protonation on reduced species may occur and lower electron density at the iron center. The shift of initial reduction and catalytic activity is increase as function of acid strength.

DFT calculations gave a good agreement with calculated electronic properties and geometry of neutral molecules. To understand the reduction process, some of the possible intermediate models had to be calculated including rotated dianion and reduction with dissociation to two different iron monomer anion, however these models cannot match with experimental voltammogram. The IR spectrum in CO stretching

region of reduced species show absorption band at 1774 cm^{-1} suggesting that the reduced species contain bridging CO ligand.

6.2 Future Directions

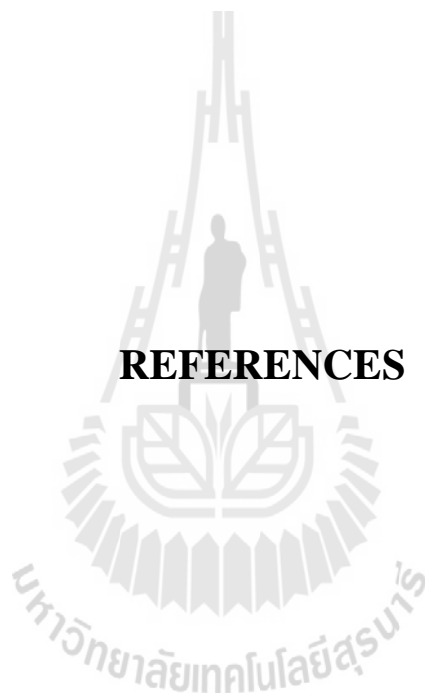
The mechanism for *bis*-thiolato diiron hexacarbonyl complexes has not been properly developed. A different model of electroactive species should be investigated to fit calculation results with experimental electrochemical behaviors. Calculation of NMR chemical shift of methyl group should be helpful to support the interpretation of structural isomer and may be useful to complexes for which it is difficult to get suitable single crystals for X-ray diffraction data.

Spectroelectrochemistry (SEC), combination of electrochemistry and IR spectroscopy, would be helpful experiments to provide more detailed indication of structural dynamics during reduction and protonation step. Although, these techniques may give a complicated spectrum because many species may be present during the reaction, it can be useful to guide on structure changes from electronic properties change.

Controlled potential coulometry (CPC), a combination of controlled-potential electrolysis technique and measurement of the quantity of electricity, should be a useful experiment to derive the accurate number of electron shuttling in the system (Jainn *et al.*, 2011; Mejia-Rodriguez, Chong, Reibenspies, Soriaga, and Darensbourg, 2004).

New catalysts containing light absorption unit ligands, such as oligomer thiophene or quantum dot could be synthesized and studied for catalytic activity for aim light driving hydrogen production (Ott *et al.*, 2004; Ott, Kritikos, Åkermark, and Sun, 2003; Reisner, Powell, Cavazza, Fontecilla-Camps, and Armstrong, 2009)

REFERENCES



REFERENCES

- Adams, M. W. W. (1990). The Structure and Mechanism of Iron-Hydrogenases. **BBA-Bioenergetics** 1020: 115-145.
- Adams, R. D., Cotton, F. A., Cullen, W. R., Hunter, D. L., and Mihichuk, L., (1975). Fluxional Behavior of Some Dinuclear Iron and Cobalt Hexacarbonyl Compounds with Alkylsulfur and Dialkylphosphorus, -Arsenic, -Germanium, and -Tin Bridges. **Inorg. Chem.** 14: 395-1399.
- Adeleke, J. A., Chen, Y.-W., and Liu, L.-K. (1992). Preparation and Crystal Structures of Iron Complexes *syn*- $[(\mu\text{-SPh})\text{Fe}(\text{CO})_3]_2$, $(\text{C}_5\text{H}_4\text{SPh})_2\text{Fe}$, $(\text{C}_5\text{H}_5)\text{Fe}(\text{C}_5\text{H}_4\text{SPh})$, and $(\text{C}_5\text{H}_4\text{SPh})\text{Fe}(\text{C}_5\text{H}_4\text{PPh}_2)$. **Organometallics** 11: 2543-2650.
- Aguirre de Carcer, I., DiPasquale, A., Rheingold, A. L., and Heinekey, D. M. (2006). Active-Site Models for Iron Hydrogenases: Reduction Chemistry of Dinuclear Iron Complexes. **Inorg. Chem.** 45: 8000-8002.
- Allen, F. (2002). The Cambridge Structural Database: a Quarter of a Million Crystal Structures and Rising. **Acta Cryst. B** 58: 380-388.
- Althoff, G., Ruiz, J., Rodriguez, V., Lopez, G., Perez, J., and Janiak, C. (2006). Can a Single C–HF–C Hydrogen Bond Make a Difference? Assessing the HF Bond Strength from 2-D 1H-19F CP/MAS NMR. **Cryst. Eng. Comm.** 8: 662-665.
- Anderson, K. M., Goeta, A. E., and Steed, J. W. (2008). Supramolecular Synthon Frustration Leads to Crystal Structures with $Z' > 1$. **Cryst. Growth Des.** 8:

2517-2524.

Armstrong, F. A. (2004). Hydrogenases: Active Site Puzzles and Progress. **Curr.**

Opin. Chem. Biol. 8: 133-140.

Artero, V. and Fontecave, M. (2005). Some General Principles for Designing Electrocatalysts with Hydrogenase Activity. **Coord. Chem. Rev.** 249: 1518-1535.

Best, S. P., Borg, S. J., White, J. M., Razavet, M., and Pickett, C. J. (2007). On the Structure of a Proposed Mixed-Valent Analogue of the Diiron Subsite of [FeFe]-Hydrogenase. **Chem. Commun.** 4348-4350.

Bennett, B., Lemon, B. J., and Peters, J. W. (2000). Reversible Carbon Monoxide Binding and Inhibition at the Active Site of the Fe-Only Hydrogenase. **Biochemistry** 39: 7455-7460.

Borg, S. J., Behrsing, T., Best, S. P., Razavet, M., Liu, X., and Pickett, C. J. (2004). Electron Transfer at a Dithiolate-Bridged Diiron Assembly: Electrocatalytic Hydrogen Evolution. **J. Am. Chem. Soc.** 126: 16988-16999.

Borg, S. J., Tye, J. W., Hall, M. B., and Best, S. P. (2007). Assignment of Molecular Structures to the Electrochemical Reduction Products of Diiron Compounds Related to [FeFe] Hydrogenase: A Combined Experimental and Density Functional Theory Study. **Inorg. Chem.** 46: 384-394.

Cabeza, J. A., Martinez-Garcia, M. A., Riera, V., Ardura, D., and Garcia-Granda, S. (1998). Binuclear Iron(I), Ruthenium(I), and Osmium(I) Hexacarbonyl Complexes Containing a Bridging Benzene-1,2-Dithiolate Ligand. Synthesis, X-Ray Structures, Protonation Reactions, and EHMO Calculations. **Organometallics** 17: 1471-1477.

- Capon, J. -F., Ezzaher, S., Gloaguen, F., Petillon, F. Y., Schollhammer, P., Talarmin, J., Davin, T. J., McGrady, J. E., and Muir, K. W. (2007). Electrochemical and Theoretical Investigations of the Reduction of $[\text{Fe}_2(\text{CO})_5\text{L}\{\mu\text{-SCH}_2\text{XCH}_2\text{S}\}]$ Complexes Related to [FeFe] Hydrogenase. **New J. Chem.** 31: 2052-2064.
- Capon, J.-F., Gloaguen, F., Pétilion, F. Y., Schollhammer, P., and Talarmin, J. (2008). On the Electrochemistry of Diiron Dithiolate Complexes Related to the Active Site of the [FeFe]H₂ase. **C. R. Chim.** 11: 842-851.
- Capon, J.-F., Gloaguen, F., Schollhammer, P., and Talarmin, J. (2005). Catalysis of the Electrochemical H₂ Evolution by Di-Iron Sub-Site Models. **Coord. Chem. Rev.** 249: 1664–1676.
- Ceperley D. M. and Alder, B. J. (1980). Ground State of the Electron Gas by a Stochastic Method. **Phys. Rev. Lett.** 45: 566-569.
- Chen, J., Vannucci, A. K., Mebi, C. A., Okumura, N., Borowski, S. C., Swenson, M., Lockett, L. T., Evans, D. H., Glass, R. S., and Lichtenberger, D. L. (2010). Synthesis of Diiron Hydrogenase Mimics Bearing Hydroquinone and Related Ligands. Electrochemical and Computational Studies of the Mechanism of Hydrogen Production and the Role of O–H···S Hydrogen Bonding. **Organometallics** 29: 5330–5340.
- Chong, D., Georgakaki, I. P., Mejia-Rodriguez, R., Sanabria-Chinchilla, J., Soriaga, M. P., and Darensbourg, M. Y. (2003). Electrocatalysis of Hydrogen Production by Active Site Analogues of the Iron Hydrogenase Enzyme: Structure/Function Relationships. **Dalton Trans.** 4158-4163.

- Cotton, F. A. and Troup, J. M. (1974). A 2,2'-Bipyridine Derivative of Diiron Nonacarbonyl, $\text{Fe}_2(\text{CO})_7\text{dipy}$. Some Observations on the Nature and Function of Semibridging Carbonyl Groups. **J. Am. Chem. Soc.** 96: 1233-1234.
- Ctech-Global Pte Ltd. The Manifold Image. (Online) Available: <http://ctech-global.com/ProductMain.aspx?ProductDetail=Vacuum>, access on 10 August 2012.
- Darchen, A., Mousser, H., and Patin, H. (1988). Two-Electron Transfer Catalysis of Carbon Monoxide Exchange with a Ligand in Hexacarbonyl Di-iron Compounds $[(\mu\text{-RS})_2\text{Fe}_2(\text{CO})_6]$. **Chem. Commun.** 14: 968-970.
- Darensbourg, M. Y., Lyon, E. J., and Smee, J. J. (2000). The Bio-Organometallic Chemistry of Active Site Iron in Hydrogenases. **Coord. Chem. Rev.** 206-207: 533-561.
- Desiraju, G. R. (2006). On the Presence of Multiple Molecules in the Crystal Asymmetric Unit ($Z' > 1$). **Cryst. Eng. Comm.** 9: 91-92.
- Eckert, F., Leito, I., Kaljurand, I., Kütt, A., Klamt, A., and Diedenhofen, M. (2009). Prediction of Acidity in Acetonitrile Solution with COSMO-RS. **J. Comp. Chem.** 30: 799-810.
- Einstein, A. (1905). Über einen Erzeugung und Verwandlung des Lichtes Betreffenden Heuristischen Gesichtspunkt. **Ann. Phys.** 322:132-148.
- Felton, G. A. N., Glass, R. S., Lichtenberger, D. L., and Evans, D. H. (2006). Iron-Only Hydrogenase Mimics. Thermodynamic Aspects of the Use of Electrochemistry to Evaluate Catalytic Efficiency for Hydrogen Generation. **Inorg. Chem.** 45: 9181-9184.

- Felton, G. A. N., Mebi, C. A., Petro, B. J., Vannucci, A. K., Evans, D. H., Glass, R. S., and Lichtenberger, D. L. (2009). Review of Electrochemical Studies of Complexes Containing the Fe₂S₂ Core Characteristic of [FeFe]-Hydrogenases Including Catalysis by These Complexes of the Reduction of Acids to Form Dihydrogen. **J. Organomet. Chem.** 694: 2681-2699.
- Felton, G. A. N., Vannucci, A. K., Chen, J., Lockett, L. T., Okumura, N., Petro, B. J., Zakai, U. I., Evans, D. H., Glass, R. S., and Lichtenberger, D. L. (2007). Hydrogen Generation from Weak Acids: Electrochemical and Computational Studies of a Diiron Hydrogenase Mimic. **J. Am. Chem. Soc.** 129: 12521-12530.
- Felton, G. A. N., Vannucci, A. K., Okumura, N., Lockett, L. T., Evans, D. H., Glass, R. S., and Lichtenberger, D. L. (2008). Hydrogen Generation from Weak Acids: Electrochemical and Computational Studies in the [(η^5 -C₅H₅)Fe(CO)₂]₂ System. **Organometallics** 27: 4671-4679.
- Fontecilla-Camps, J. C., Volbeda, A., Cavazza, C., and Nicolet, Y. (2007). Structure/Function Relationships of [NiFe]- and [FeFe]-Hydrogenases. **Chem. Rev.** 107: 4273-4303.
- Frey, M., (2002). Hydrogenases: Hydrogen-Activating Enzymes. **Chem. Bio. Chem.** 3: 153-160.
- Georgakaki, I. P., Miller, M. L., and Darensbourg, M. Y. (2003). Requirements for Functional Models of the Iron Hydrogenase Active Site: D₂/H₂O Exchange Activity in $\{(\mu\text{-SMe})(\mu\text{-pdt})[\text{Fe}(\text{CO})_2(\text{PMe}_3)]^{2+}\}[\text{BF}_4^-]$. **Inorg. Chem.** 42: 2489-2494.

- Georgakaki, I. P., Thomson, L. M., Lyon, E. J., Hall, M. B., and Darensbourg, M. Y. (2003). Fundamental Properties of Small Molecule Models of Fe-Only Hydrogenase: Computations Relative to the Definition of an Entatic State in the Active Site. **Coord. Chem. Rev.** 238–239: 255-266.
- Gordon, A. J. and Ford, R. A. (1972). *The Chemist's Companion*, John Wiley and Sons: New York.
- Gordon, J. C., and Kubas, G. J. (2010). Perspectives on How Nature Employs the Principles of Organometallic Chemistry in Dihydrogen Activation in Hydrogenases. **Organometallics** 29: 4682-4701.
- Greco, C., Bruschi, M., De Gioia, L., and Ryde, U. (2007). A QM/MM Investigation of the Activation and Catalytic Mechanism of Fe-Only Hydrogenases. **Inorg. Chem.** 46: 5911-5921.
- Greco, C., Zampella, G., Bertini, L., Bruschi, M., Fantucci, P., and De Gioia, L. (2007). Insights into the Mechanism of Electrocatalytic Hydrogen Evolution Mediated by $\text{Fe}_2(\text{S}_2\text{C}_3\text{H}_6)(\text{CO})_6$: The Simplest Functional Model of the Fe-Hydrogenase Active Site. **Inorg. Chem.** 46: 108-116.
- Gritzner, G. and Kuta, J. (1984). Recommendations on Reporting Electrode Potentials in Nonaqueous Solvents. **Pure Appl. Chem.** 56: 461-466.
- Gruhn, N. E., da Silva Filho, D. A., Bill, T. G., Malagoli, M., Coropceanu, V., Kahn, A., and Bredas, J. (2002). The Vibrational Reorganization Energy in Pentacene: Molecular Influences on Charge Transport. **J. Am. Chem. Soc.** 124: 7918-7919.

- Hatchikian, E. C., Forget, N., Fernandez, V. M., Williams, R., and Cammack, R. (1992). Further characterization of the [Fe]-Hydrogenase from *Desulfovibrio desulfuricans* ATCC 7757. **Eur. J. Biochem.** 209: 357-365.
- Hirohito, T., Ataka, K., Pilak, O., Vogt, S., Stagni, M. S., Meyer-Klaucke, W., Warkentin, E., Thauer, R. K., Shima, S., and Ermler, U. (2009). The Crystal Structure of C176A Mutated [Fe]-Hydrogenase Suggests an Acyl-Iron Ligation in the Active Site Iron Complex. **FEBS Lett.** 583:585-590.
- Herrmann, W. A., Biersack, H., Ziegler, M. L., Weidenhammer, K., Siegel, R., and Rehder, D. (1981). Metal-Carbonyl Syntheses. 9. Carbon Monoxide - A Six-Electron Ligand? Synthesis and Structural Characterization of the Unusual Carbonylniobium Cluster $(\eta^5\text{-C}_5\text{H}_5)_3\text{Nb}_3(\text{CO})_7$. **J. Am. Chem. Soc.** 103: 1692-1699.
- Humphrey, W., Dalke, A. and Schulten, K. (1996). VMD - Visual Molecular Dynamics. **J. Molec. Graph.** 14: 33-38.
- International Energy Agency (2011), CO₂ Emissions from Fuel Combustion Highlights, IEA Information Paper, OECD/IEA, Paris.
- Jain, A., Lense, S., Linehan, J. C., Raugei, S., Cho, H., DuBois, D. L., and Shaw, W. J. (2011). Incorporating Peptides in the Outer-Coordination Sphere of Bioinspired Electrocatalysts for Hydrogen Production. **Inorg. Chem.** 50: 4073-4085.
- Klamt, A. (1995). Conductor-Like Screening Model for Real Solvents: A New Approach to the Quantitative Calculation of Solvation Phenomena. **J. Phy. Chem.** 99: 2224-2235.

- Klamt, A. and Schüürmann, G. (1993). COSMO: A New Approach to Dielectric Screening in Solvents with Explicit Expressions for the Screening Energy and Its Gradient. **J. Chem. Soc.: Perkin Trans. 2**: 799-805.
- Kohn, W. and Sham, L. J. (1965). Self-Consistent Equations Including Exchange and Correlation Effects. **Phy. Rev.** 140: A1133-A1138.
- Krassen, H.; Ott, S.; Heberle, J. (2011). In Vitro Hydrogen Production-Using Energy from the Sun. **Phys. Chem. Chem. Phys.** 13: 47-57.
- Li, H. and Rauchfuss, T. B. (2002). Iron Carbonyl Sulfides, Formaldehyde, and Amines Condense to Give the Proposed Azadithiolate Cofactor of the Fe-Only Hydrogenases. **J. Am. Chem. Soc.** 124: 726-727.
- Lichtenberger, D. L. (2004). A Tutorial on Photoelectron Spectroscopy, (Online) Available: <http://www.chem.arizona.edu/~lichtend/group.dir/presentation/2004Tutorial/index.html>., access on June 2, 2012.
- Lichtenberger, D. L. (2011). A Teaching Materials on Organometallic Compounds (CHEM514), Spring Semester. The University of Arizona.
- Lichtenberger, D. L. and Copenhaver, A. S. (1990). Ionization Band Profile Analysis in Valence Photoelectron Spectroscopy. **J. Electron Spectrosc. Relat. Phenom.** 50: 335-352.
- Lloyd, M. A., Patterson, G. E., Simpson, G. H., Duncan, L. L., King, D. P., Fu, Y., Patrick, B. O., Parkin, S., and Brock, C. P. (2007). Solid-State Compounds of Stereoisomers: *Cis* and *Trans* Isomers of 1,2-Cyclohexanediol and 2,3-Tetralindiol. **Acta Cryst. B** 63: 433-447.

- Lyon, E. J., Georgakaki, I. P., Reibenspies, J. H., and Darensbourg, M. Y. (1999). Carbon Monoxide and Cyanide Ligands in a Classical Organometallic Complex Model for Fe-Only Hydrogenase. **Angew. Chem., Int. Ed.** 38: 3178-3180.
- Lyon, E. J., Georgakaki, I. P., Reibenspies, J. H., and Darensbourg, M. Y. (2001). Coordination Sphere Flexibility of Active-Site Models for Fe-Only Hydrogenase: Studies in Intra- and Intermolecular Diatomic Ligand Exchange. **J. Am. Chem. Soc.** 123: 3268-3278.
- Mejia-Rodriguez, R., Chong, D., Reibenspies, J. H., Soriaga, M. P., and Darensbourg, M. Y. (2004). The Hydrophilic Phosphotriazaadamantane Ligand in the Development of H₂ Production Electrocatalysts: Iron Hydrogenase Model Complexes. **J. Am. Chem. Soc.** 126: 12004-12014.
- Nicolet, Y., de Lacey, A. L., VernÅde, X., Fernandez, V. M., Hatchikian, E. C., and Fontecilla-Camps, J. C. (2001). Crystallographic and FTIR Spectroscopic Evidence of Changes in Fe Coordination Upon Reduction of the Active Site of the Fe-Only Hydrogenase from *Desulfovibrio Desulfuricans*. **J. Am. Chem. Soc.** 123: 1596-1601.
- Nicolet, Y., Cavazza, C., and Fontecilla-Camps, J. C. (2002). Fe-Only Hydrogenases: Structure, Function and Evolution. **J. Inorg. Biochem.** 91: 1-8.
- Ott, S., Borgström, M., Kritikos, M., Lomoth, R., Bergquist, J., Åkermark, B., Hammarström, L., and Sun, L. (2004). Model of the Iron Hydrogenase Active Site Covalently Linked to a Ruthenium Photosensitizer: Synthesis and Photophysical Properties. **Inorg. Chem.** 43: 4683-4692.

- Ott, S., Kritikos, M., Åkermark, B., and Sun, L. (2003). Synthesis and Structure of a Biomimetic Model of the Iron Hydrogenase Active Site Covalently Linked to a Ruthenium Photosensitizer. **Angew. Chem. Int. Ed.** 42: 3285-3288.
- Ott, S., Kritikos, M., Åkermark, B., Sun, L., and Lomoth, R. (2004). A Biomimetic Pathway for Hydrogen Evolution from a Model of the Iron Hydrogenase Active Site. **Angew. Chem., Int. Ed.** 43: 1006-1009.
- Pandey, A. S., Harris, T. V., Giles, L. J., Peters, J. W., and Szilagyi, R. K. (2008). Dithiomethylether as a Ligand in the Hydrogenase H-Cluster. **J. Am. Chem. Soc.** 130: 4533-4540.
- Perdew, J. P., Burke, K., and Ernzerhof, M. (1996). Generalized Gradient Approximation Made Simple. **Phys. Rev. Lett.** 77: 3865- 3868.
- Petro, B. J., Vannucci, A. K., Lockett, L. T., Mebi, C., Kottani, R., Gruhn, N. E., Nichol, G. S., Goodyer, P. A. J., Evans, D. H., Glass, R. S., and Lichtenberger, D. L. (2008). Photoelectron Spectroscopy of Dithiolatodiirohexacarbonyl Models for the Active Site of [Fe-Fe] Hydrogenases: Insight Into the Reorganization Energy of the "Rotated" Structure in the Enzyme. **J. Mol. Struct.** 890: 281-288.
- Portmann, S. and Luthi, H. P. (2000). MOLEKEL: An Interactive Molecular Graphics Tool. **Chimia** 54: 766-769.
- Rajeshwar, K., McConnell, R., and Licht, S. (2008). Solar Hydrogen Generation: Toward a Renewable Energy Future. Springer, New York, USA.
- Rauchfuss, T. B. (2004). Research on Soluble Metal Sulfides: From Polysulfido Complexes to Functional Models for the Hydrogenases. **Inorg. Chem.** 43: 14-26.

- Razavet, M., Davies, S. C., Hughes, D. L., Barclay, J. E., Evans, D. J., Fairhurst, S. A., Liu, X., and Pickett, C. J. (2003). All-Iron Hydrogenase: Synthesis, Structure and Properties of {2Fe3S}-Assemblies Related to the Di-Iron Sub-Site of the H-Cluster. **Dalton Trans.** 586-595.
- Reisner, E., Powell, D. J., Cavazza, C., Fontecilla-Camps, J. C., and Armstrong, F. A. (2009). Visible Light-Driven H₂ Production by Hydrogenases Attached to Dye-Sensitized TiO₂ Nanoparticles. **J. Am. Chem. Soc.** 131: 18457-18466.
- Schwartz, L. (2009). Synthetic [FeFe] Hydrogenase Active Site Model Complexes. Dissertation. Uppsala University, Sweden.
- Schwartz, L., Ekström, J., Lomoth, R., and Ott, S. (2006). Dynamic Ligation at the First Amine-Coordinated Iron Hydrogenase Active Site Mimic. **Chem. Commun.** 4206-4208.
- Schwartz, L., Eriksson, L., Lomoth, R., Teixidor, F., Vinas, C., and Ott, S. (2008). Influence of an Electron-Deficient Bridging O-Carborane on the Properties of an [FeFe] Hydrogenase Active Site Model. **Dalton Trans.** 18: 2379-2381.
- Schwartz, L., Singh, P. S., Eriksson, L., Lomoth, R., and Ott, S. (2008). Tuning the Electronic Properties of Fe₂(μ-areneedithiolate)(CO)_{6-n}(PMe₃)_n (n = 0, 2) Complexes Related to the [Fe-Fe]-Hydrogenase Active Site. **C. R. Chim.** 11: 875-889.
- Scientific Computing and Modelling (SCM) (2010). ADF2010.02 Theoretical Chemistry, Vrije Universiteit, Amsterdam, The Netherlands. (Online) Available: <http://www.scm.com>.
- Scintag Inc. (1999). Chapter 7: Basic of X-ray Diffraction, (Online) Available: <http://epswww.unm.edu/xrd/xrdbasics.pdf>, access on March 23, 2013.

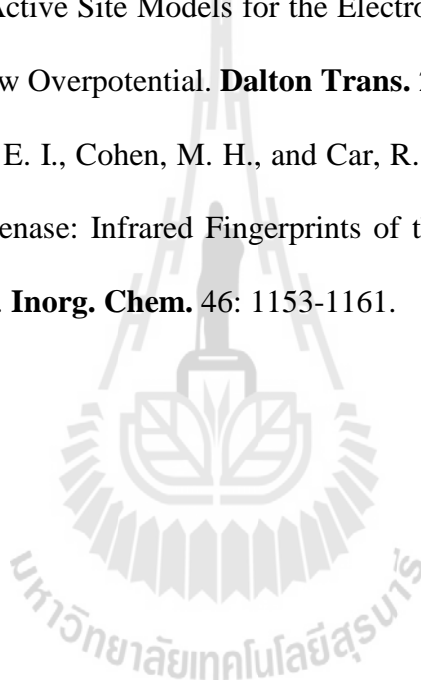
- Seyferth, D., Henderson, R. S., and Song, L. C. (1982). Chemistry of μ -Dithiobis(tricarbonyliron), a Mimic of Inorganic Disulfides. 1. Formation of Di- μ -Thiolato Bis(tricarbonyliron) Dianion. **Organometallics** 1: 125-133.
- Seyferth, D., Henderson, R. S., Song, L. C., and Womack, G. B. (1985). Chemistry of μ -Dithiobis(tricarbonyliron), An Inorganic Mimic of Organic Disulfides : II. Nucleophilic S...S Bond Cleavage by Organolithium and Organomagnesium Reagents. **J. Organomet. Chem.** 292: 9-17.
- Sheldrick, G. (2008). A Short Story of SHELX. **Acta Cryst. A** 64: 112-122.
- Shima, S., Pilak, O., Vogt, S., Schick, M., Stagni, M. S., Meyer-Klaucke, W., Warkentin, E., Thauer, R. K., and Ermler, U. (2008). The Crystal Structure of [Fe]-Hydrogenase Reveals the Geometry of the Active Site. **Science** 321: 572-575.
- Shriver, D. F. and Drezdson, M.A. (1986). The Manipulation of Air-Sensitive Compounds, 2nd edition. A Wiley-Interscience publication. USA.
- Si, Y. T., Hu, M. Q., and Chen, C. N. (2008). Diiron Models for Active Site of FeFe-Hydrogenase with Aromatic Thiolate Bridges: Structures and Electrochemistry. **C. R. Chimie** 11: 932-937.
- Solomon, E. I., Basumallick, L., Chen, P., and Kennepohl, P. (2005). Variable Energy Photoelectron Spectroscopy: Electronic Structure and Electronic Relaxation. **Coord. Chem. Rev.** 249: 229-253.
- Stephens, I. E. L. and Chorkendorff, I. (2011). Minimizing the Use of Platinum in Hydrogen-Evolving Electrodes. **Angew. Chem. Int. Ed.** 50: 1476-1477.

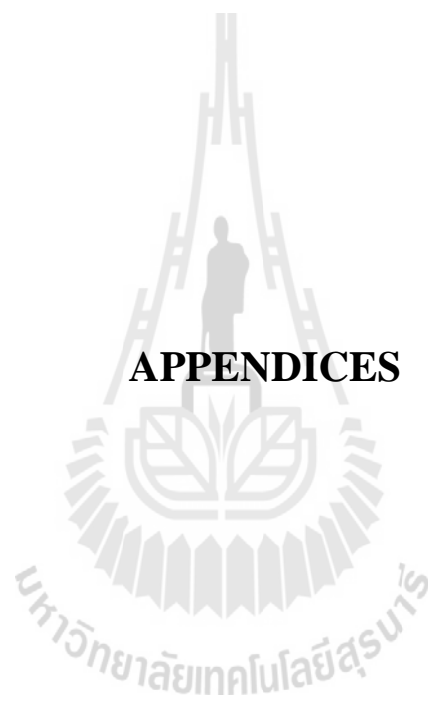
- Stephenson, M. and Stickland, L. H. (1931). Hydrogenase: A Bacterial Enzyme Activating Molecular Hydrogen: The Properties of the Enzyme. **Biochem. J.** 25: 205-214.
- Stoll, H., Pavlidou, C., and Preuß, H. (1978). Theoretical Chemistry Accounts: Theory, Computation, and Modeling. **Theor. Chim. Acta.** 49: 143-149.
- Song, L.-C., Yang, Z.-Y., Bian, H.-Z., and Hu, Q.-M. (2004). Novel Single and Double Diiron Oxadithiolates as Models for the Active Site of [Fe]-Only Hydrogenases **Organometallics** 23: 3082-3084.
- Song, L.-C., Cheng, J., Yan, J., Wang, H.-T., Liu, X.-F., and Hu, Q.-M. (2006). Two Novel Bridgehead-C-Substituted Diiron Propanedithiolate Complexes as Active Site Models for Fe-Only Hydrogenases. **Organometallics** 25: 1544-1547.
- Song, L.-C., Li, C. G., Ge, J. H., Yang, Z. Y., Wang, H. T., Zhang, J., and Hu, Q. M. (2008). Synthesis and Structural Characterization of the Mono- and Diphosphine-Containing Diiron Propanedithiolate Complexes Related to [FeFe]-Hydrogenases. Biomimetic H₂ Evolution Catalyzed by [(μ -PDT)Fe₂(CO)₄][(Ph₂P)₂N(n-Pr)]. **J. Inorg. Biochem.** 102: 1973-1979.
- Song, L.-C., Yang, Z.-Y., Hua, Y.-J., Wang, H.-T., Liu, Y., and Hu, Q.-M. (2007). Diiron Thiadithiolates as Active Site Models for the Iron-Only Hydrogenases: Synthesis, Structures, and Catalytic H₂ Production. **Organometallics** 26: 2106-2110.

- Song, L., Yin, B., Li, Y., Zhao, L., Ge, J., Yang, Z., and Hu, Q. (2007). Synthesis, Structural Characterization, and Some Properties of New N-Functionally Substituted Diiron Azadithiolate Complexes as Biomimetic Models of Iron-Only Hydrogenases. **Organometallics** 26: 4921-4929.
- Stoll, H., Pavlidou, C., and Preuß, H. (1978). Theoretical Chemistry Accounts: Theory, Computation, and Modeling. **Theor. Chim. Acta.** 49: 143-149.
- Swart, M., Ehlers A.W., and Lammertsma, K. (2004). Performance of the OPBE Exchange-Correlation Functional. **Mol. Phys.** 102: 2467- 2474.
- Tard, C., Liu, X. M., Ibrahim, S. K., Bruschi, M., De Gioia, L., Davies, S. C., Yang, X., Wang, L. S., Sawers, G., and Pickett, C. J. (2005). Synthesis of the H-Cluster Framework of Iron-Only Hydrogenase. **Nature** 433: 610-613.
- Te Velde, G. Bickelhaupt, F. M., Baerends, E. J., Guerra, C. F., Van Gisbergen, S. J. A., Snijders, J. G., and Ziegler, T. (2001). Chemistry with ADF. **J. Comput. Chem.** 22: 931-967.
- Teo, B. K., Hall, M. B., Fenske, R. F., and Dahl, L. F. (1975). Nonparameterized Molecular Orbital Calculations of Ligand-Bridge $\text{Fe}_2(\text{CO})_6\text{X}_2$ -type Dimers Containing Metal-Metal Interactions. **Inorg. Chem.** 14: 3103-3117.
- Theoretical and Computational Biophysics Group, NIH Center for Macromolecular Modeling and Bioinformatics. The CpI hydrogenase image. The University of Illinois at Urbana-Champaign. (Online) Available:
<http://www.ks.uiuc.edu/Research/hydrogenase/>, access on August 10, 2012.

- Tye, J. W., Darensbourg, M. Y., and Hall, M. B. (2006). Correlation between Computed Gas-Phase and Experimentally Determined Solution-Phase Infrared Spectra: Models of the Iron-Iron Hydrogenase Enzyme Active Site. **J. Comput. Chem.** 27: 1454-1462.
- Tye, J. W., Darensbourg, M. Y., and Hall, M. B. (2006). De Novo Design of Synthetic Di-Iron(I) Complexes as Structural Models of the Reduced Form of Iron-Iron Hydrogenase. **Inorg. Chem.** 45: 1552-1559.
- Yu, Z., Wang, M., Li, P., Dong, W., Wang, F., and Sun, L. (2008) Diiron Dithiolate Complexes Containing Intra-ligand NH...S hydrogen bonds: [FeFe] Hydrogenase Active Site Models for the Electrochemical Proton Reduction of HOAc with Low Overpotential. **Dalton Trans.** 2400-2406.
- Van Lenthe, E., and Baerends, E.J. (2003). Optimized Slater-Type Basis Sets for the Elements 1–118. **J. Com. Chem.** 24: 1142-1156.
- Vignais, P. M., Billoud, B., and Meyer, J. (2001). Classification and Phylogeny of Hydrogenases. **FEMS Microbiol. Rev.** 25: 455-501.
- Vincent, K. A., Parkin, A., and Armstrong, F. A. (2007). Investigating and Exploiting the Electrocatalytic Properties of Hydrogenases. **Chem. Rev.** 107: 4366-4413.
- Vosko, S. H., Wilk, L., and Nusair, M. (1980). Accurate Spin-Dependent Electron Liquid Correlation Energies for Local Spin Density Calculations: a Critical Analysis. **Can. J. Phys.** 58: 1200-1211.
- Wei, Y., Chan, C. C., Tian, J., Jang, G. W., and Hsueh, K. F. (1991). Electrochemical Polymerization of Thiophenes in the Presence of Bithiophene or Terthiophene: Kinetics and Mechanism of the Polymerization. **Chem. Mater.** 3: 888-897.

- Wright, R. J., Zhang, W., Yang, X., Fasulo, M., and Tilley, T. D., (2012). Isolation, Observation, and Computational Modeling of Proposed Intermediates in Catalytic Proton Reductions with the Hydrogenase Mimic $\text{Fe}_2(\text{CO})_6\text{S}_2\text{C}_6\text{H}_4$. **Dalton Trans.** 73-82.
- Yu, Z., Wang, M., Li, P., Dong, W., Wang, F., and Sun, L. (2008). Diiron Dithiolate Complexes Containing Intra-Ligand $\text{NH}\cdots\text{S}$ Hydrogen Bonds: [FeFe] Hydrogenase Active Site Models for the Electrochemical Proton Reduction of HOAc with Low Overpotential. **Dalton Trans.** 2400-2406.
- Zilberman, S., Stiefel, E. I., Cohen, M. H., and Car, R. (2007). Theoretical Studies of [FeFe]-Hydrogenase: Infrared Fingerprints of the Dithiol-Bridging Ligand in the Active Site. **Inorg. Chem.** 46: 1153-1161.





APPENDICES

APPENDIX A

SUPPORTING INFORMATION FOR CHAPTER III

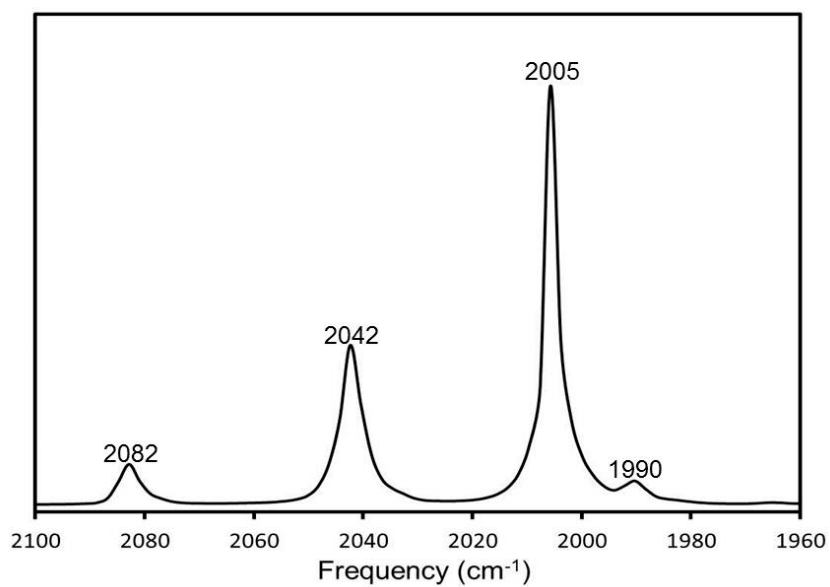


Figure A.1 IR spectrum in carbonyl stretching region of $[(\mu\text{-S})_2\text{Fe}_2(\text{CO})_6]$ in hexane.

A.1 Typical ADF 2010.02 input file

```
xc
lda vwn stoll
!gga opbe
end

basis
type TZP
!core none
end

charge 0 0

!unrestricted

relativistic ZORA

!symmetry nosym
!symmetry C(S)

integration=6.0

SCF
iterations 500
converge 1e-6 1e-3
end

geometry
branch old
iterations 200
converge E=0.0005
converge grad=0.001
converge Rad=0.001
converge Angle=0.1
end

analyticalfreq
end

!solvation
!solve name=acetonitrile
!charged conv=1e-10 iter=1000
!end

File xyz trajectory.xyz

atoms cartesion
C      -2.283800      -1.162200      0.000000
O       -1.168400      -1.162200      0.000000
End

End input
eor
```



APPENDIX B

SUPPORTING INFORMATION FOR CHAPTER IV

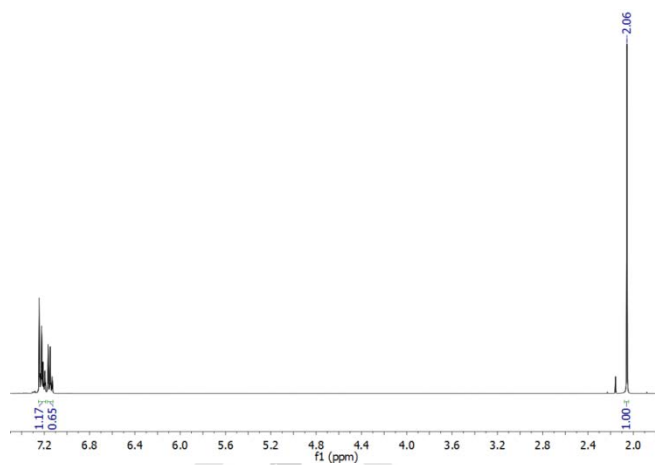


Figure B.1 ¹H-NMR spectrum of **1** in CDCl₃ solution.

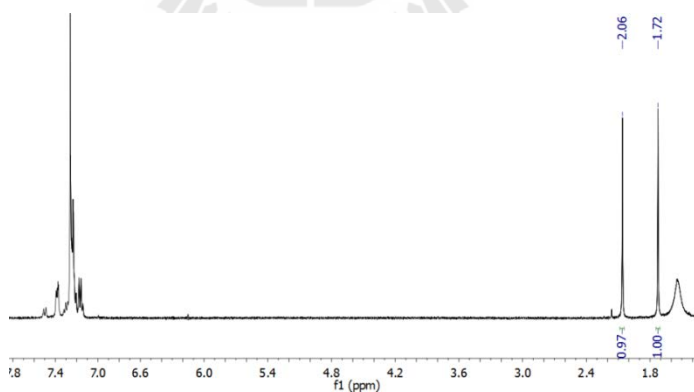


Figure B.2 ¹H-NMR spectrum of $[(\mu\text{-SMe})(\mu\text{-SPh})\text{Fe}_2(\text{CO})_6]$ in CDCl₃ solution prepared from the mixed *anti*-isomer crystals.

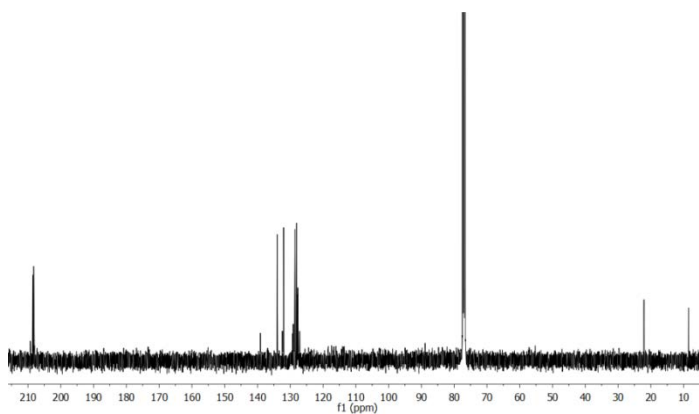


Figure B.3 ^{13}C -NMR spectrum of $[(\mu\text{-SMe})(\mu\text{-SPh})\text{Fe}_2(\text{CO})_6]$ in CDCl_3 solution prepared from the mixed *anti*-isomer crystals.

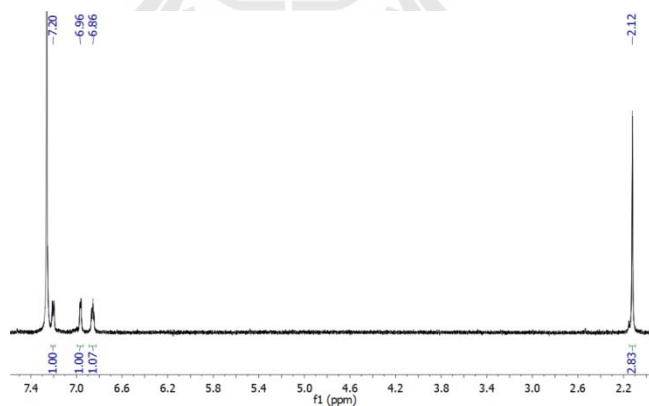


Figure B.4 ^1H -NMR spectrum of **2** in CDCl_3 solution.

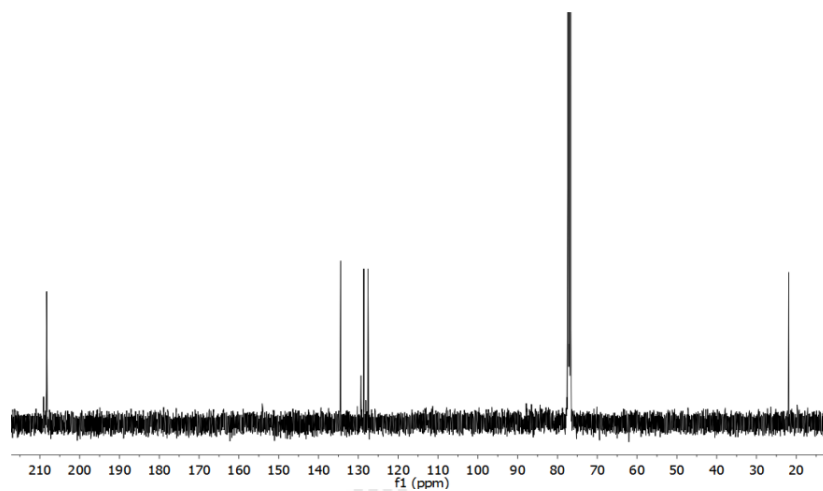


Figure B.5 ^{13}C -NMR spectrum of **2** in CDCl_3 solution.

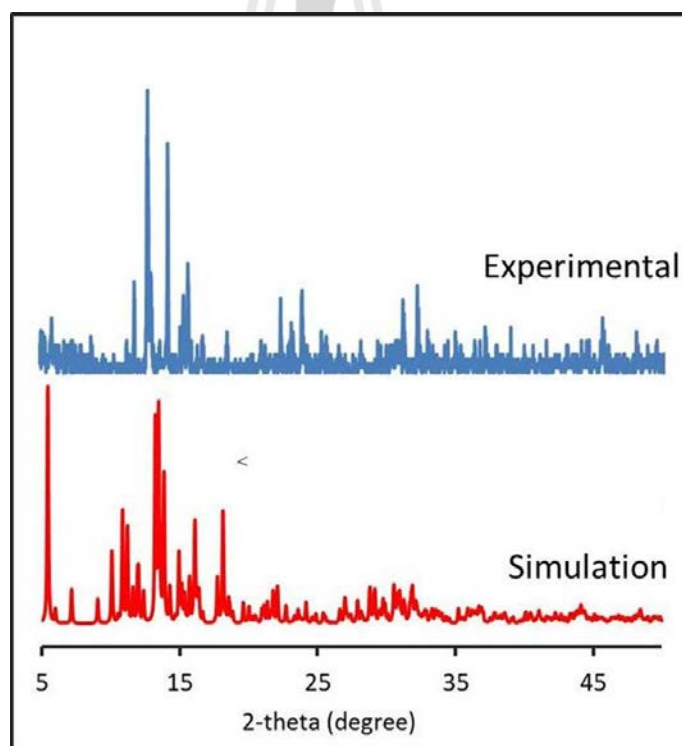


Figure B.6 Comparison of the experimental XRD pattern of bulk sample **1** with the simulated XRD pattern from mixed *anti*-isomer crystal data.

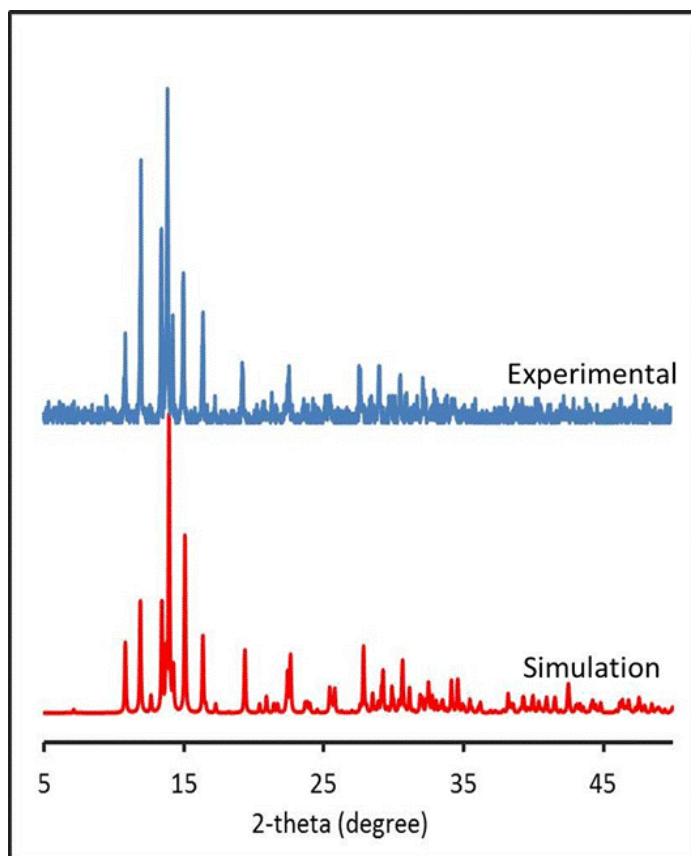


Figure B.7 Comparison of the experimental and simulated XRD pattern of **2**.

Table B.1 Comparison of selected bond lengths and angles of crystallographically independent **A** and **B** of $[(\mu\text{-SMe})(\mu\text{-SPh})\text{Fe}_2(\text{CO})_6]$ to DFT structures.

Bond (Å)/Angle (°)	A	Bond (Å)/Angle (°)	B	DFT
Fe(1)–Fe(2)	2.512	Fe(3)–Fe(4)	2.511	2.514
Fe(1)–S(1)	2.249	Fe(3)–S(3)	2.247	2.272
Fe(1)–S(2)	2.267	Fe(3)–S(4)	2.264	2.288
S(1)⋯S(2)	2.906	S(3)⋯S(4)	2.910	2.901
S(1)–C(7)	1.817	S(3)–C(20)	1.821	1.825
S(2)–C(8)	1.802	S(4)–C(21)	1.799	1.799
Fe–C ^{av}	1.793	Fe–C ^{av}	1.795	1.776
C–O ^{av}	1.141	C–O ^{av}	1.138	1.158
S(1)–Fe(1)–S(2)	80.12	S(3)–Fe(3)–S(4)	80.36	79.00
Fe(1)–S(1)–Fe(2)	67.82	Fe(3)–S(3)–Fe(4)	67.89	67.18
Fe(1)–S(2)–Fe(2)	67.18	Fe(3)–S(4)–Fe(4)	67.18	66.68
S(1)–Fe(1)–C(1)	99.92	S(3)–Fe(3)–C(14)	101.01	102.06
S(2)–Fe(1)–C(1)	107.15	S(4)–Fe(3)–C(14)	106.07	103.68
C(1)–Fe(1)–C(2)	98.44	C(14)–Fe(3)–C(15)	97.84	99.93
C(1)–Fe(1)–C(3)	99.81	C(14)–Fe(3)–C(16)	100.23	99.07
C(2)–Fe(1)–C(3)	92.18	C(15)–Fe(3)–C(16)	92.85	92.18
S(1)⋯S(2)–C(8)	78.57	S(3)⋯S(4)–C(21)	79.76	75.31
S(2)⋯S(1)–C(7)	160.52	S(4)⋯S(3)–C(20)	160.35	159.34

^{av} Averaged over all COs

Table B.2 Comparison of selected bond lengths and angles of crystallographically independent **C** and **D** of $[(\mu\text{-SMe})(\mu\text{-SPh})\text{Fe}_2(\text{CO})_6]$ to DFT structures.

Bond (Å)/Angle (°)	C	Bond (Å)/Angle (°)	D	DFT
Fe(5)–Fe(6)	2.514	Fe(7)–Fe(8)	2.517	2.513
Fe(5)–S(5)	2.255	Fe(7)–S(7)	2.258	2.281
Fe(5)–S(6)	2.262	Fe(7)–S(8)	2.264	2.273
S(5)⋯S(6)	2.900	S(7)⋯S(8)	2.902	2.932
S(5)–C(33)	1.818	S(7)–C(46)	1.819	1.823
S(6)–C(34)	1.787	S(8)–C(47)	1.783	1.789
Fe–C ^{av}	1.795	Fe–C ^{av}	1.798	1.779
C–O ^{av}	1.138	C–O ^{av}	1.138	1.157
S(5)–Fe(5)–S(6)	79.90	S(7)–Fe(7)–S(8)	79.85	80.15
Fe(5)–S(5)–Fe(6)	67.61	Fe(7)–S(7)–Fe(8)	67.88	66.82
Fe(5)–S(6)–Fe(6)	67.57	Fe(7)–S(8)–Fe(8)	67.66	67.13
S(5)–Fe(5)–C(27)	100.91	S(7)–Fe(7)–C(40)	104.19	103.07
S(6)–Fe(5)–C(27)	102.76	S(8)–Fe(7)–C(40)	101.36	102.38
C(27)–Fe(5)–C(28)	100.30	C(40)–Fe(7)–C(41)	99.86	100.41
C(27)–Fe(5)–C(29)	100.04	C(40)–Fe(7)–C(42)	98.66	99.40
C(28)–Fe(5)–C(29)	90.51	C(41)–Fe(7)–C(42)	91.77	90.76
S(5)⋯S(6)–C(34)	162.95	S(7)⋯S(8)–C(47)	162.23	159.98
S(6)⋯S(5)–C(33)	78.89	S(8)⋯S(7)–C(46)	79.52	77.67

^{av} Averaged over all COs

Table B.3 Comparison of selected bond lengths and angles of $[(\mu\text{-SMe})(\mu\text{-STh})\text{Fe}_2(\text{CO})_6]$ to DFT structure.

Bond (Å)/Angle (°)	X-ray	DFT ^b
Fe(1)–Fe(2)	2.521	2.511
Fe(1)–S(1)	2.253	2.272
Fe(1)–S(2)	2.274	2.290
S(1)⋯S(2)	2.906	2.913
S(1)–C(7)	1.819	1.825
S(2)–C(8)	1.722	1.771
Fe–C ^{av}	1.801	1.777
C–O ^{av}	1.137	1.158
S(1)–Fe(1)–S(2)	79.88	79.35
Fe(1)–S(1)–Fe(2)	67.91	67.09
Fe(1)–S(2)–Fe(2)	67.36	66.48
S(1)–Fe(1)–C(1)	104.42	102.96
S(2)–Fe(1)–C(1)	102.87	104.05
C(1)–Fe(1)–C(2)	98.88	99.85
C(1)–Fe(1)–C(3)	98.01	98.68
C(2)–Fe(1)–C(3)	91.5	91.8
S(1)⋯S(2)–C(8)	76.45	74.12
S(2)⋯S(1)–C(7)	159.35	159.23

^{av} Averaged over all COs

Table B.4 Bond lengths (Å) and angles (°) for $[(\mu\text{-SMe})(\mu\text{-SPh})\text{Fe}_2(\text{CO})_6]$.

Fe(2)-C(6)	1.779(3)	Fe(5)-C(29)	1.795(3)
Fe(2)-C(5)	1.799(3)	Fe(5)-C(27)	1.797(3)
Fe(2)-C(4)	1.806(3)	Fe(5)-S(5)	2.2548(8)
Fe(2)-S(1)	2.2532(8)	Fe(5)-S(6)	2.2619(8)
Fe(2)-S(2)	2.2727(8)	Fe(7)-C(42)	1.794(3)
Fe(2)-Fe(1)	2.5116(6)	Fe(7)-C(41)	1.800(3)
Fe(1)-C(3)	1.783(3)	Fe(7)-C(40)	1.802(3)
Fe(1)-C(1)	1.794(3)	Fe(7)-S(7)	2.2576(9)
Fe(1)-C(2)	1.799(3)	Fe(7)-S(8)	2.2637(8)
Fe(1)-S(1)	2.2488(8)	S(8)-C(47)	1.783(3)
Fe(1)-S(2)	2.2671(8)	S(6)-C(34)	1.788(3)
Fe(3)-C(16)	1.788(3)	S(5)-C(33)	1.817(3)
Fe(3)-C(14)	1.796(3)	S(7)-C(46)	1.820(3)
Fe(3)-C(15)	1.805(3)	O(42)-C(42)	1.145(3)
Fe(3)-S(3)	2.2470(8)	O(43)-C(43)	1.135(3)
Fe(3)-S(4)	2.2639(8)	O(40)-C(40)	1.139(3)
Fe(3)-Fe(4)	2.5111(6)	O(41)-C(41)	1.135(3)
Fe(4)-C(19)	1.779(3)	O(28)-C(28)	1.139(3)
Fe(4)-C(18)	1.794(3)	O(27)-C(27)	1.140(3)
Fe(4)-C(17)	1.807(3)	O(32)-C(32)	1.129(3)
Fe(4)-S(3)	2.2501(8)	O(31)-C(31)	1.136(3)
Fe(4)-S(4)	2.2750(8)	O(29)-C(29)	1.140(3)
S(4)-C(21)	1.799(3)	O(30)-C(30)	1.145(3)
S(2)-C(8)	1.802(3)	O(1)-C(1)	1.143(3)
S(1)-C(7)	1.818(3)	O(2)-C(2)	1.144(3)
S(3)-C(20)	1.821(3)	O(4)-C(4)	1.138(3)
Fe(6)-C(31)	1.795(3)	O(5)-C(5)	1.138(3)
Fe(6)-C(30)	1.796(3)	O(6)-C(6)	1.139(3)
Fe(6)-C(32)	1.801(3)	O(3)-C(3)	1.144(3)
Fe(6)-S(6)	2.2586(8)	O(14)-C(14)	1.139(3)
Fe(6)-S(5)	2.2628(8)	CO12-C(19)	1.143(3)
Fe(6)-Fe(5)	2.5135(6)	O(18)-C(18)	1.139(3)
Fe(8)-C(44)	1.789(3)	O(15)-C(15)	1.129(3)
Fe(8)-C(45)	1.796(3)	O(16)-C(16)	1.141(3)
Fe(8)-C(43)	1.807(3)	O(17)-C(17)	1.136(3)
Fe(8)-S(7)	2.2512(8)	C(21)-C(26)	1.379(4)
Fe(8)-S(8)	2.2581(8)	C(21)-C(22)	1.380(4)
Fe(8)-Fe(7)	2.5173(6)	C(22)-C(23)	1.385(4)

Table B.4 (Continued).

Fe(5)-C(28)	1.789(3)	C(25)-C(24)	1.370(5)
C(25)-C(26)	1.381(4)	C(3)-Fe(1)-C(1)	99.80(12)
C(24)-C(23)	1.379(5)	C(3)-Fe(1)-C(2)	92.18(13)
C(34)-C(39)	1.375(4)	C(1)-Fe(1)-C(2)	98.47(13)
C(34)-C(35)	1.376(4)	C(3)-Fe(1)-S(1)	92.71(10)
C(39)-C(38)	1.384(4)	C(1)-Fe(1)-S(1)	99.92(9)
C(35)-C(36)	1.388(4)	C(2)-Fe(1)-S(1)	159.87(9)
C(36)-C(37)	1.369(4)	C(3)-Fe(1)-S(2)	152.89(10)
C(38)-C(37)	1.366(4)	C(1)-Fe(1)-S(2)	107.16(9)
C(9)-C(8)	1.375(4)	C(2)-Fe(1)-S(2)	86.69(9)
C(9)-C(10)	1.392(4)	S(1)-Fe(1)-S(2)	80.12(3)
C(8)-C(13)	1.383(4)	C(3)-Fe(1)-Fe(2)	97.78(9)
C(12)-C(11)	1.375(4)	C(1)-Fe(1)-Fe(2)	150.95(9)
C(12)-C(13)	1.384(4)	C(2)-Fe(1)-Fe(2)	103.80(9)
C(11)-C(10)	1.374(4)	S(1)-Fe(1)-Fe(2)	56.17(2)
C(47)-C(52)	1.375(4)	S(2)-Fe(1)-Fe(2)	56.52(2)
C(47)-C(48)	1.382(4)	C(16)-Fe(3)-C(14)	100.22(13)
C(51)-C(50)	1.378(4)	C(16)-Fe(3)-C(15)	92.85(13)
C(51)-C(52)	1.385(4)	C(14)-Fe(3)-C(15)	97.85(13)
C(44)-O(44)	1.136(3)	C(16)-Fe(3)-S(3)	92.74(10)
C(48)-C(49)	1.375(4)	C(14)-Fe(3)-S(3)	101.01(9)
C(45)-O(45)	1.141(3)	C(15)-Fe(3)-S(3)	159.04(10)
C(16)-Fe(3)-S(4)	153.63(10)	C(14)-Fe(3)-S(4)	106.07(8)
C(50)-C(49)	1.371(4)	C(15)-Fe(3)-S(4)	85.71(9)
C(6)-Fe(2)-C(5)	90.36(12)	S(3)-Fe(3)-S(4)	80.36(3)
C(6)-Fe(2)-C(4)	99.38(13)	C(16)-Fe(3)-Fe(4)	98.42(9)
C(5)-Fe(2)-C(4)	100.55(13)	C(14)-Fe(3)-Fe(4)	151.13(8)
C(6)-Fe(2)-S(1)	92.11(9)	C(15)-Fe(3)-Fe(4)	103.05(9)
C(5)-Fe(2)-S(1)	157.04(9)	S(3)-Fe(3)-Fe(4)	56.12(2)
C(4)-Fe(2)-S(1)	101.55(10)	S(4)-Fe(3)-Fe(4)	56.62(2)
C(6)-Fe(2)-S(2)	158.00(10)	C(19)-Fe(4)-C(18)	90.14(13)
C(5)-Fe(2)-S(2)	89.41(9)	C(19)-Fe(4)-C(17)	99.54(14)
C(4)-Fe(2)-S(2)	102.28(9)	C(18)-Fe(4)-C(17)	100.58(14)
S(1)-Fe(2)-S(2)	79.91(3)	C(19)-Fe(4)-S(3)	92.27(10)
C(6)-Fe(2)-Fe(1)	102.27(9)	C(18)-Fe(4)-S(3)	156.80(10)
C(5)-Fe(2)-Fe(1)	101.20(9)	C(17)-Fe(4)-S(3)	101.76(10)
C(4)-Fe(2)-Fe(1)	149.02(10)	C(19)-Fe(4)-S(4)	158.21(10)
S(1)-Fe(2)-Fe(1)	56.01(2)	C(18)-Fe(4)-S(4)	89.28(9)
S(2)-Fe(2)-Fe(1)	56.30(2)		

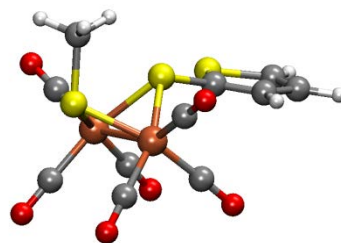
Table B.5 Bond lengths (Å) and angles (°) for $[(\mu\text{-SMe})(\mu\text{-STh})\text{Fe}_2(\text{CO})_6]$.

Fe(1)-C(3)	1.7867(16)	S(1)-Fe(1)-Fe(2)	56.186(11)
Fe(1)-C(2)	1.8068(15)	S(1)-Fe(1)-Fe(2)	56.186(11)
Fe(1)-C(1)	1.8107(16)	S(2)-Fe(1)-Fe(2)	56.314(11)
Fe(1)-S(1)	2.2533(4)	C(6)-Fe(2)-C(5)	90.81(7)
Fe(1)-S(2)	2.2737(4)	C(6)-Fe(2)-C(4)	97.05(8)
Fe(1)-Fe(2)	2.5215(3)	C(5)-Fe(2)-C(4)	98.49(7)
Fe(2)-C(6)	1.7938(17)	C(6)-Fe(2)-S(1)	92.75(5)
Fe(2)-C(5)	1.8016(16)	C(5)-Fe(2)-S(1)	154.67(5)
Fe(2)-C(4)	1.8065(17)	C(4)-Fe(2)-S(1)	105.93(5)
Fe(2)-S(1)	2.2609(4)	C(6)-Fe(2)-S(2)	162.33(6)
Fe(2)-S(2)	2.2733(4)	C(5)-Fe(2)-S(2)	89.49(5)
S(1)-C(7)	1.8188(16)	C(4)-Fe(2)-S(2)	100.38(5)
S(2)-C(8)	1.7721(15)	S(1)-Fe(2)-S(2)	79.732(15)
S(3)-C(11)	1.7223(19)	C(6)-Fe(2)-Fe(1)	106.24(6)
S(3)-C(8)	1.7231(15)	C(5)-Fe(2)-Fe(1)	99.09(5)
O(1)-C(1)	1.139(2)	C(4)-Fe(2)-Fe(1)	150.45(5)
O(2)-C(2)	1.135(2)	S(1)-Fe(2)-Fe(1)	55.900(12)
O(3)-C(3)	1.141(2)	S(2)-Fe(2)-Fe(1)	56.327(11)
C(4)-O(4)	1.138(2)	C(7)-S(1)-Fe(1)	114.33(6)
O(5)-C(5)	1.134(2)	C(7)-S(1)-Fe(2)	114.14(6)
C(6)-O(6)	1.136(2)	Fe(1)-S(1)-Fe(2)	67.914(13)
C(8)-C(9)	1.364(2)	C(8)-S(2)-Fe(2)	109.85(5)
C(9)-C(10)	1.424(2)	C(8)-S(2)-Fe(1)	112.34(5)
C(10)-C(11)	1.339(3)	Fe(2)-S(2)-Fe(1)	67.359(12)
C(3)-Fe(1)-C(2)	91.49(7)	C(11)-S(3)-C(8)	91.61(8)
C(3)-Fe(1)-C(1)	98.01(7)	O(1)-C(1)-Fe(1)	177.91(16)
C(2)-Fe(1)-C(1)	98.89(7)	O(2)-C(2)-Fe(1)	178.71(14)
C(3)-Fe(1)-S(1)	91.96(5)	O(3)-C(3)-Fe(1)	178.72(15)
C(2)-Fe(1)-S(1)	155.70(5)	O(4)-C(4)-Fe(2)	177.42(16)
C(1)-Fe(1)-S(1)	104.42(5)	O(5)-C(5)-Fe(2)	178.64(14)
C(3)-Fe(1)-S(2)	158.87(5)	O(6)-C(6)-Fe(2)	178.59(18)
C(2)-Fe(1)-S(2)	88.42(5)	C(9)-C(8)-S(3)	111.04(12)
C(1)-Fe(1)-S(2)	102.88(5)	C(9)-C(8)-S(2)	127.52(12)
S(1)-Fe(1)-S(2)	79.884(15)	S(3)-C(8)-S(2)	121.12(9)
C(3)-Fe(1)-Fe(2)	102.99(5)	C(8)-C(9)-C(10)	112.48(15)
C(2)-Fe(1)-Fe(2)	99.64(5)	C(11)-C(10)-C(9)	113.06(16)
C(1)-Fe(1)-Fe(2)	151.47(5)	C(10)-C(11)-S(3)	111.81(13)
C(1)-Fe(1)-Fe(2)	151.47(5)		

B.6 Optimized geometry (cartesian coordinates in Å).

[(μ -SMe)(μ -STh)Fe₂(CO)₆], Me a/Th e isomer

Fe	-1.321789	-0.537723	-0.640513
Fe	0.655343	-1.332714	0.687744
S	0.797410	-0.664243	-1.498875
S	-0.192346	0.769939	0.834954
O	-2.001997	-3.018613	-2.059608
O	-2.708785	1.401433	-2.358193
O	0.824435	-4.133347	-0.186896
O	-3.450675	-0.973680	1.317776
O	3.394005	-0.935470	1.667788
O	-0.679948	-2.091687	3.179245
C	-1.722223	-2.037537	-1.515944
C	-2.140589	0.652438	-1.683966
C	0.765753	-3.026663	0.142009
C	-2.619232	-0.804828	0.528350
C	2.312425	-1.088371	1.282983
C	-0.139304	-1.805153	2.195207
C	-1.103157	1.084865	2.384702
H	-1.702280	0.224560	2.737414
H	-0.352269	1.360169	3.152113
H	-1.765354	1.954379	2.200360
C	1.534026	0.945056	-1.570600
C	2.805420	1.291692	-1.166503
C	3.150420	2.614103	-1.534231
C	2.145725	3.256418	-2.217000
S	0.762530	2.249862	-2.412446
H	3.463681	0.605486	-0.612385
H	4.114683	3.085007	-1.294804
H	2.132621	4.281247	-2.609867

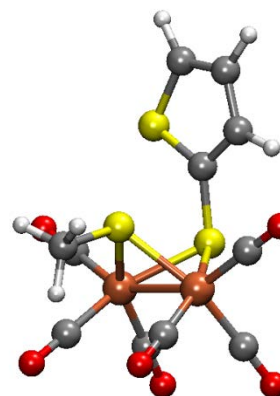


วิทยาลัยเทคโนโลยีสุรนารี

B.6 (Continued).

[(μ -SMe)(μ -STh)Fe₂(CO)₆], Me e/Th a isomer

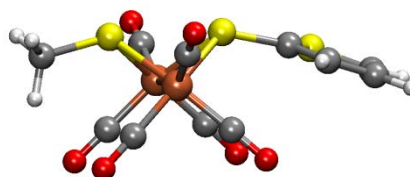
Fe	-1.321729	-0.537730	-0.640572
Fe	0.655347	-1.332685	0.687782
S	0.797498	-0.664271	-1.498850
S	-0.192359	0.769953	0.834936
O	-2.002078	-3.018424	-2.059937
O	-2.708938	1.401386	-2.358165
O	0.824118	-4.133392	-0.186655
O	-3.450401	-0.973872	1.317892
O	3.394071	-0.935541	1.667580
O	-0.679862	-2.091527	3.179377
C	-1.722241	-2.037415	-1.516164
C	-2.140615	0.652435	-1.683972
C	0.765587	-3.026655	0.142116
C	-2.619093	-0.804962	0.528342
C	2.312475	-1.088380	1.282888
C	-0.139262	-1.805049	2.195324
C	-1.103366	1.084860	2.384567
H	-1.702368	0.224445	2.737259
H	-0.352633	1.360393	3.152044
H	-1.765726	1.954231	2.200068
C	1.534086	0.945046	-1.570558
C	2.805478	1.291709	-1.166487
C	3.150402	2.614123	-1.534186
C	2.145634	3.256446	-2.216852
S	0.762501	2.249789	-2.412389
H	3.463829	0.605505	-0.612465
H	4.114684	3.085013	-1.294865
H	2.132436	4.281215	-2.609864



B.6 (Continued).

[(μ -SMe)(μ -STh)Fe₂(CO)₆], Me e/Th e isomer

Fe	-1.337272	-0.580181	-0.640261
Fe	0.654114	-1.359438	0.659130
S	0.797072	-0.573471	-1.492334
S	-0.131337	0.786907	0.733504
O	-2.073323	-3.152085	-1.845725
O	-2.701691	1.284956	-2.459122
O	0.642722	-4.196871	-0.083556
O	-3.444249	-0.855889	1.369226
O	3.418859	-1.096384	1.627988
O	-0.661226	-1.981181	3.194646
C	-1.768053	-2.133653	-1.392208
C	-2.149258	0.560027	-1.747361
C	0.656649	-3.072009	0.183846
C	-2.619773	-0.748696	0.561453
C	2.335248	-1.182544	1.232032
C	-0.128245	-1.744577	2.192836
C	-0.985695	1.199834	2.289544
H	-1.588745	0.365352	2.694787
H	-0.207446	1.495173	3.020960
H	-1.637725	2.071051	2.080299
C	1.088786	-1.846518	-2.678993
C	2.093079	-2.789763	-2.670537
C	2.147900	-3.536063	-3.872586
C	1.195874	-3.149617	-4.783527
S	0.217984	-1.866733	-4.179260
H	2.768446	-2.932965	-1.813529
H	2.867709	-4.345954	-4.058397
H	0.996229	-3.560369	-5.781561

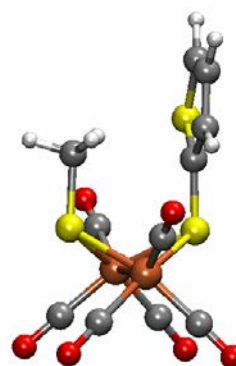


วิทยาลัยเทคโนโลยีสุรนารี

B.6 (Continued).

[[μ -SMe)(μ -STh)Fe₂(CO)₆], Me **a**/Th **a** isomer

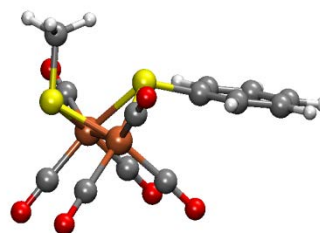
Fe	-1.341748	-0.491038	-0.582175
Fe	0.666627	-1.292247	0.711397
S	0.754107	-0.661078	-1.473602
S	-0.453369	0.632642	1.188532
O	-2.066867	-2.780076	-2.278602
O	-2.592794	1.690581	-2.095736
O	1.093341	-4.046258	-0.229718
O	-3.550921	-1.159971	1.234944
O	3.330371	-0.642788	1.751518
O	-0.604773	-2.340720	3.142932
C	-1.770840	-1.876467	-1.621620
C	-2.097406	0.827575	-1.505106
C	0.931087	-2.959571	0.128113
C	-2.681312	-0.890118	0.523403
C	2.280767	-0.913059	1.340325
C	-0.103525	-1.922143	2.189784
C	0.398361	2.194965	0.782134
H	-0.142161	2.970553	1.361635
H	1.451347	2.139172	1.122025
H	0.368287	2.433240	-0.298526
C	1.584286	0.876507	-1.711782
C	2.821297	1.257534	-1.241646
C	3.245274	2.502823	-1.767329
C	2.336760	3.053070	-2.637474
S	0.951235	2.044224	-2.832397
H	3.400916	0.651610	-0.528860
H	4.201759	2.981708	-1.512296
H	2.404022	3.998863	-3.190590



B.6 (Continued).

[(μ -SMe)(μ -SPh)Fe₂(CO)₆], Me a/Ph e isomer

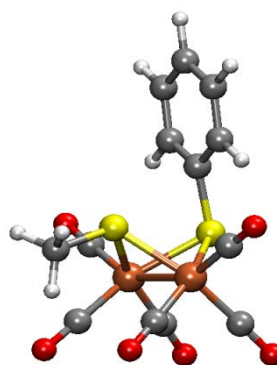
Fe	-1.326539	-0.565666	-0.655362
Fe	0.656869	-1.349680	0.673156
S	0.784974	-0.666476	-1.489764
S	-0.241920	0.739027	0.869068
O	-2.153239	-3.068564	-1.944055
O	-2.624889	1.400956	-2.408244
O	0.639230	-4.206064	0.004905
O	-3.463736	-0.896446	1.328381
O	3.429269	-1.009328	1.581936
O	-0.597062	-1.976299	3.251271
C	-1.815031	-2.078789	-1.451586
C	-2.102746	0.625602	-1.724898
C	0.658837	-3.075498	0.246993
C	-2.618006	-0.756549	0.552637
C	2.339038	-1.139854	1.214726
C	-0.103655	-1.719528	2.237761
C	0.789406	2.015068	0.073857
H	0.127554	2.876357	-0.146395
H	1.559657	2.316467	0.811516
H	1.272105	1.656631	-0.857370
C	1.056965	-1.971765	-2.683051
C	1.630490	-3.833508	-4.675600
C	2.129606	-2.852063	-2.522899
C	0.277258	-2.011954	-3.841868
C	0.566208	-2.945665	-4.833988
C	2.410335	-3.783267	-3.520317
H	2.742939	-2.808638	-1.607049
H	-0.564751	-1.308959	-3.960313
H	-0.055439	-2.981249	-5.742777
H	3.250151	-4.483688	-3.387101
H	1.851909	-4.575525	-5.459585



B.6 (Continued).

[(μ -SMe)(μ -SPh)Fe₂(CO)₆], Me e/Ph a isomer

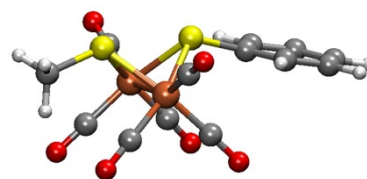
Fe	-1.311407	-0.533863	-0.622281
Fe	0.657734	-1.337183	0.718631
S	0.821554	-0.622491	-1.446580
S	-0.209241	0.756690	0.888140
O	-1.956348	-2.969048	-2.134727
O	-2.640505	1.466088	-2.310812
O	0.836662	-4.110230	-0.235640
O	-3.466046	-1.025629	1.297001
O	3.354437	-1.045995	1.841623
O	-0.744401	-2.157106	3.152575
C	-1.691429	-2.006770	-1.550835
C	-2.105892	0.685243	-1.642695
C	0.773585	-3.014447	0.125881
C	-2.624074	-0.836513	0.523862
C	2.291975	-1.142672	1.387427
C	-0.177487	-1.847546	2.190983
C	-1.145309	1.040802	2.428749
H	-1.732331	0.166175	2.766683
H	-0.409898	1.324407	3.208074
H	-1.821842	1.898995	2.243124
C	1.524895	1.030358	-1.545586
C	2.720172	3.520155	-1.924428
C	2.719693	1.333894	-0.890520
C	0.931319	1.963837	-2.399049
C	1.530942	3.207400	-2.583642
C	3.312831	2.580314	-1.081883
H	3.184403	0.592087	-0.220753
H	4.250182	2.820314	-0.554976
H	3.187368	4.508139	-2.066161
H	1.055030	3.944736	-3.249845
H	-0.010876	1.716559	-2.915966



B.6 (Continued).

[(μ -SMe)(μ -SPh)Fe₂(CO)₆], Me e/Ph e isomer

Fe	-1.318596	-0.572608	-0.663838
Fe	0.662204	-1.350943	0.660027
S	0.821649	-0.544108	-1.476668
S	-0.144573	0.785480	0.750149
O	-2.041780	-3.098404	-1.968354
O	-2.687899	1.320080	-2.448758
O	0.660883	-4.174861	-0.132879
O	-3.422864	-0.940821	1.334364
O	3.429844	-1.087452	1.616693
O	-0.641471	-2.012042	3.193594
C	-1.737140	-2.100884	-1.469347
C	-2.132514	0.587295	-1.746071
C	0.671140	-3.055276	0.156253
C	-2.598791	-0.796523	0.531923
C	2.342179	-1.173201	1.231107
C	-0.115138	-1.760101	2.191913
C	-1.028297	1.166988	2.298120
H	-1.625547	0.319682	2.684904
H	-0.264681	1.463398	3.044503
H	-1.688854	2.032234	2.090782
C	1.140476	-1.803643	-2.706494
C	1.788203	-3.584377	-4.748568
C	2.247224	-2.644569	-2.568367
C	0.362265	-1.842529	-3.866150
C	0.688743	-2.736626	-4.883122
C	2.564926	-3.535542	-3.591165
H	2.857850	-2.601413	-1.650635
H	3.432485	-4.204751	-3.476706
H	2.040249	-4.293733	-5.553265
H	0.069010	-2.771929	-5.793256
H	-0.506467	-1.169930	-3.966136



B.6 (Continued).

[(μ -SMe)(μ -SPh)Fe₂(CO)₆], Me a/Ph a isomer

Fe	-1.338185	-0.475399	-0.562896
Fe	0.661765	-1.300843	0.734393
S	0.765458	-0.604597	-1.426339
S	-0.468984	0.608717	1.244007
O	-2.010487	-2.740896	-2.312119
O	-2.568524	1.729762	-2.054827
O	1.137723	-4.016068	-0.290991
O	-3.566632	-1.191912	1.213113
O	3.290706	-0.694338	1.882488
O	-0.658342	-2.432184	3.103151
C	-1.737541	-1.846265	-1.633275
C	-2.086526	0.855600	-1.466418
C	0.955629	-2.944725	0.101859
C	-2.688593	-0.904719	0.518888
C	2.256514	-0.941702	1.420595
C	-0.138375	-1.981628	2.174776
C	0.394365	2.174845	0.877839
H	-0.131429	2.939910	1.484089
H	1.450638	2.099029	1.205386
H	0.359985	2.443091	-0.194796
C	1.577638	0.968229	-1.684651
C	2.942437	3.316852	-2.321497
C	0.994917	1.900429	-2.548856
C	2.850741	1.197297	-1.158318
C	3.527491	2.372934	-1.476986
C	1.677927	3.074240	-2.859741
H	3.312103	0.450408	-0.491193
H	4.530298	2.551740	-1.056561
H	3.479857	4.246461	-2.568729
H	1.211930	3.809946	-3.534721
H	-0.004645	1.706192	-2.972601

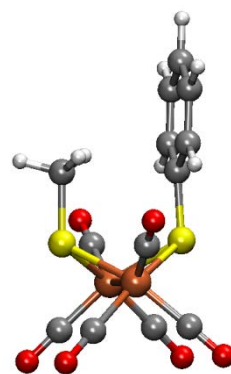
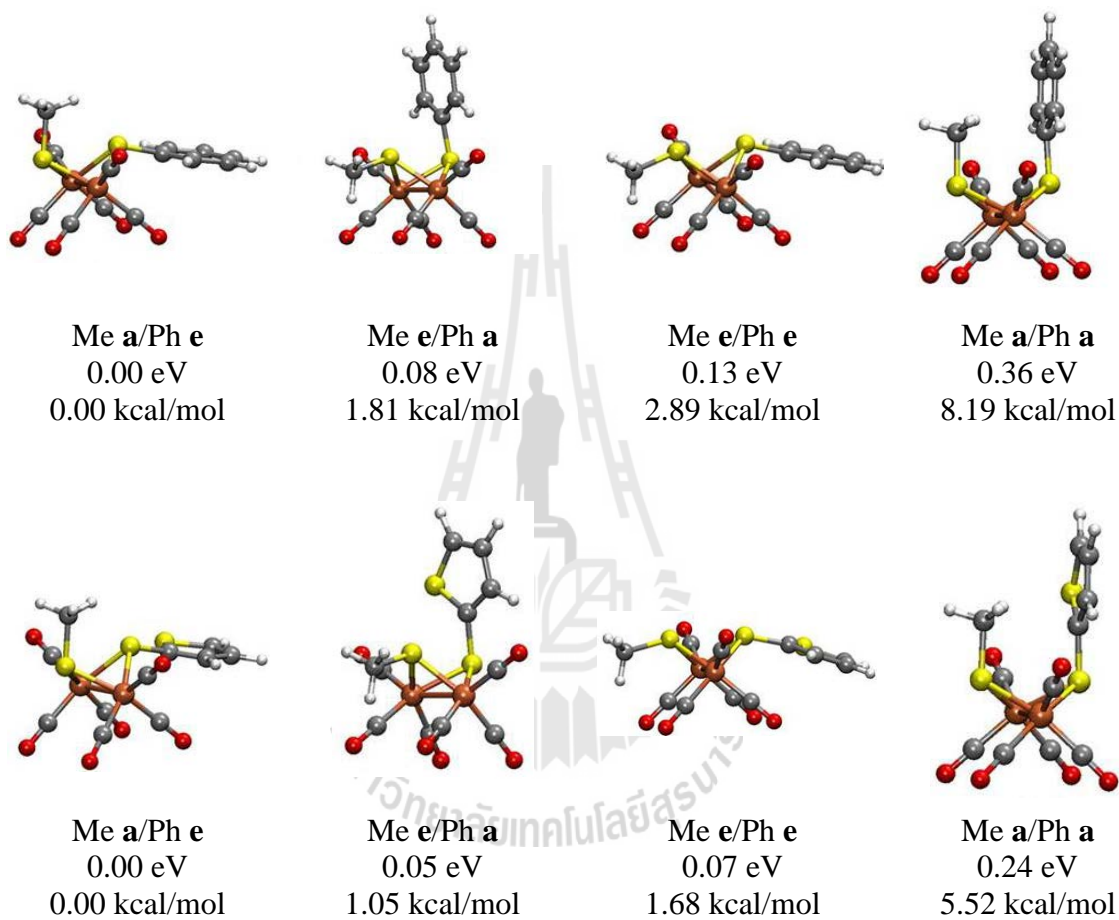


Figure B.8 Comparison of DFT structures of different isomers of $[(\mu\text{-SMe})(\mu\text{-SPh})\text{Fe}_2(\text{CO})_6]$ and $[(\mu\text{-SMe})(\mu\text{-STh})\text{Fe}_2(\text{CO})_6]$. Isomers and relative Gibbs energy were indicated.



APPENDIX C

SUPPORTING INFORMATION FOR CHAPTER V

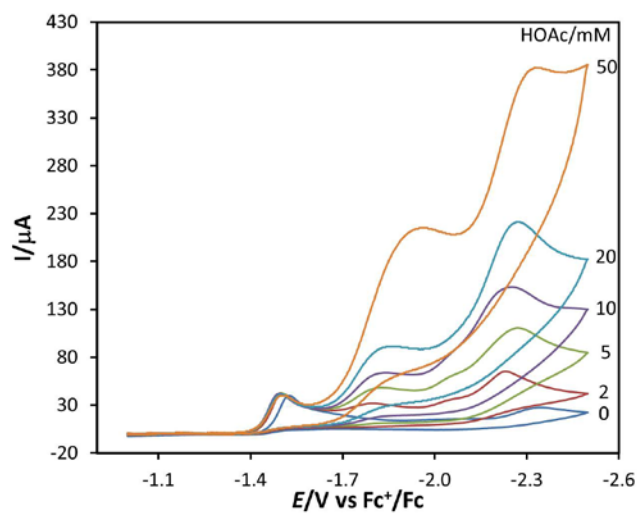


Figure C.1 Voltammograms of **1** in the absence/presence of acetic acid under N_2 atmosphere.

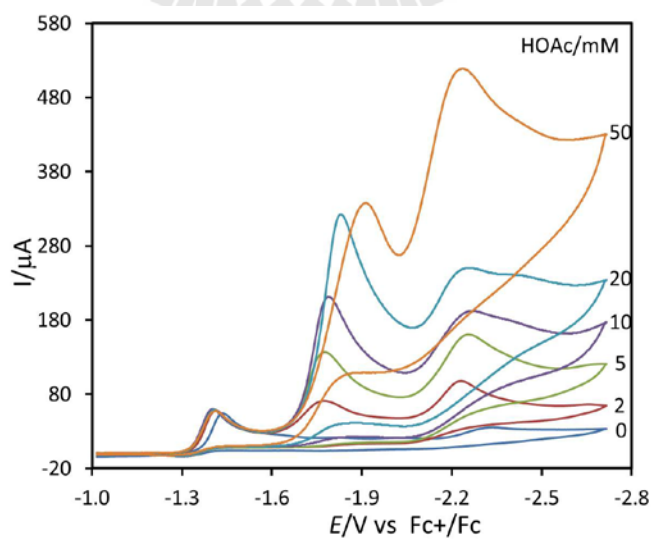


Figure C.2 Voltammograms of **2** in the absence/presence of acetic acid under N_2 atmosphere.

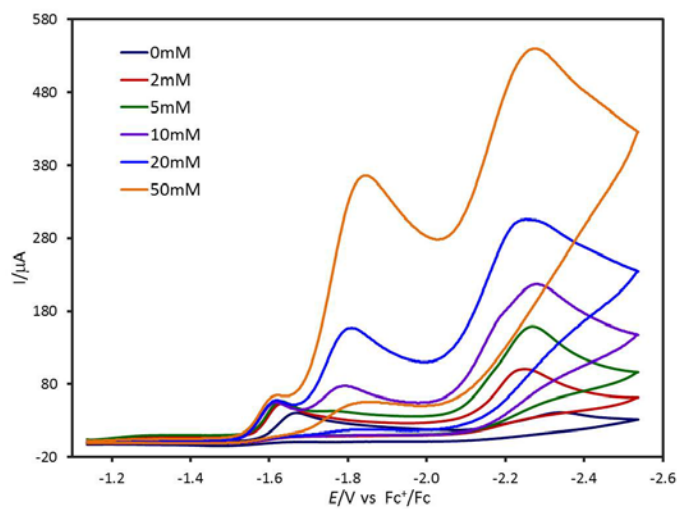


Figure C.3 Voltammograms of $anti-[(\mu-SMe)_2Fe_2(CO)_6]$ in the absence/presence of acetic acid under N_2 atmosphere.

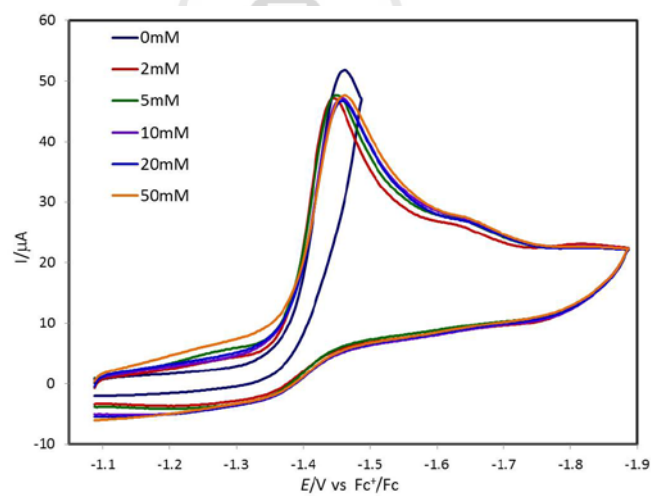


Figure C.4 Voltammograms of **2** in the absence/presence of phenol (pK_a , 29.14) under N_2 atmosphere.

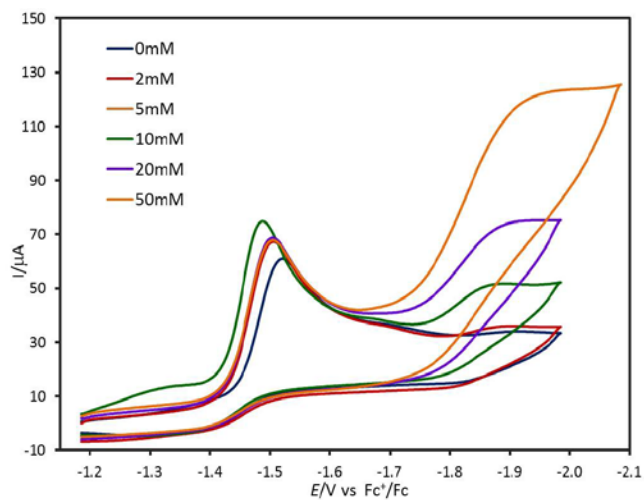


Figure C.5 Voltammograms of **2** in the absence/presence of 4-bromophenol (pK_a , 25.53) under N_2 atmosphere.

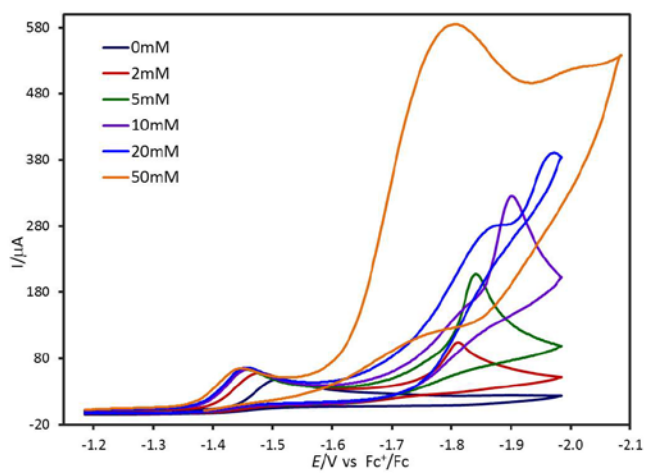


Figure C.6 Voltammograms of **2** in the absence/presence of cyanoacetic acid (pK_a , 18) under N_2 atmosphere.

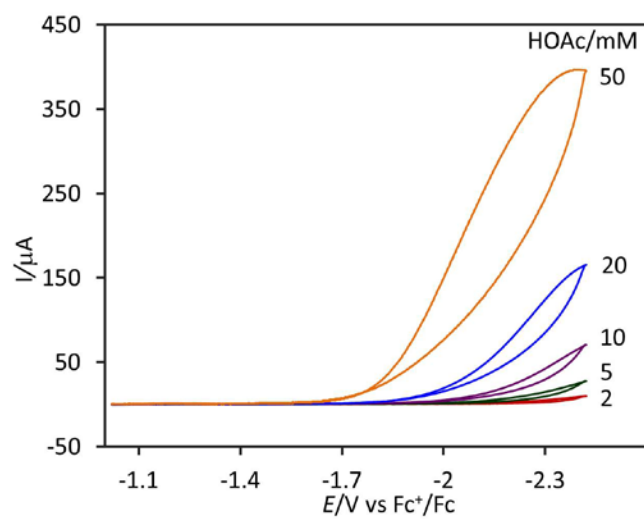


Figure C.7 Direct reduction at GC electrode surface of HOAc under N_2 atmosphere.

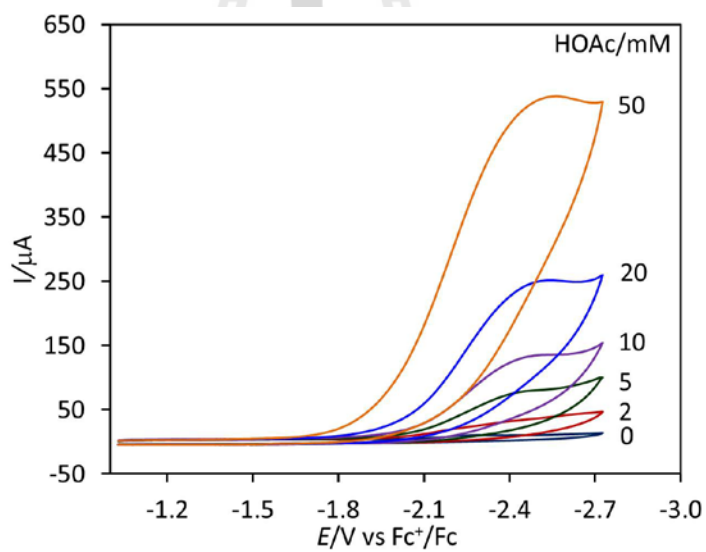


Figure C.8 Direct reduction at GC electrode surface of HOAc under CO atmosphere.

C.1 Synthesis of $[(\mu\text{-SMe})_2\text{Fe}_2(\text{CO})_6]$

The $[(\mu\text{-SMe})_2\text{Fe}_2(\text{CO})_6]$ complex was prepared following the literature method (Seyferth, Henderson, and Song, 1982). 1.02 g (3 mmol) of $[(\mu\text{-S}_2)\text{Fe}_2(\text{CO})_6]$ was added to a 250 mL round bottom flask, purged with Ar for 30 min, and 60 mL of dry THF added to the flask via cannula. The mixture was stirred and cooled to $-78\text{ }^\circ\text{C}$ in a dry ice/acetone bath. 0.1 M lithium triethylborohydride in THF (Aldrich, 99.8%), 6 mL (6 mmol) was slowly added to the reaction flask by adding 0.5 mL of lithium triethylborohydride in every 5 min with stirring. The reaction mixture was stirred at $-78\text{ }^\circ\text{C}$ for 30 min and then 0.9 mL (6 mmol) of iodomethane was added via syringe. The reaction was stirred at $-78\text{ }^\circ\text{C}$ for 20 min and then warmed to room temperature and stirred for 3 hr and the solvent removed by rotary evaporation. The dark red crude product was purified by silica gel chromatographic column, 2.5 x 25 cm, using hexane or pentane as eluents. The *anti*- $[(\mu\text{-SMe})_2\text{Fe}_2(\text{CO})_6]$ was isolated as major product. Yield 0.35 g (1 mmol) 33%; R_f (hexane) 0.52; IR (hexane, CO stretching, cm^{-1}): 2071 (w), 2035 (vs), 1999 (m) and 1989 (m); $^1\text{H-NMR}$ (CDCl_3): δ (ppm), 1.24 (s, CH_3 **a**), 1.61 (s, CH_3 **e**)

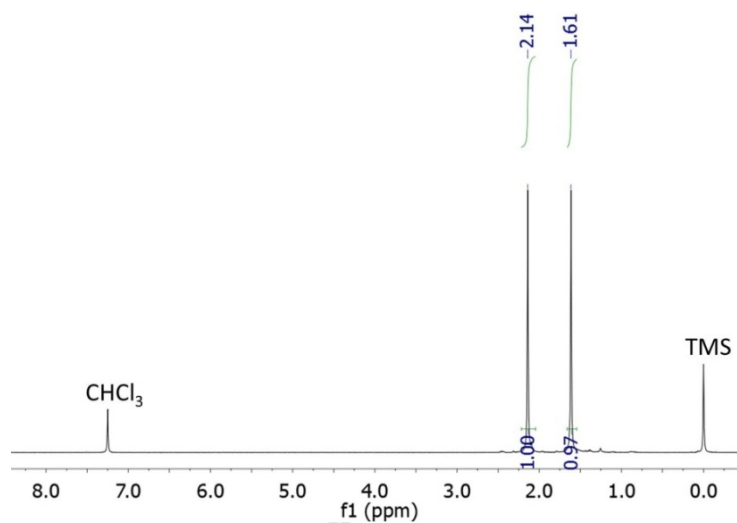


Figure C.9 ¹H-NMR spectrum of *anti*-[(μ -SMe)₂Fe₂(CO)₆] in CDCl₃ solution.

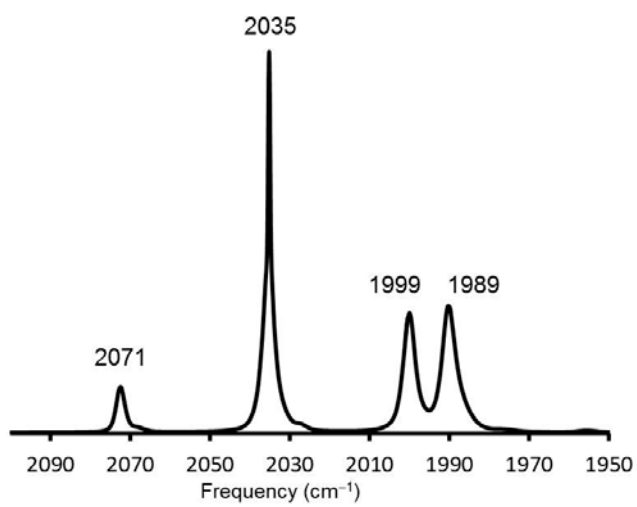


Figure C.10 IR absorption spectrum in carbonyl stretching region of *anti*-[(μ -SMe)₂Fe₂(CO)₆] in hexane.

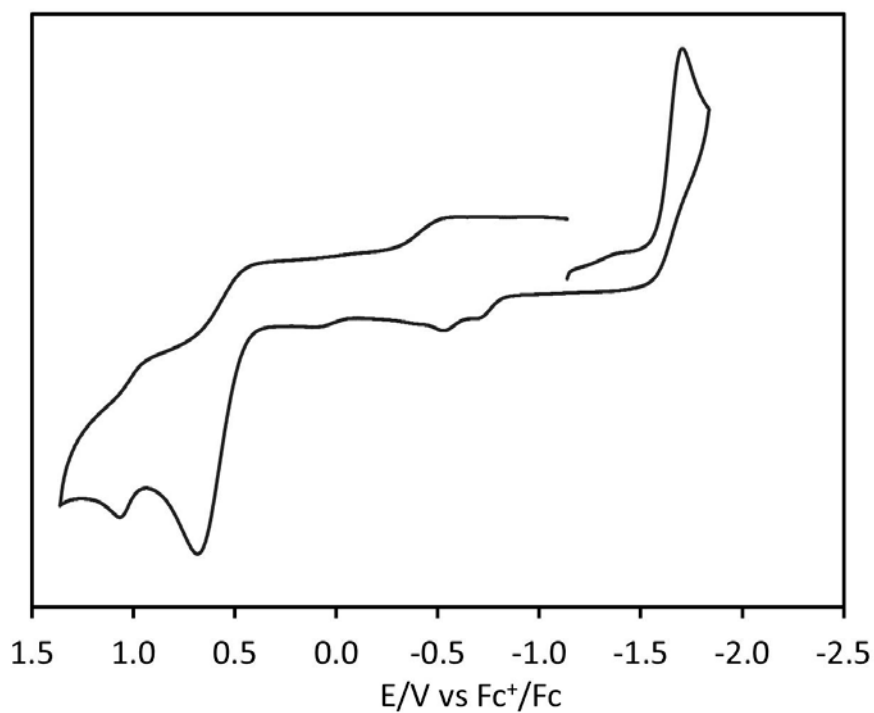
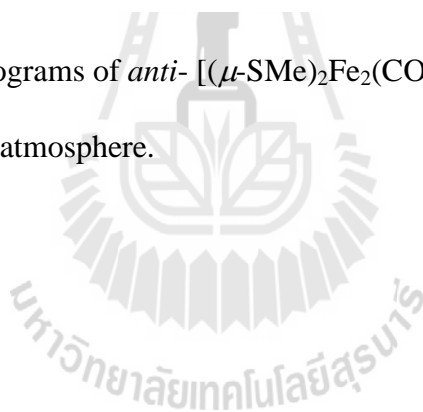


Figure C.11 Voltammograms of *anti*- $[(\mu\text{-SMe})_2\text{Fe}_2(\text{CO})_6]$ in the absence of acid under N_2 atmosphere.



APPENDIX D

CONFERENCE PRESENTATIONS AND PROCEEDINGS

D.1 Presentations

Oral presentations

1) **Orrasa In-noi**, Samroeng Krachodnok, and Kenneth J. Haller. Supramolecular Interactions Linking Zinc Vanadate Layers. *The 1st Suranaree University of Technology Graduate Conference (SUT-GRAD1)*. 1-2 November 2007. Nakhon Ratchasima, Thailand.

2) **Orrasa In-noi**, Kenneth J. Haller, John H. Enemark, Dennis H. Evans, Richard S. Glass, Dennis L. Lichtenberger. Synthesis, Structural, and Electrochemical Studies of Diiron Hydrogenase Mimics for Molecular Hydrogen Generation: $[(\mu\text{-SCH}_3)(\mu\text{-SC}_4\text{H}_3\text{S})\text{Fe}_2(\text{CO})_6]$. *Pure and Applied Chemistry International Conference (PACCON2012)*, 11-33 January 2012, Chiang Mai. Thailand.

Poster presentations

1) **Orrasa In-noi**, Samroeng Krachodnok, Kenneth J. Haller, Herman H.-Y. Sung, Fanny L-Y. Shek, and Ian D. Williams. A Three-Dimensional Supramolecular Structure of Zinc Vanadate: $\text{Zn}(2\text{-EtIm})_2(\text{VO}_3)_2$. *The 8th Conference of the Asian Crystallographic Association (AsCA'07)*, 4-7 November 2007. Taipei, Taiwan.

2) **Orrasa In-noi**, Samroeng Krachodnok, Kenneth J. Haller, Herman H.-Y. Sung, Fanny L-Y. Shek, and Ian D. Williams. Hydrothermal Synthesis and Structural Characterization of a Zinc Vanadate Compound. *The 33rd Congress on Science and Technology, (STT'33)*, 18-20 October 2007, Nakhon Si Thammarat, Thailand.

3) **Orrasa In-noi** and Kenneth J. Haller. Solvothermal Synthesis and Characterization of Zinc Blend CdSe Nanocrystals. *CHE-USDC Congress I*, 5-7 September 2008, Chonburi, Thailand.

4) **Orrasa In-noi** and Kenneth J. Haller. Solvothermal Synthesis and Characterization of CdSe nanoparticles. *The 34th Congress on Science & Technology of Thailand (STT'34)*, 31 October-2 November 2008, Bangkok, Thailand.

5) **Orrasa In-noi** and Kenneth J. Haller. Effect of Supramolecular Structure on Molecular Structure in a Titanium(III) Oxalate Dimer. *German-Thai Symposium on Nanoscience and Nanotechnology 2009 (GTSNN2009)*, 21-22 September, 2009, Chiang Mai, Thailand.

6) **Orrasa In-noi** and Kenneth J. Haller, Supramolecular Structure of a Titanium(III) Oxalate Dimer: $\text{Ti}_2(\mu\text{-C}_2\text{O}_4)(\text{C}_2\text{O}_4)_2(\text{H}_2\text{O})_6 \cdot 2\text{H}_2\text{O}$. *The 35th Congress on Science & Technology of Thailand (STT'35)*, 15-17 October 2009, Chonburi, Thailand.

7) **Orrasa In-noi** and Kenneth J. Haller. Synthesis and Characterization of A Titanium Imidazole Carboxylate Compound. *Pure and Applied Chemistry International Conference (PACCON2010)*, 21-23 January 2010, Ubon Ratchathani, Thailand.

8) **Orrasa In-noi** and Kenneth J. Haller. Effect of Supramolecular Structure on Molecular Structure in a Titanium(III) Oxalate Dimer: $\text{Ti}_2(\mu\text{-C}_2\text{O}_4)(\text{C}_2\text{O}_4)_2(\text{H}_2\text{O})_6 \cdot 2\text{H}_2\text{O}$. *2011 American Crystallographic Association Meeting (ACA2011)*, 28 May - 2 June 2011, New Orleans, Louisiana. USA.

9) **Orrasa In-noi**, Gary S. Nichol, Dennis L. Lichtenberger, John H. Enemark, Kenneth J. Haller. Three-Dimensional Framework Structure of Vanadium and 1,2,4,5-Benzenetetracarboxylate. *The XXII Congress and Assembly International Union Crystallography (IUCr2011)* 22-30 August 2011, Madrid, Spain.

10) **Orrasa In-noi**, Gary S. Nichol, Dennis L. Lichtenberger, John H. Enemark, Kenneth J. Haller. A Three Dimensional Vanadium Framework Constructed by 1,2,4,5-Benzenetetracarboxylate. *American Chemical Society Fall Meeting*. 28 August-2 September 2011, Denver, Colorado, USA.

11). **Orrasa In-noi**, Kenneth J. Haller, John H. Enemark, Dennis H. Evans, Richard S. Glass, Dennis L. Lichtenberger. Synthesis, Structural, and Electrochemical Studies of Diiron Hydrogenase Mimics: $[(\mu\text{-SR})(\mu\text{-SR}')\text{Fe}_2(\text{CO})_6]$ system. *American Chemical Society Spring Meeting*, 25-29 March 2012, San Diego, California, USA.

D.2 Conference Proceedings

1) **Orrasa In-noi**, Samroeng Krachodnok, and Kenneth J. Haller, Supramolecular Interactions Linking Zinc Vanadate Layers. *The 1st SUT Graduate Conference*. 1-2 November 2007, Nakhon Ratchasima, Thailand.

2) **Orrasa In-noi** and Kenneth J. Haller, Supramolecular Structure of a Titanium(III) Oxalate Dimer: $\text{Ti}_2(\mu\text{-C}_2\text{O}_4)(\text{C}_2\text{O}_4)_2(\text{H}_2\text{O})_6 \cdot 2\text{H}_2\text{O}$. *The 35th Congress on Science & Technology of Thailand (STT'35)*, 15-17 October 2009, Chonburi, Thailand.

3) **Orrasa In-noi** and Kenneth J. Haller. Effect of Supramolecular Structure on Molecular Structure in a Titanium(III) Oxalate Dimer. *German-Thai Symposium on Nanoscience and Nanotechnology 2009 (GTSNN2009)*, 21-22 September, 2009, Chiang Mai, Thailand.

CURRICULUM VITAE

Personal Information:

Name: Orrasa In-noi

Born: April 4, 1982, Ubon Ratchathani, Thailand

Citizenship: Thai

Educations:

May 2006-present Ph.D. candidate, Suranaree University of Technology,
Nakhon Ratchasima, Thailand.

May 2005-Mar 2006 Grad. Dip., Teaching Profession, Khon Khean University.

May 2001-Apr 2004 B.Sc., Chemistry (Second Class Honor), Ubon Rajathani
University.

Scholarships and Awards:

The Office of the Commission of Higher Education (2006-present), The
Institute for the Promotion of Teaching of Science and Technology (2001-2005),
ACA Travel Award (ACA2011), New Orleans, LA. USA., and IUCr Young Scientist
Travel Grant (IUCr2011), Madrid, Spain.

Professional Experiences:

Collaborative Research in Chemistry, Department of Chemistry and
Biochemistry, The University of Arizona, Tucson, Arizona, USA (Sep 2010-Sep 2011
and Mar 2012-Apr 2012)